Syracuse University

SURFACE

August 2020

Laboratory Studies of Structural Changes in Water-Poor and Water-Rich Ices: A Connection to Molecule Formation in Interstellar Ices

Francis Eugene Toriello
Syracuse University

ABSTRACT

In this thesis I explore the results of ultra-high vacuum laboratory experiments performed at the Syracuse University Astrophysics and Surface Science Laboratory on structural changes of analogs of ice mantles that cover dust grains in dense clouds in the interstellar medium. We present the experimental and analytical techniques that we used and the motivations for the investigations in the context of molecular astrophysics. The primary contribution of this thesis is the meaningful insight into the long-standing question of how molecular diffusion and formation occur in or on ices in the interstellar medium under the conditions of low pressure and low temperature. Specifically, the focus is placed on an astrophysically relevant two layer ice geometry where the first layer is primarily composed of water molecules (water-rich), while the second layer's dominant species is CO (water-poor). We consider each layer separately, first investigating the pore surface area of the water-rich layer and correspondingly its ability to store, trap, and facilitate the formation of complex organic molecules (COMs). We then consider the water poor layer where we report the discovery of a new phase transition in carbon monoxide ice at low temperature. We use CO_2 as a probe within the CO ice matrix to demonstrate how this transition causes a diffusion and clustering of CO_2 and consequentially suggests the potential mechanism for molecular formation in the ISM. This information is used to build a predictive model that is applied to an astrophysically relevant parameter space within which we are able to directly relate the time scale on which this transition occurs with that of stellar evolution.

LABORATORY STUDIES OF STRUCTURAL CHANGES IN WATER-POOR AND WATER-RICH ICES: A CONNECTION TO MOLECULE FORMATION IN INTERSTELLAR ICES

By

Francis E. Toriello

M.S., Syracuse University 2016

B.S, Columbia University 2014

DISSERTATION

SUBMITTED IN PARTIAL FULFILLMENT OF THE REQUIREMENTS

FOR THE DEGREE OF

DOCTOR OF PHILOSOPHY IN PHYSICS

Syracuse University

August 2020

ACKNOWLEDGEMENTS

Contents

List of Tables

List of Figures

Preface

The content of Chapter 3 and Chapter 5 is taken from

He, J., Clements, A. R., Emtiaz, S. M., Toriello, F., Garrod, R. T., Vidali, G., "The Effective Surface Area of Amorphous Solid Water Measured by the Infrared Absorption of Carbon Monoxide." In: (2019) The Astrophysical Journal 878.2, doi: 10.3847/1538-4357/ab1f6a

The content of Chapter 4 and Chapter 5 is taken from

He, J., Toriello, F. E., Emtiaz, S. M., Henning, T., Vidali, G., "Phase Transition of Interstellar CO Ice." In: submitted to Nature Astronomy

To my parents.

Chapter 1

Introduction

1.1 Background

The field of molecular astrophysics devotes itself to the "study of the formation, destruction, and excitation of molecules in astronomical environments and the corresponding influence on the structure, dynamics and evolution of astronomical objects." [10]. The astronomical environments we will be considering are those of the interstellar medium (ISM), a physically diverse and chemically active landscape between star systems that consists of gas, dust, and ice. The condensation of gasphase species on cold dust grains is considered to be a powerful chemical route by which ices and molecules are formed in ISM dense clouds; a starting point from which excitation, destruction, and further molecular formation are guided by cloud collapse and stellar evolution. Surface chemistry thus plays a commanding role in understanding the composition of ice mantles and molecular gas that is desorbed from dust grains and observed in the space surrounding of young stellar objects (YSO) [11].

1.1.1 Interstellar Gas

The interstellar gas is composed primarily of hydrogen followed by helium and trace amounts of oxygen, carbon, and nitrogen (see Table 1) for elemental abundances [5]. To better understand its elemental composition and where and how molecules are formed and found, as well as its temperature and pressure range, we refer to the three phase model of the ISM put forward by McKee and Ostriker [2]. The three phase model only takes hydrogen in to account assuming that the influence of other elements are negligible and is defined by the intensity of the Interstellar Radiation Field (ISRF) in that region [2]. The ISRF is the integrated light of all the stars in the galaxy possessing a mean energy density of $7 \ 10^{-14}$ J m^{-3} [12]. The three phases of the model

are: Cold Neutral Interstellar Medium (CNM), Warm Interstellar Medium which is broken down into subphases: neutral (WNM) and ionized (WIM) , and Hot Interstellar Medium (HIM) [2].

The details discussed in the following paragraph are summarized in Table 2. The HIM region accounts for most of the ISM ($\sim 70\%$) and as a result of energy imparted by nearby supernovae contributes photons (UV for example) to the ISRF that have enough energy (greater than 13.56 eV) to ionize atomic hydrogen. Thereby this region is hot (average temperature of $\sim 10^5$ K), low in density ($\sim 10^{-2}$ particles cm^{-3}), and populated primarily by H$^+$. The WIM and WNM regions collectively account for approximately 30% of the ISM with average temperatures approximately of 8,000 K and 80 K, respectively, and densities of approximately 0.1 to 1 and 10 to 100 particles cm^{-3}, respectively. The WIM region is populated by atomic hydrogen (H) and ionized hydrogen (H$^+$) and is where low pressure gas clouds known as inter clouds are formed. The WNM region is populated by atomic hydrogen (H) and is where diffuse gas clouds are formed. The CNM phase accounts for less than 1 % of the ISM and is the region where dense molecular clouds form. It has a temperature range of approximately 10 - 70 K; it is coldest at the cloud core and becomes warmer moving outwards towards the edges. This phase also has a relatively high average density of approximately 10^4 particles cm^{-3} and is populated largely by molecular hydrogen (H$_2$) formed on the surface of dust grains [2] (formation of H$_2$ on dust grains is discussed more in the subsection below).

Dense molecular clouds in the CNM phase often are of most interest to molecular astrophysicists. This is due to the fact that the cores of dense clouds are shielded from the interstellar extinction of UV photons by dust grains that reside at cloud edges. Molecular hydrogen provides self-shielding as well. This protection provides an environment in which molecules that are too fragile to exist in other regions of the ISM can form and have an appreciable probability of survival. In turn, they may ultimately seed planetary systems that are produced via the collapse of dense clouds; the typical lifetime of dense clouds is between 10 and 50 Myrs [13]. Over 200 molecular species have been identified in the ISM via the detection of radio, far-IR and mid-IR spectra when molecular rovibrational transitions are undergone in the gas phase; in the solid state phase (i.e. in or on ice), molecules are identified through their near and mid IR spectra. About one third of these detected molecules have multiple carbon atoms which are known as COMs (Complex Organic Molecules) by their astronomical classification [14, 15].Example of detected COMs in the ISM include Hydrocarbons: ethene (HC$_4$H), butadiyne (H$_2$C$_4$), butatrienylidene (H$_2$C$_4$); O-Containing: methanol (CH$_3$OH), propynal (HC$_2$CHO), acetaldehyde (CH$_3$CHO); N-Containing: acetonitrile (CH$_3$CN), methylisocyanide (CH$_3$NC), keteneimine (CH$_2$CNH); S-Containing: methyl mercaptan

(CH$_3$SH); and N,O-Containing: formamide (NH$_2$CHO), acetamide (CH$_3$CONH$_2$) [16]. Particularly noteworthy is the Atacama Large Millimeter/submillimeter Array (ALMA) 2014 discovery of the COM isopropyl cyanide (C$_4$H$_7$N) in the giant gas cloud Sagittarius B2. It was the first detection of a branched-carbon based molecule. [17]. In 2016 the chiral molecule propylene oxide (CH$_3$CHCH$_2$O) was also detected by ALMA in Sagittarius B2 [18]. These discoveries give meaningful credit to the theory that life essential molecules are a consequence of interstellar chemistry that takes place in the CNM phase and that they might seed planets with such biogenic molecules.

1.1.2 Interstellar Dust

Interstellar dust grains are primarily made up of a mix of amorphous silicates and carbonaceous materials; dust grains account for virtually the all of silicon, magnesium, and iron and approximately 30% of oxygen and 70% of carbon in the ISM. Dust grain sizes range from 0.001μm to 0.1 μm; the smaller grains being more prevalent. The smaller grains are responsible for the extinction of UV radiation and thus play a crucial role in the shielding of dense cloud cores. As discussed in the last subsection, this shielding is important for extended lifetimes of molecules and corresponding increase in molecular complexity [5]. Interstellar dust grain parameters such as these are often deduced from observations. For example, the 1930 Trumpler observations revealed that clouds of interstellar dust were dimming starlight as it passed though space with a wavelength dependence of the interstellar extinction that was proportional to $\frac{1}{\lambda}$, which implied that dust grains were on the scale of submicrons [19]. Dust grain parameters are determined more effectively by a combination of observations and statistical models that consider different compositions and distributions of size in order to fit or reproduce the observed wavelength-dependent extinction. Mathis et al. [20] developed an authoritatively successful interstellar dust model by using observed extinction of starlight along lines of sight that pass through diffuse clouds in the WNM phase, and deducing a power-law interstellar dust grain size distribution function (IDGSDF) approximately given by:

$$n(a) \sim a^{-3.5} \tag{1.1}$$

where n is the number density of dust grains and a is the dust grain size in μm [20].

The temperature of dust grains is particularly important given that physical chemical processes on the dust strongly depend on this parameter. Furthermore, dust grains require temperatures in excess of 1200 K to vaporize and thus are fairly resilient and versatile components of the ISM. For example, at the boundary of dense clouds, shielding takes place and grains that absorb UV photons heat up and emit mid-IR radiation [5]. This is known as the photodissociation region (PDR) and dust grains not only prevent the penetration of UV radiation but the IR radiation they emit heats

the surrounding gas via the photoelectric effect, causing the emission of electrons. Dust grain temperatures in regions throughout dense clouds and extending in to the CNM on the other hand range between 10 and 70 K as the three phase model tells us (see Table 2). Dust grains do not emit IR radiation in this temperature range but instead the coldest grains in the dense cloud cores serve as a catalytic surface upon which atoms and molecules accrete and molecular bonds form. In fact, dust grains are considered responsible for the formation of all of the molecular hydrogen in the ISM and the hydrogenation of O, C, and N; a process that is key to the formation of ice mantles which coat the dust grains [11, 21]. It is important to note for the most cases and the work presented in this thesis the surface particles of dust grains are not considered to play a catalytic role with regard to chemistry of ice or volatile gases but rather provide a site on which reactions occur [5].

1.1.3   Interstellar Ice

Spitzer Space Telescope data of large samples of young stellar objects (YSO), such as the protostar HH46 IRS - to be discussed later, show that the dominant ice species detected in the ISM are simple molecules, H_2O, CO, CO_2, CH_4, NH_3, and CH_3OH (see Figure 2 and Table 3). The most prevalent of ice species is H_2O. It is important to note that these ices detected in YSO are considered to be representative of the dense cloud environments where they formed. These ice species have been confirmed by stimulatory laboratory experiments [22] [23] and observational inventory of interstellar ices performed by the Kuiper Airborne Observatory (KAO) and the Infrared Space Observatory (ISO). They are also precisely those predicted by the hydrogenation and oxidation of dominant elements O, C, and N which occurs on the surface of cold dust grain as discussed in the last subsection [11, 21]. The exception is CO which directly accretes from the gas phase on to the grain surface.

Interstellar ices have a layered structure that is interpreted from the shapes of the ice IR bands and the characteristics of the cloud, and consist of a water-rich first layer followed by a water-poor second layer. The thickness and composition of the layers depend on the chemical make up of the cloud and its thermal history. The layer in which a given molecule resides is revealed by the molecule's vibrational constant (i.e. spring constant) which differs depending on whether the molecule is surrounded by water molecules or not. This distinction is found in the line profile of solid CO and is indicative of the fact that 60-90 percent of CO is in pure form (i.e. is not surrounded by water molecules) and is the dominant component of the water-poor layer (i.e. CO rich) [24, 11]. While this layered interstellar ice grain geometry, called the onion model, is well

understood, the morphology (porous vs non-porous and amorphous vs crystalline) of both the CO-rich (water-poor) outer layer and CO-poor (water-rich) inner layer is not. Nor are the potential consequences this information bares with regard to COM formation.

COM formation can be broken into three generations; zeroth, first, and second. The zeroth generation is representative of COM formation during ice formation when the cloud core is still cold and star formation has not yet begun. The zeroth generation is the most challenging to study, since the chemical pathways that can lead to COM formation at temperatures as low as 10 K are currently not well understood. Curiosity with regard to molecular formation during this generation is peaked by the fact that all of the YSO sources in the Spitzer samples mentioned above show remarkable similarities with regard to composition which suggests that there exists a strong and universal zeroth generation formation mechanism. The main point of this thesis is to make a meaningful contribution to this long-standing issue that currently is being investigated via observations, laboratory work and computer simulations, as presented in greater detail in sections and chapters below. The first generation is commenced during protostellar warm-up when enough thermal energy is imparted to the ice mantle (via warm-up of the grain surface), in such a way that molecules in and on the ice mantle become mobile. The second generation is the result of high temperatures in which the ice mantle evaporates, and COMs are ejected from the grains and some COMs are also formed in the gas phase from this enrichment of the gas-phase chemical environment [5].

1.2   Surface Chemistry

A surface chemical model will be required going further in order to quantify experimental data and draw meaningful connections between laboratory results and astrophysical phenomena associated with interstellar ice-coated dust grains. We will be focusing our attention on surface chemical mechanisms that occurs at the solid-vacuum interface and in the solid state. Figure 1 illustrates the mechanisms that will be considered: adsorption, diffusion, and desorption [5].

Key to adsorption is the probability that a given atomic or molecular species sticks to the grain surface when collision occurs. This is known as the sticking coefficient and is defined as the ratio of molecules that adsorb to the surface to the sum total of all molecules that impinge on the surface. Diffusion of a species in or on an ice mantle is paramount as it is considered the primary mechanism by which COM formation occurs. There are two ways in which diffusion can be described; quantum tunneling and thermal hopping. Diffusion via quantum tunneling is particularly important for H as its low mass makes it significantly more likely to tunnel across energy barriers to other adsorption sites as opposed to heavier atoms and radicals. Generally speaking, quantum tunneling becomes dominant at temperatures below 100 K, which is likely to

be the primary mechanism for many hydrogenation reactions on the surface of cold of grains [25]. However, the tunneling rate is highly sensitive to the height and width of the energy barrier between adjacent adsorption sites. Experiments of molecular hydrogen formation on disordered/amorphous surfaces in this laboratory showed that H_2 formation is initiated by thermal energy [26]. Diffusion via thermal hopping, however, is more relevant to this thesis and can be defined in terms of a rate coefficient given by equation:

$$K_{hop} = \nu \exp(\frac{-E_{hop}}{T_s}) \tag{1.2}$$

where ν is the vibrational frequency of the molecule in the particle-surface adsorption potential well, E_{hop} is the energy barrier that must be overcome in order for diffusion to ensue, and T_s is the temperature of the surface. The diffusion energy barrier, E_{hop}, is conventionally considered to be a fraction (0.3 to 0.8 depending on the model) of the binding energy (E_{bind}), the energy required for the molecule to desorb from the surface [5]. It is important to note that this model does not take into account the possibility of the surface being rough in which case the energy barriers may change from site to site. An example of this occurance is the case for porous ice in contrast to smooth compact ice. Such morphological states can significantly change the surface dynamics of a given species. For example, in chapter 3 we will investigate porous amorphous solid water (p-ASW) and how CO diffuses or gets trapped in water ice pores. This is in contrast to chapter 4 in which we will work with compact (non-porous) ASW. Different analyses and models will be developed and used in the two cases.

1.3 Relevant Work

Laboratory experiments performed and analyzed at the Syracuse University Laboratory of Astrophysics and Surface Science are the focus of the work that comprises this thesis. Our primary objective is to simulate the environment of the interstellar medium and the chemical processes described above so as to measure physical parameters that are useful in making meaningful and powerful predictions with regard to astrophysical phenomena.

A detailed technical description of our laboratory and measuring methods is provided in chapter 2 of this thesis. It is advised that this introductory chapter be treated as a guiding companion when reading the second chapter, so as to be able to discern utility and purpose of the various equipment and measurement techniques that are mentioned. For added clarity, I will explicitly call on this introductory chapter throughout the next chapter. In the second half of chapter 2 we focus on an in-vacuum helical coaxial resonator I designed and built for the dissociation of gaseous molecules and

ultimately the production of atomic beams. I mathematically explore this useful laboratory tool and demonstrate a novel insight into its technical parameters; the work presented is done in the pursuit of making meaningful recommendations for future work using this piece of equipment. I discuss the exciting potential that in-vacuum atomic beam sources have with regard to the investigation of COM formation via radical-induced chemistry of interstellar ice analogues.

In chapter 3 we perform a systematic study of the water rich (CO-poor) layer of ASW and ASW mixtures via the infrared absorption spectrum of CO as a tool to measure the temperature dependence of pore surface area, connectivity, and trapping potential. The primary motivation for doing so is the potential of efficient diffusive processes that p-ASW may have to offer with regard to the production of COMs in the ISM.

In chapter 4 we explore the water poor (CO-rich) layer of ASW and consider the crystallization of CO as a mechanism by which COM formation occurs. We present compelling evidence of low temperature crystallization kinetics that have never been identified or measured before. We extend our novel experimental results to construct a predictive model that is applied to an astrophysically relevant parameter space and impactful predictions are made with regard to COM formation.

Table 1: Elemental Abundances of ISM [1]

Species	Abundance
H	1
He	1×10^{-1}
O	5×10^{-4}
C	2×10^{-4}
N	7×10^{-5}
Fe	3×10^{-5}
Mg	3×10^{-5}
Si	2×10^{-5}
S	1×10^{-5}
Ca	2×10^{-6}
Ni	1×10^{-6}

Table 2: The Three Phase Model of the ISM [2]

Phase	Region	Species Present	T(K)	Density (particles cm^{-3})	% ISM
HIM	Ionized	H^+	$\sim 10^5$	$\sim 10^{-2}$ - 10^{-3}	$\sim$ 70 - 80%
WIM	Inter clouds	H^+ and H	8000	0.1 - 1	$\sim 20 - 30\%$
WNM	Diffuse clouds	H	80	$10 - 100$	$\sim$3%
CNM	Dense Clouds	H_2	$\sim$ 10-70	10^4	less than 1%

Table 3: Molecular Abundances of ISM [1] [3]

Species	Abundance
H_2	1
CO	8 X 10^{-5}
OH	3 X 10^{-7}
H_2O	< 7 X 10^{-8}
O_2	< 3.9 X 10^{-8}
C_2	5 X 10^{-8}
CN	3 X 10^{-8}
CH	2 X 10^{-8}
C_4H	2 X 10^{-8}
NH_3	2 X 10^{-8}
H_2CO	2 X 10^{-8}
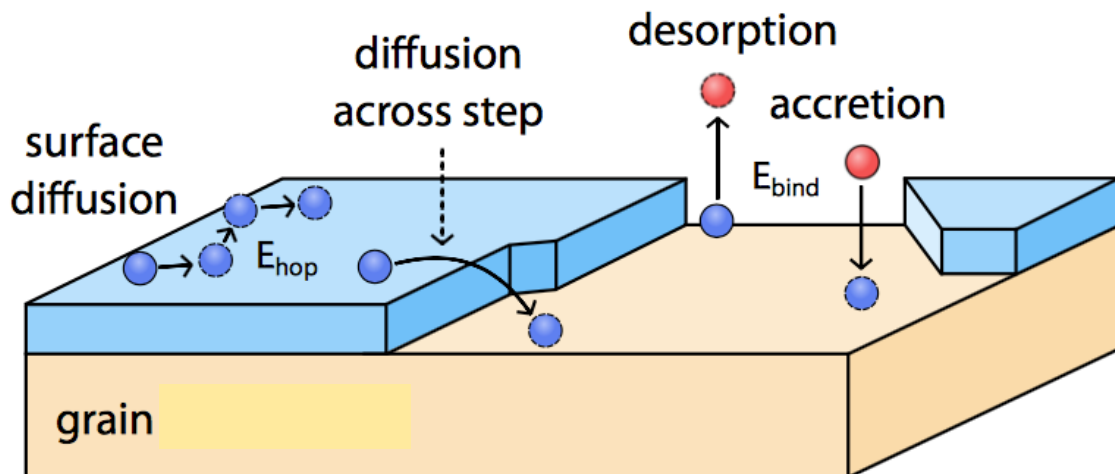
Figure 1: Illustration of gas-grain chemistry model for binding sites on a dust grain surface. The image was created by Dishoeck [5]
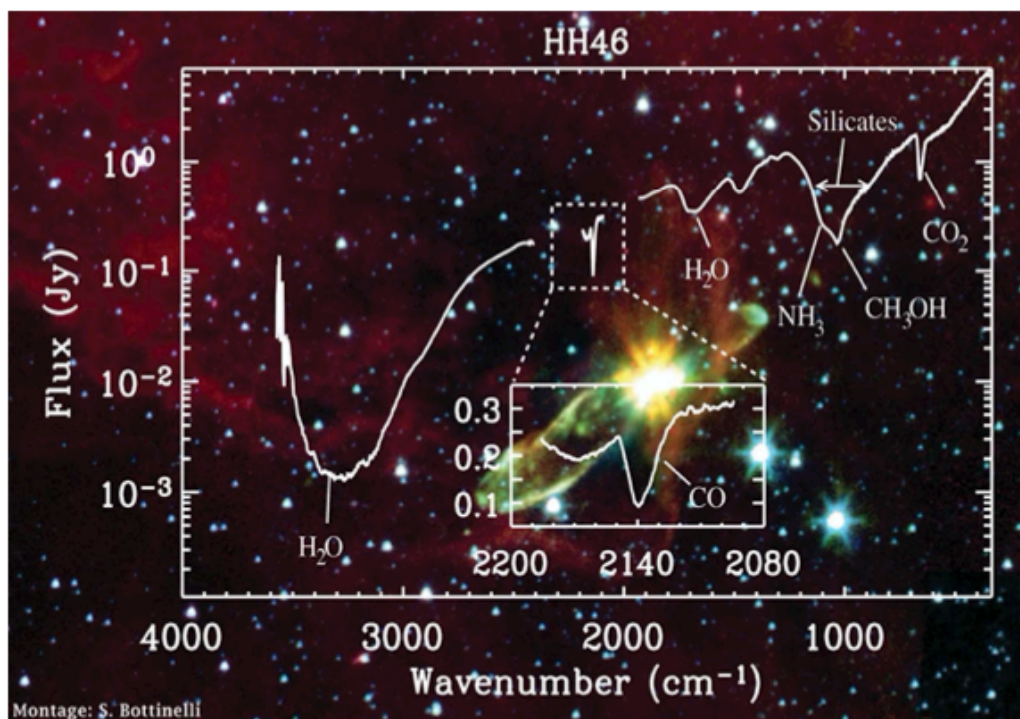
Figure 2: Detection of ices torward the low-mass protostar HH46 IRS using Spitzer data at 5-20μm
Credit NASA/ESA/A.Noriego-Crespo [5]

Chapter 2

Experimental Setup

2.1 General

A comprehensive view of the Syracuse University Laboratory of Astrophysics and Surface Science ultrahigh vacuum (UHV) apparatus is shown in top view in Figure 3 (top view) and side view in Figure 4. The apparatus can be divided into three major areas; a UHV main chamber and two triply differentially pumped UHV beam lines and are referred to as R-Line and L-line in this thesis (Figure 3). Located at the geometric center of the main chamber is the substrate or otherwise known as the sample, which is a gold-coated copper disk attached to the cold finger of a closed-cycle helium cryostat (ARS DE-204 4K). The sample is representative of an interstellar dust grain; referred to as a dust grain analogue. The sample temperature is measured by a calibrated silicon diode sensor (DT670) placed behind the substrate. A cartridge heater in the sample holder is used to heat the sample. A Lakeshore 336 temperature controller reads and controls the temperature between 5 to 300 K with an accuracy better than 50 mK.

2.2 Beam Sources

Diatomic gases commonly used in the laboratory such as N_2 and O_2 need to be molecularly dissociated in order to produce atomic beams. Atomic and molecular beams are used to deposit species on the substrate at low temperatures. The species produced are typically representative of dominant elements in the ISM. There are many ways to transfer energy to gases and break down the molecular bonds. Conventional techniques include thermal and microwave or radio frequency (RF) dissociation. Electromagnetic energy can be transferred by inductive or capacitive means [7]. The work presented in the latter half of this chapter pertains to inductive RF dissociation.

The cavity in which the gas resides during dissociation, known as the beam source, is a Pyrex

glass tube that is mated and vacuum sealed to its respective beamline by a glass ball joint with rubber O-ring. This ball joint is mounted on stainless steel bellows with X-Y positioning stages for alignment. The beam sources are each equipped with a water jacket for cooling, a quarter inch ribbed molecular gas inlet on the non-vacuum side and a nozzle on the UHV side that is approximately 1mm in diameter and 10 mm by length. The molecular gas inlet is connected to an Alicat gas flow regulator followed by a VCR stainless steel manifold that is pumped by a turbomolecular pump in an external pumping station and mated to gas tanks by PVC lines. The beam sources are inserted into coaxial resonators with helical inner conductors which provide the dissociative RF energy mentioned above. The R-Line resonator is installed externally to the vacuum system while the L-Line resonator is installed in the first stage vacuum chamber see Figure 4). The latter resonator is where I focused my work, and is explained in second half of this chapter.

2.3   Beamlines

The beamlines are replicas of one another with regard to their structure and, for the purposes of this section, Figure 4 is representative of both lines. Each beamline consists of three vacuum chambers that are individually pumped and connected to each other by stainless steel ports and by a bellow to the UHV chamber. Each chamber represents a differential stage where the pressure decreases by about an order of magnitude moving from the first stage to the third stage. Between each chamber, including that of the third chamber and the main chamber, installed are copper gasket collimators of about 2 mm in diameter. The collimators reduce the vacuum conductivity between adjacent chambers isolating them from one another and defining the three pressure stages. The collimators are also important so as to mitigate the beam divergence as it traverses its way to the main chamber. It is important that a molecular beam is properly collimated as its main advantage is the rapid and intense deposition of species on to the substrate mitigating the adsorption of impurities from the background [27]. This is in contrast to vapor deposition which is discussed in detail later. The beam lines converge at the position of the surface of the substrate (i.e. the geometric center of the main chamber), with an angular separation between the beamlines of 38 degrees with a tolerance that is within a fraction of a degree.

The first two chambers of each lines are evacuated by diffusion oil pumps backed by a large mechanical pump (Kinney). Each diffusion pump is separated from its vacuum chamber by a gate valve. To avoid backstreaming of oils from the diffusion pumps into the vacuum chamber, each pump has a cooled baffle and the gate valves are kept open only when there is a beam, thus assuring that there is a gas stream into the diffusion pumps. In the R line, the beam source is connected to the first chamber which is pumped by a baffled water-cooled Varian diffusion pump (VHS-6)

(1500 l/s).

The pressure in the first chamber is measured by a Varian tubular hot-cathode ionization gauge and it routinely reaches a pressure of the order of 10^{-5} Torr. The second chamber is pumped by a water-cooled diffusion pump with a liquid nitrogen trap, The pressure in the second stage is also measured by a Varian tubular hot-cathode ionization gauge and it routinely reaches the order of 10^{-6} Torr.

The third chamber in each line is pumped by a 90 l/s turbomolecular pump backed by a rotary-vane pump. Since each stage in each line is connected to the others by a collimator, the turbomolecular pump maintains a base vacuum condition when the beam is not in operation. The pressure in the third chambers of the beamlines is measured by two Instrutech cold cathode ion gauges (module CCM500) and is in the low 10^{-8} Torr range. The third chamber of the R-Line has a flag shutter installed that is controlled externally by a stepper motor so the beam can be blocked with rapid speed.

In the L-line, I designed and built a variable-aperture beam collimator that replaced the flag shutter. It allows for changing the aperture of the collimator from outside the vacuum (see Figure 6). As pointed out above collimation of a molecular or atomic beam is necessary to control its divergence. This principle can be illuminated further by considering the phenomenon of isentropic gas expansion. As a molecular or atomic gas leaves the nozzle of a beam source and begins its trajectory through the beam line it expands isentropically such that there is no transfer of heat or matter resulting in molecular or atomic speeds greater than that of the speed of sound (supersonic). It is important to note that in this description and going forward in this chapter that supersonic flow only occurs near the nozzle. This initial sprint however is broken by the fact that the expansion does not stay isentropic and collisions and recombinations occur within the beam. This non isentropic behavior can be mitigated and the integrity of the beam can be restored by collimating the beam [27] [28]. In the laboratory the matter of collimator sizes can be a revisionary task and often requires the breaking of the vacuum and the reinstallation of a brand new collimator. A variable collimator that can be controlled outside the vacuum eliminates this hassle.

The variable collimator consists of a 0 to 21mm diameter iris diaphragm (Edmunds). It is in the line of sight with the beamline collimators that are installed between the chambers. It is mounted in to an aluminum C-shaped holder which is connected to a UHV linear motion feedthrough (Huntington Model VF-108-1) with a high precision (+/-0.05 mm) micrometer positioning knob that allows a solid stainless steel rod to move in the z (vertical) direction. At the bottom of the stainless steel rod attached is a thin metal arm that connects with the arm of the iris. As the rod is manipulated from outside the vacuum by adjusting the micrometer positioning knob the metal arm moves

with it and if retracted; opens the aperture of the collimator wider and the opposite for extension of the rod. The variable collimator was calibrated before being installed in the third chamber by changing the setting on the positioning knob, measuring the diameter of the collimator with dowel pins and then fitting the diameter vs. micrometer position (see Figure 7) resulting in the calibration equation:

$$Y = 2.72X - 0.08 \tag{2.1}$$

Where X is the diameter of the collimator in +/- 0.1 mm and Y is the setting on the positioning knob in +/- 0.05 mm. The collimator is connected to an X-Y-Z micrometer positioning stage such that the entire piece of equipment can move in unison without effecting the iris arm or diameter setting. This is necessary in order to align the variable collimator precisely with the beam in the third stage.

2.4   Main Chamber

The UHV main 10-inch diameter chamber can be divided in two sections. In the lower section there is an 8" port that is connected to a pumping castle. At the bottom of the UHV chamber there is a 13.25 inch diameter flange that carries a quadrupole mass spectrometer. The QMS is placed in a housing that is inserted into the UHV chamber. The housing has opening for the beam to enter the QMS from the back and from the front in the upper section (see also below). The housing is pumped by a turbomolecular pump attached to the bottom of the rotatable flange. This arrangement allows to differentially pump the QMS, thus reducing the pressure in the detector even further. The bottom flange (Thermionics) is doubly differentially pumped by a turbomolecular pump and a rotary pump connected to the flange by flexible lines, so the flange can be rotated while maintaining UHV conditions in the chamber. The flange can be rotated 190 degrees around the sample by a Labview controlled High Torque Stepper Motor (Applied Motion HT34-486) equipped with a 451 lb-in speed reducer (Graham Circulute Model A47) which is paired with the sprocket edges of the flange by a comb style mechanical gear.

In the upper region the beams enter the UHV chamber via two gate valves and converge onto the sample attached to a holder connected to the closed-cycle liquid helium cold finger(see below). Two UHV high precision Varian leak valves are installed in this section.

The pumping castle is connected to the lower section of the UHV chamber. It has an air cooled 300 l/s turbo pump (Leybold 450i) backed by a 90 l/s turbomolecular pump (Pffiefer). There is also a 110 l/s ion pump (Varian model 921-0041), and a 10 inch diameter cryo pump. All pumps

can be sealed from the main chamber by gate valves. The pressure of the main chamber routinely reaches pressures the order of low 10^{-10} Torr and is measured by a Labview monitored nude hot ionization gauge that is installed in a port in the lower region.

Installed in the upper chamber are two Varian UHV high precision leak valves (see Figure 4), one being designated for deposition of specialty gases and the other for water vapor. Each leak valve is mated to its own stainless-steel VCR manifolds that are externally pumped by a separate pumping station that routinely gets the manifold pressures down to low $10^{-3}Torr$. The water leak valve manifold is equipped with an isolated 150 mL dewar in which distilled water is stored for vapor deposition. The gas leak valve can be used for pure gas or gas mixture deposition. For pure gas deposition a simple PVC connection from the manifold to a gas canister can be made. For gas mixtures, the gas manifold is equipped with and can be isolated from if need be a VCR sealed mixing manifold that is externally pumped by a separate pumping station (see Figure 8). Detailed descriptions of how water vapor and gas mixtures are introduced in the main chamber for the experiments described in this thesis are provided in chapter 3 and chapter 4.

2.4.1 Sample, Sample Holder, and Shield

Installed at the very top of the upper section of the UHV chamber is the sample manipulator. A doubly differentially pumped rotatable flange allows to change the angle of the sample with respect to the beams. On top of this flange there is a XYZ sample positioning manipulator (Huntington). Through it, a thermally shielded cold finger reaches the sample holder. On top, there is a closed cycle-liquid helium cryocooler (ARS model DE204) (see Figure 9). The sample holder unit is a solid oxygen-free, high conductivity copper block in which the 1 cm diameter gold coated copper sample is housed. Directly behind the sample there is a cavity in which a 25 Ohm cartridge heater is installed. The heater is chosen to be powerful enough so as to have a linear temperature ramp at the sample up to 200K. Higher temperatures up to 400K can be obtained without cooling. The temperature of the sample is measured by a silicon diode hall-effect sensor (DT-670) that is directly underneath the sample. This measurement is read and controlled with an accuracy better than 50mK by a Lakeshore 336 Temperature controller in tandem with a LabVIEW program. The temperature of the sample can be adjusted between 5 K and 300 K.

Finally, there is a copper shield installed around the sample holder unit such that it covers all but the sample itself leaving the gold surface exposed (see Figure 9). The purpose of the shield is to shield thermal radiation so that the substrate can reach a lower temperature than that of the shield itself. This arrangement also prevents adsorption of gases on to the sample holder or cold finger itself. In this way, only the surface of the sample receives deposition of atomic and molecular

gas species. The shield must not be in thermal contact with the sample holder or cold finger. We have found that this is an impractical ideal scenario and that despite our best ability to do so we cannot completely eliminate all thermal contacts, especially at very low temperatures, such as 10 K and below. As a remedy, we have developed a shield degassing procedure in which before cooling the sample to such low temperatures the cryocooler is powered down while the heater remains powered on. In the time that it takes for the sample to raise only a Kelvin or so the shield whose temperature is monitored by a thermocouple connection (seen in Figure 9 and 10) raises and degases. This is made evident by a rise in pressure in the main chamber as measured by the nude hot cathode ionization gauge mentioned previously. Once the shield has finished degassing (i.e. the pressure reduces) the cryocooler can be powered on and the sample can be cooled to deposition temperature. This allows for approximately a twenty minute window in which the sample is cold enough for species to adsorb on to its surface while the shield is not.

2.5   Signal Detection

The mid-IR (4000-650 cm^{-1}) vibrational spectra of ices composed of harmonically oscillating independent molecules on the gold surface of the sample is monitored by a Nicolet 6700 Fourier Transfer Infrared Spectrometer (FTIR) in the Reflection Absorption InfraRed Spectroscopy (RAIRS) configuration. Gold is preferred for the coating of the copper sample due its inert qualities which ensure that is does not play a catalytic role and its high reflectivity which ensures a strong FTIR signal. The optical path of the IR laser is as follows: it emerges from the spectrometer and enters a near air tight box in which its path is deflected by first a flat optical mirror (Edmund) and then a concave curved mirror (Edmund) (see Figure 11). It then enters the main chamber through a Potassium Bromide (KBr) vacuum view port where it strikes the sample with a grazing angle of 78 degree.

The optical path being almost parallel to the gold surface of the sample significantly strengthens the absorption intensity. This enhancement is a product of the interaction of the electric fields of the radiation and the conducting metal. Being that the electric field of the conducting metal only extend a very short distance from the surface a grazing angle is necessary to facilitate this key interaction. It is at this point in the optical path that a unique spectral fingerprint of the given species of ice is formed when certain frequencies of the infrared laser are absorbed [29]. Further details on how the spectra are acquired and analyzed are given in chapter 3 and 4.

Returning to IR laser optical path, after reflecting off the sample the laser leaves the main chamber through another KBr view port where it enters another box, is deflected again by another concave optical mirror and is directed into a liquid nitrogen cooled Thermo Electron Scientific

Corps detector head (type MCTA) (see Figure 11). The detector is paired with a computer and the spectra are collected using Omnic software. Spectra were measured and averaged every 20 s at a resolution of 1 cm^{-1}. All optical boxes are sealed with rubber o-rings and the entire path of the IR laser is purged of water vapor and carbon dioxide by constantly flushing the system with dry laboratory grade nitrogen gas. This is important as otherwise large water and carbon Dioxide background absorption bands will be present in the spectral features and hide experimentally meaningful signals.

The concentration of gases and vapor species in the vacuum are monitored by a Hiden Analytical QMS (standard PIC triple filter). The QMS setup consists of an in vacuum rotatable detector (type HAL 3F PIC) as discussed in the previous section, an RF preamplifier head that sits just outside the vacuum under the main chamber and a control unit that is connected to a computer and uses Hiden Analytical MASsoft software to collect data. The detector consists of four parallel metal rods that are electrically connected between opposing pairs (the quadrupole). An RF voltage with a DC offset is applied by the RF preamplifier head to each pair and ions that enter the detector either from the beam line, the gas phase, or desorbing from the sample will travel down the quadrupole between the rods. The ratio of the voltages applied to the rod pairs defines which mass to charge ratios (i.e. specific ions) are detected [30]. The ions that make it through the quadrupole rods are detected by an ion-counting secondary electron multiplier (SEM).

The detector is housed in a stainless steel cylinder with two entrance holes. One entrance hole is facing the sample and equipped with a teflon cone. The purpose of this cone is to maximize the flux of particles in to the QMS that would desorb from the sample in a Temperature Programmed Desorption experiment (TPD) and mitigate any false signal that might be due to desorption of particles that had adsorbed not on the sample itself but the sample holder unit, cold finger, or shield. This ultimately results in a bolstered signal to noise ratio. The other entrance hole is directly opposite and is aligned with the R-Line or L-Line if the detector is rotated to 0 or 38 degrees respectively. The QMS is aligned with a beamline often to test alignment of a beam source or in the case of the work presented in this thesis the dissociation percentage of an atomic beam.

2.6 In-Vacuum Helical Coaxial Resonator

In the following section, the in vacuum RF helical coaxial resonator mentioned in the first half of this chapter is explained in detail; the ultimate goal being the production of a gas dissociation source that will maximize the transfer of power from the RF power supply to the load. We will first calculate the plasma impedance by modeling the plasma as a circuit in which a resistor and an inductor are in series and inductively coupled to a coil following the work of Chabert and

Braithwaite [7]. We will apply this model to the molecular species N_2 and O_2. We will then turn our attention to the RF autotransformers as will be required for the stepping down of the very large plasma impedance in order to roughly match it to 50 Ω. This will give a unique and valuable insight in to how the turns ratio of the autotransformer relates to these two species. Both the plasma impedance and the turns ratio are calculated as a function of electron temperature and electron elastic collisional cross section. This will be followed by a close examination of the most optimal design parameters of the resonator as provided MacAlpine and Schildknecht [4]. Finally, test results and future recommendations for improvements and implementation of this piece of equipment will be shared.

A strong motivation for this project is the efficient dissociation of N_2 and thus the production of a powerful nitrogen atomic beam. As alluded to in the introduction of this project, atomic beams are critical to the study of the formation of molecules induced by deposition of elemental species such as H, O, and N as well as radicals on interstellar ice analogues. Particularly important is that of nitrogen bearing molecules and formation mechanisms of ammonia (NH_3); a key reactant in the formation of precursors to prebiotic molecules such as amino acids [31]. NH_3 is one of only a few nitrogen-bearing molecular species detected in interstellar ices toward YSOs and dense interstellar clouds [23]. This makes the surface chemistry of nitrogen bearing molecules and its role with regard to the formation of NH_3 a prime candidate for potentially revealing the link between simple species and life essential COMs found in the ISM. In order to explore this key area of research further in the lab a source of atomic nitrogen is required. Hiraoka et al performed TPD experiments of hydrogenated solid N_2 trapped within which were N-atoms and confirmed the formation of NH_3 [32]. McPherson et al confirmed that condensation of atomic carbon at 77 K on interstellar ice grain analogues composed of H_2O:NH_3 produces the amino acids glycine, N-methylglycine, alanine, beta-alanine, aspartic acid and serine [31].

Despite works such as these the surface chemistry of nitrogen bearing molecules remains largely unexplored and thus is poorly understood in the field [23]. This is largely due to the difficulty of dissociating N_2; typically a dissociation rate of only a few percent is achieved. The most pressing challenges to overcome in producing atomic nitrogen is the large bond dissociation energy and triple bond of N_2; the latter of which has the adverse effect of recombination at the walls of the glass source. This is not helped by poor impedance matching of RF circuitry and inefficient resonators many parameters of which are determined empirically. One such example would be the turns ratio or tap point of the helical inner conductor of the resonator (see Figure 12) which is key for impedance matching as it is the most impactful measure by which large impedance of the plasma is reduced [33] [8]. The resonator design and tests presented in this chapter address these

challenges. In an effort to move away from empiricism and to theoretically expound on the role of the turns ratio parameter I present a calculation of the plasma impedances for the gas species N_2 and O_2 and their relation to this parameter. In the interest of addressing plasma locality, the resonator is designed to be installed in vacuum at the end of the glass source near the orifice of the nozzle of the glass source as this mitigates the recombination of atoms as they traverse out of the source and in to the UHV environment (see Figure 12).

2.6.1 Plasma Impedance

Plasma is an ionized gas which is composed of electrons and ions that are subject to collective motion by an applied external electromagnetic fields. Most visible matter in the universe is plasma. We observe stars to consist largely of plasma as well as the interstellar medium where the plasma is cold and of low density [7]. Specifically, we are interested in radio frequency inductively coupled plasmas that are induced via coil systems. The resonant coil is designed to use the standard 13.5 MHz laboratory frequency that is provided by an RF power supply. The formation of the inductively coupled plasma can be viewed in two stages; low density known as the glow regime and higher density known as the filamentary mode [7]. When the RF power is initially applied to the coil the RF photons interact with the gas molecules and liberate electrons. This produces a low density plasma known as the glow regime in which the electron density and ion density are equal and thus is electrically neutral. The free electrons begin to bombard neutral molecules breaking the bonds and liberating atoms. While in the glow regime, the plasma is capacitively coupled between the adjacent coil turns. As an azimuthal RF field is established by the coil current in the low-density plasma, the ionization process is strengthened, and the plasma density increases. As the plasma is to be considered a conductive fluid in this state, it can be viewed as a collection of filamentary discharges that run parallel to the coil thus transitioning to what is known as the filamentary mode and becoming inductively coupled to the coil. We are then able to model the plasma as a one turn secondary coil of an air-core transformer [34]. In the filamentary mode a sheath is formed which is occupied by the ions. The electric and magnetic fields decay in the sheath giving a skin depth δ which is illustrated in Figure 13 and defined as:

$$\delta = \sqrt{\frac{2}{\omega \sigma_m \mu_o}} \tag{2.2}$$

where σ_m is the real part of the conductivity of the plasma:

$$\sigma_m = \frac{n_e e^2}{m_e(\nu_m + i\omega)} \tag{2.3}$$

where n_e is the electron density typically on the order of $10^{16}m^{-2}$ in the filamentary mode [7] and v_m is the electron elastic collisional frequency:

$$v_m = n_g \overline{\sigma} v_e \tag{2.4}$$

where n_g is number of molecules per unit volume which can calculated by the vacuum conductivity relationship:

$$P_s = \frac{Q}{C} \tag{2.5}$$

where P_s is the pressure inside the glass source after gas is introduced but before any power is supplied to the coil, Q is the volumetric flow rate of the gas in to the glass source which is controlled by an Alicat gas regulator and held at a constant 0.013 Torr*L/s. C is the vacuum conductance between the nozzle of the glass source and the first stage of the triply differentially pumped beamline. Taking the ideal gas law in to account we can re-express equation[2.5] and explicitly state n_g as:

$$N/V = n_g = \frac{Q}{K_b T C} \tag{2.6}$$

where T is the temperature of the gas before any power is applied to the coil which of course is room temperature. The vacuum conductance is given by:

$$C = A\sqrt{\frac{RT}{2\pi M_m}}t \tag{2.7}$$

where A is the cross sectional area of the beam nozzle which is on the order of $10^{-7}m^2$, R is the universal gas constant, and M_m is the molar mass of the gas species. The parameter t is the transmission probability for a cylindrical tube which in this case is represented by the nozzle of the glass source. This value of this parameter is dependent on the ratio of the length and diameter of the nozzle and for this geometry it was empirically determined to be 0.109304 [35]. Finally, this gives a vacuum conductivity of 0.087L/s which results in a number density for both O_2 and N_2 that is on the order of $n_g = 10^{21}\frac{molecules}{m^3}$ and a P_s value of approximately 150 mTorr.

Returning to equation [2.4], $\overline{\sigma}$ is the mean elastic electron collisional cross section which is reported by Itikawa [36] to be on the order of $10^{-19}m^2$ for N_2 and 10^{-20} for O_2 in the respective electron energy range of interest which is 10eV to 15eV and 5.5eV to 10eV or in terms of kinetic temperatures 116,000 K to 174,000 K and 63,855 K to 116,000 K. This range was determined by considering the fact that the electrons of interest with regard to dissociation must have an energy

greater than that of the bond-dissociation energy of N_2 and O_2 which is reported to be 9.79eV and 5.15eV respectively [37]. Finally, v_e is the average velocity of the electron given by:

$$v_e = \sqrt{\frac{8K_b T_e}{m_e}} \qquad (2.8)$$

where T_e is the kinetic electron temperatures discussed above.

At this stage the plasma must be maintained by the transfer of energy to the free electrons by the electromagnetic fields that decay within the sheath [34]. Thus, it is appropriate at this point to direct our attention to the calculation of the impedance of the plasma as modeled by Chabert and Baithwaite as a circuit in which a resistor and an inductor are in series and inductively coupled to a coil (see Figure 14). We begin by considering the impedance of the plasma alone and not taking the reactance of the coil in to account. My reasons for proceeding in this fashion are as follows; the mutual inductance of the plasma coil implicitly includes the coil inductance as will be explained shortly and is shown in Figure 14 as L_{mp} and secondly after reviewing Sibener et al. [8] one learns that any reactance from the coil is negated by a fine tuning process via an external π-network (see Figure 20) and that the crucial first step is to reduce the impedance of the plasma load; a process that is dependent on the square of turns ratio of the rf autotransformer coil [8]. In fact, Alagia et al. [33] whose design relied heavily on the work of Sibener's group claims that with an efficient enough turn ratio this pi-network may not even be necessary.

Taking in to account the parameters mentioned above we see that the collisional elastic frequency given by equation[2.4], v_m, is on the order of $10^9 s^{-1}$ while the angular frequency of the RF coil , ω, is on the order of $10^7 s^{-1}$. This justifies using the approximation of the plasma resistance for v_m greater than ω given by Chabert and Baithwaite as:

$$R_p = \frac{\pi r_o \omega_p}{\overline{\sigma} l c} \sqrt{\frac{2\omega}{v_m}} \qquad (2.9)$$

where ω_p is the characteristic plasma frequency given by:

$$\omega_p = \sqrt{\frac{n_e e^2}{m_e \varepsilon_o}} \qquad (2.10)$$

Next we consider the mutual inductance L_{mp} which is due to the RF positive ion current localized in the skin depth. We are assuming that we are in the filamentary phase so that the current only exists in the skin depth and as a result L_{mp} effectively mirrors the inductance of the coil except with the number of turns being equal to one and the radius being that of the source, r_o , giving:

$$L_{mp} = \frac{\mu_o \pi r_o^2}{l} \qquad (2.11)$$

We take in to account the inductance due to the electron inertia which follows from the imaginary component of the plasma conductivity [2.3], giving:

$$L_p = \frac{R_p}{\nu_m} \tag{2.12}$$

Giving the total inductance of the plasma to be:

$$L_{ptot} = \frac{\mu_o \pi r_o^2}{l} + \frac{R_p}{\nu_m} \tag{2.13}$$

which in turn gives the plasma impedance:

$$Z_p = R_p + i\omega_{pe}L_{ptot} \tag{2.14}$$

Taking in to account the parameters already discussed and the dimensions of the glass source the following parameters can be substituted in to impedance equation (2.14) as follows:

$$r_o \approx 0.02m \tag{2.15}$$

$$l \approx 0.075m \tag{2.16}$$

$$\omega_p \approx 5.63x10^9 s^{-1} \tag{2.17}$$

This gives the approximate plasma impedance as a function of electron kinetic temperature and collisional electron elastic cross section as:

$$Z_p \approx [3.42x10^{18}\sqrt{T_e}\overline{\sigma} + i652.232](\Omega) \tag{2.18}$$

The modulus is plotting using Mathematica and is shown in Figure 15 in the Electron temperature and collisional elastic cross region of interest for O_2 and N_2 collectively and respectively. As expected we see that impedance increases with large T_e and large $\overline{\sigma}$ and that it is considerably larger than 50 Ω requiring the need for an RF autotransformer. Notice that the impedance for cross sections falling in the $10^{-20}m^2$ range differs very slightly while the opposite is true for cross sections in the range of $10^{-18}m^2$ to $10^{-19}m^2$. This suggests that for sources possessing relatively large cross sections and electron temperature range, such as N_2 relative to that of O_2, the determination of an efficient turns ratio requires special attention and may be more difficult to dissociate than those of smaller cross sections and lower kinetic electron temperatures. This offers a validating note for the presented model as it is well known in the field that generating N atomic

beams of an appreciable dissociation are difficult to achieve and significantly limit studies of this astrochemically fundamental gas species [33].

2.6.2 RF Autotransformer

An rf autotransformer can either step up or step down the voltage across a given load. We will be focusing our attention on the step up transformer (see Figure 17) as this translates to a stepped down impedance of the load [38]. The voltage division equation is given by:

$$V_2 = \frac{N_T}{N_1}V_1 \tag{2.19}$$

Where V_2 is the secondary voltage applied across the plasma load, V_1 is the primary voltage applied to the inducting coil, N_T is the total number of turns and N_1 is the number of turns of the primary. Given the fact that $V_1 I_1 = V_2 I_2$ we get the following expression; $\frac{I_2}{I_1} = \frac{V_1}{V_2} = \frac{N_1}{N_T}$. In terms of impedance we can show $Z_1 = \frac{V_1}{I_1} = \frac{V_2 \frac{N_1}{N_T}}{I_1} = Z_2 \frac{I_2}{I_1} \frac{N_1}{N_T}$ [38] yielding the step up RF autotransformer impedance transformation relationship:

$$Z_1 = Z_2 [\frac{N_1}{N_T}]^2 \tag{2.20}$$

The plasma impedance is our load and we can define the following relationship:

$$Z_1 = Z_p [\frac{N_1}{N_T}]^2 \tag{2.21}$$

Where Z_p is the modulus of equation (2.18). Setting Z_1 to 50 Ω and solving for the turns ratio gives:

$$\frac{N_1}{N_T} = \sqrt{\frac{50}{Z_p}} \tag{2.22}$$

The turns ratio equation(2.22) was plotted in the same fashion as the plasma impedance and is pictured in Figure 16. As to be expected from the plasma impedance results, we see that the greater the cross section and the higher the electron kinetic temperature the smaller the required turn ratio. This makes sense because a smaller turn ratio means a greater step up of the voltage which translates inversely to a greater step down of the plasma impedance. Also, we see once again that for cross sections in the $10^{-20}m^2$ range there is a small difference in turn ratio as opposed to cross sections in the $10^{-19}m^2$ where the difference is more appreciable.

We must remember that assumed in this analysis is a constant electron density and thus also a constant characteristic plasma frequency via equation(2.10). Also, the collisional cross section

is electron energy dependent and thus a dynamic variable in the plasma manifestation process. It should also be reiterated that the equations used in the plasma impedance calculations are approximations. The figures presented in this thesis are meant to be guiding in nature and illuminate the mathematical relationship between the required turn ratio to step down plasmas of different gaseous variety.

There remains a valuable lesson to be learned from the trend present in these results. That is, there appears to be a ledge structure in the impedance and the turn ratio such that if a given source possesses a large enough average cross section, and electron temperature more finesse with regard to impedance matching may be required. Molecular nitrogen falls in to this category while molecular oxygen does not.

2.6.3 Coaxial Resonator with Helical Inner Conductor Design

We now move on to the coaxial resonator with helical inner conductor design as suggested by Macalpine and Schildknecht which consists of a cylindrical copper shell housing a helical coil whose rear is soldered to the shell. The shell is then connected to the shield of a straight coaxial resonator line or conventional coaxial cable grounding shell as well as the rear of the coil. The high voltage signal is passed through the surface of the shell to a tapped point which defines the turns ratio of the coil and gives the unit as a whole autotransformer properties with regard to a load (the plasma) that is inserted in to the resonator (see Figure 12). Macalpine and Schildkneckt produce design equations that allow all pertinent parameters such as coil length, pitch, etc. to be calculated for a resonator with a Q factor of several thousand. Figure 18 illustrates the most pertinent of these parameters. The equations have been experimentally verified to within +/- 10 percent [4]. The most important design equation is that of the Q factor which is defined as:

$$Q = 50D\sqrt{f_o} \tag{2.23}$$

Where D is the shield inner diameter in inches and f_o is the resonant frequency in mega cycles which as stated earlier is dictated by the RF power supply and is 13.56 mc or 13.56 MHz. The shield inner diameter parameter is limited by the size of the 1st stage of the beamline and has a maximum value which allows for slight motions so as to be able to adjust for alignment of approximately 3.6 inches giving a Q factor of 662.83 +/- 66.28. This result certainly does not meet the standards of Macalpine and Schildknecht who, for the sake of functionality, recommend a Q factor that is at least 1000 with an uncertainty of 10% taken in to account. In fact, in order to reach this target the inner diameter of the shield would only need to be increased by approximately three inches. However, this Q factor, while diminished, does allow for the constructed resonator

built for this project to be functional enough to illustrate the phenomenon appropriately and offer valuable guidance for future designs. All of the other parameters are calculated consequently from equation(2.23) and are illustrated in Figure 18 and described and listed in Table(4).

Finally, the resonator is connected to the RF power supply in tandem with an external Pi network that utilizes series capacitor arrangement. The Pi network is used for fine tuning and consists of one large inductor and two large variable capacitors. The Figure 20 represents the work of Sibener et al. [8] but is identical to this case with the exception of C_t. For the resonator presented in this thesis, C_t is fixed and represents the value of the capacitance between the shield and the helical coil. In the work of Sibener et al. it is representative of a variable capacitor that is external from the vacuum as the coil is not encased in a cylindrical shield. It is worth noting that the design utilized by Sibener et al. is stronger and more versatile as a variable value of C_t can offer a fine-tuning that is an advantage in impedance matching. Sibener's design, however, does require water-cooled RF lines which were not available to me and thus the reason I instead followed the work of Macalpine and Schildknecht [8].

2.6.4 Test Results and Discussion

The resonator was tested separately for 1.2 sccm of O_2 and N_2 with a turns ration of 0.2. As can be seen in Figure (19) when the resonators is powered on there is a reduction of the intensity of the beam with regard to O_2 and a directly proportional increase in atomic oxygen. A calculation of the area underneath the O_2 curve before and after gives a molecular dissociation of approximately 10 percent. While this result may be relatively weak compared to that of Alagia et al. who claims to have a molecular dissociation of 70 percent for O_2 it is nonetheless encouraging as it demonstrates the functionality of the constructed resonator [33]. Furthermore, it is well understood that with more space in the first stage of the beam line and thus a larger resonator the Q factor can be significantly improved along with the molecular dissociation percentage.

A figure for the dissociation test for N_2 is not included as the constructed resonator was completely unable to produce a N atomic beam. Given the relatively weak molecular dissociation of O_2 it comes as little surprise. It is worth noting, however, that the N_2 gas did glow a vibrant pink characteristic of high energy nitrogen plasma (see photo 21); in contrast to low energy nitrogen plasma which emits yellow light [39]. With this in mind, it is possible that there was an appreciable molecular dissociation but the beam suffered from recombination in the glass source. If this is indeed one of the underlying issues then it can be remedied by passing the beam through a nozzle tip composed of materials that are not prone to recombination such as teflon or aluminum oxide [26]. Another measure worthy of further consideration in future designs is localization of

the plasma directly behind the orifice of the nozzle; achievable by not only placing the resonator in-vacuum and at the nozzle tip as has been presented but also by the placement of a grounded aluminum block around the nozzle tip as is done by Sibener et al. [8].
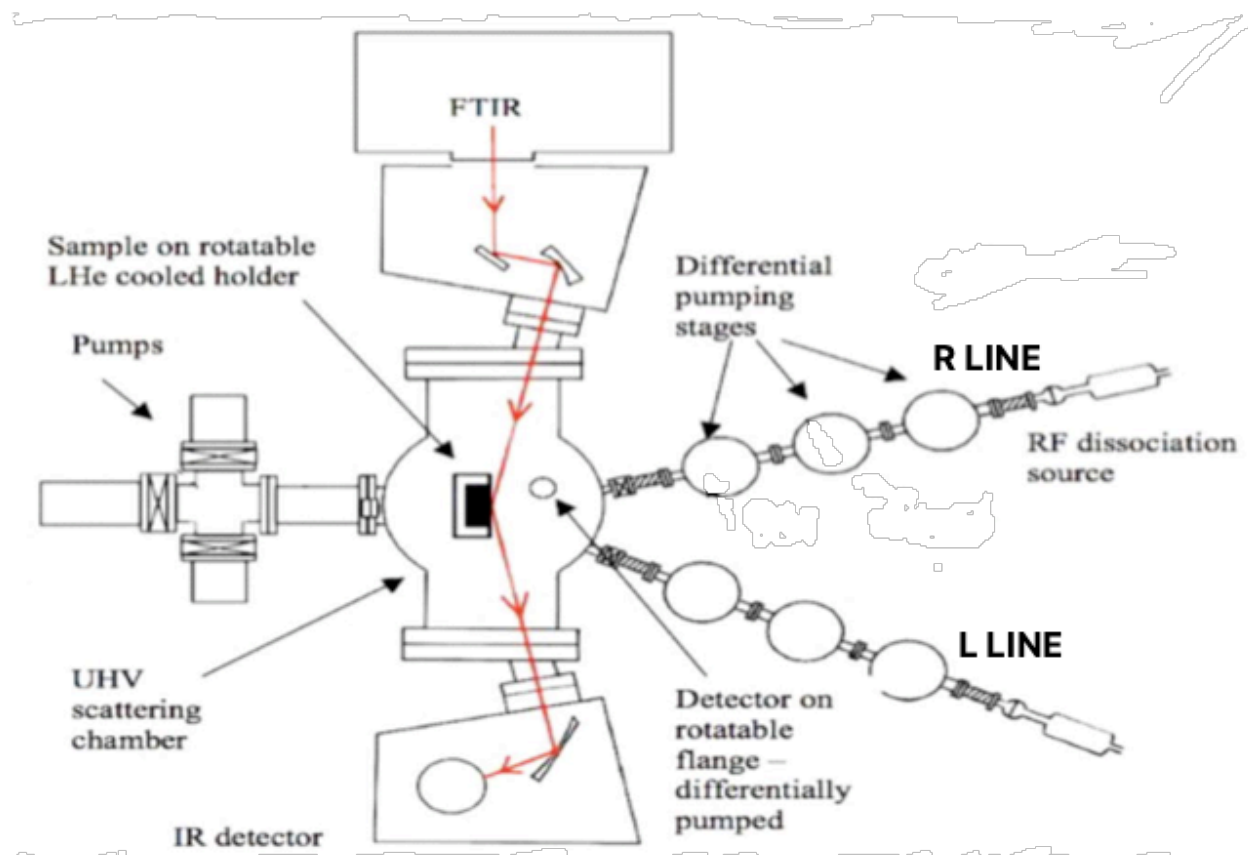
Figure 3: Top down view of the entire experimental apparatus. Details are provided in text. [6]
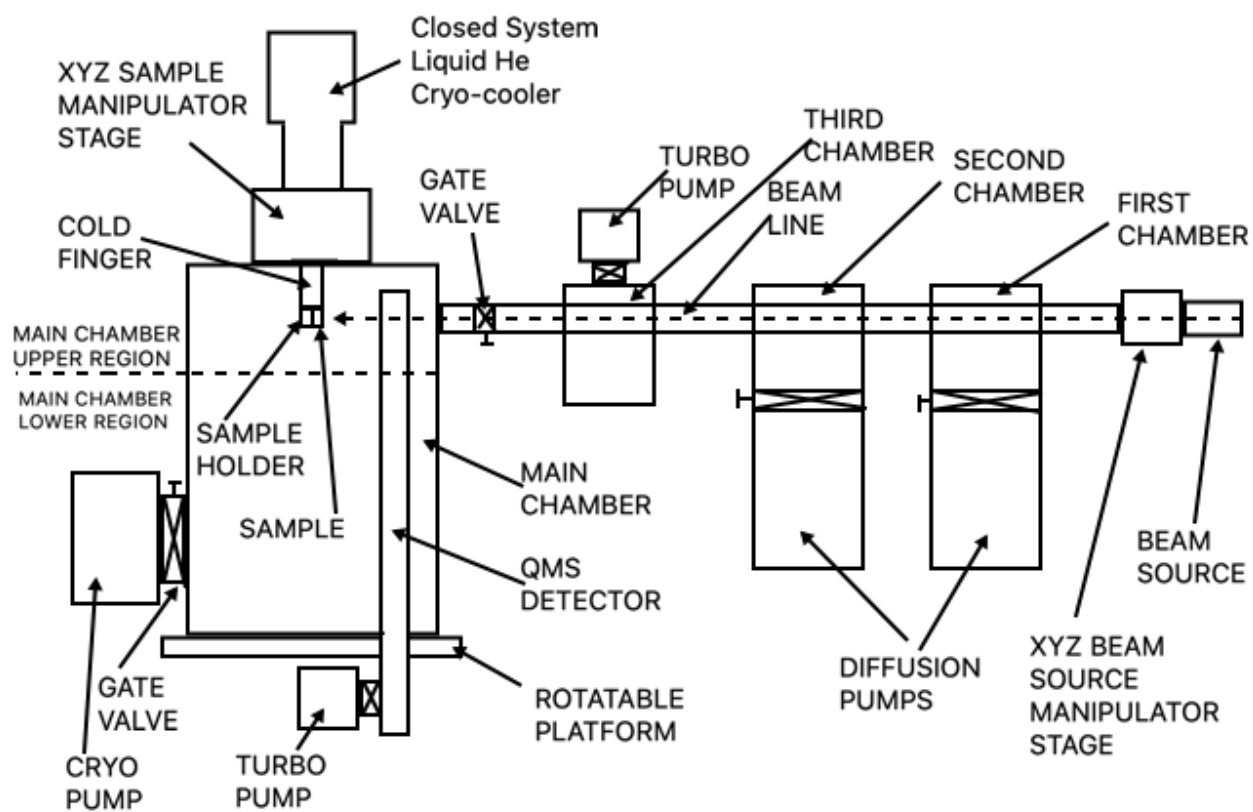
Figure 4: Side view of experimental apparatus. Details provided in text.
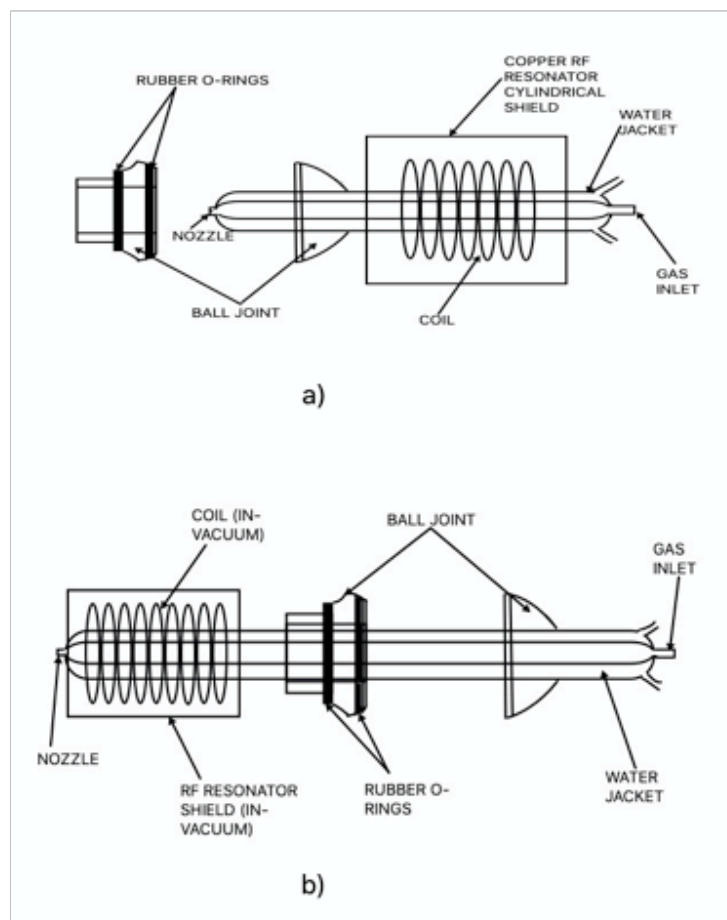
Figure 5: a) external R Line RF dissociation source b) internal L Line dissociation source.

ADJUSTER KNOB
(MOVES ONLY THE
LINEAR FEED
THROUGH ROD)

VACUUM
FLANGE

NON-VACUUM
VACUUM

XYZ
MANIPULATR
STAGE (MOVES
ENTIRE PIECE)

STAINLESS
STEEL TUBE

LINEAR FEED
THROUGH ROD

C-CLAMP

LEVER ARM

IRIS

IRIS ARM
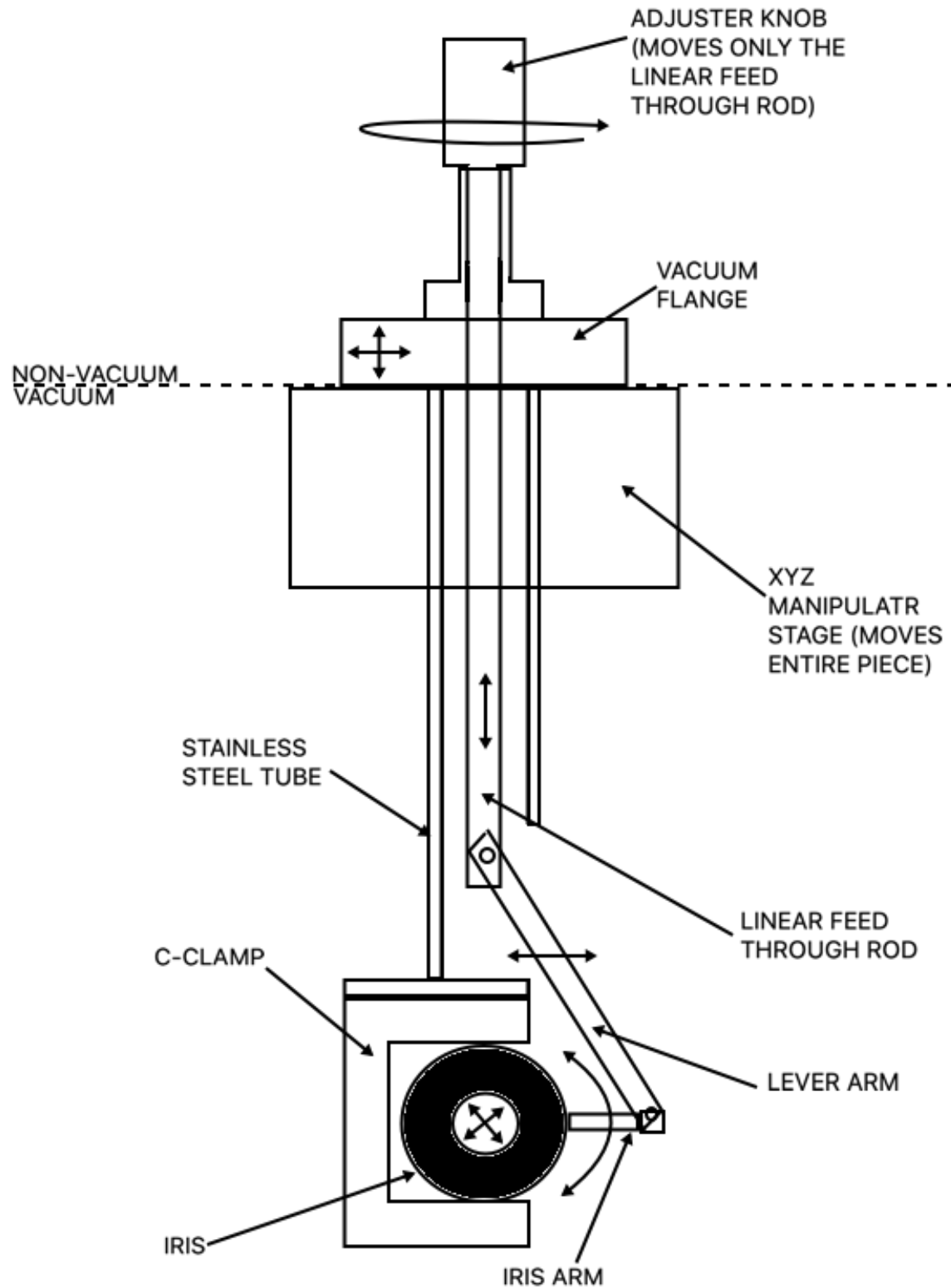
Figure 6: In-vacuum variable collimator design-installed in third chamber of L-Line.
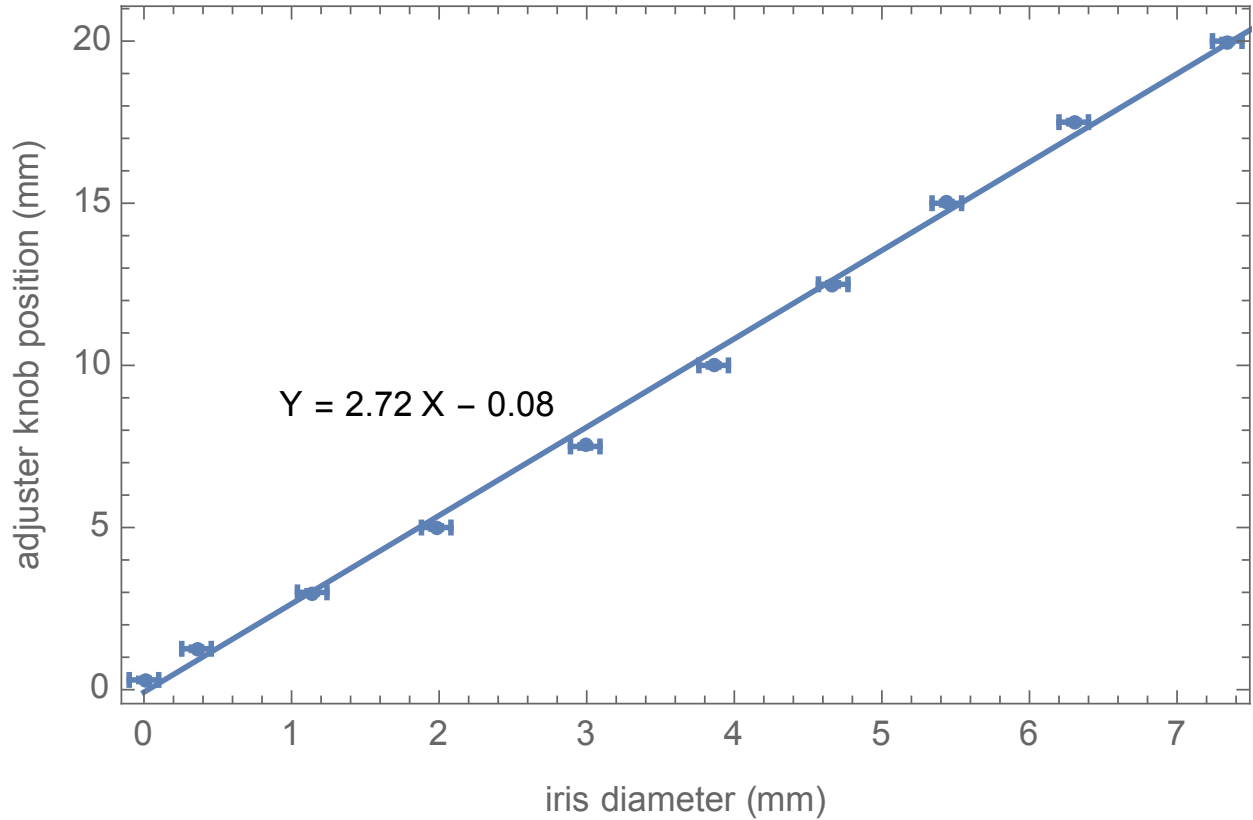
Figure 7: Calibration data and fit for in vacuum variable collimator.

Table 4: Calculated parameter values for resonator [4]

Parameter	Design Equation	Calc. Value
Diameter of shield (D)		3.6"
Resonance Frequency (f_o)		13.56 mc
Q-factor (Q)	$Q = 50D\sqrt{f_o}$	663
Number of turns (N)	$N = \frac{1900}{f_o D}$	39 turns
Pitch (τ)	$\tau = \frac{f_o D^2}{2300}$	0.76 in/turn
Diameter of turns (d)	$d = .55D$	1.98"
Axial length of coil (b)	$b = 1.5d$	2.97"
Length of shield (B)	$B = b + \frac{D}{2}$	4.77"
Maximum power that can be accommodated by resonator (P_m)	$P_m = 0.58D^3\sqrt{f_o}$	100 W
Power dissipated by heat (P_c)	$P_c = 2.32D^2$	31 W
Power delivered to gas (P)	$P = P_m - P_c$	69 W
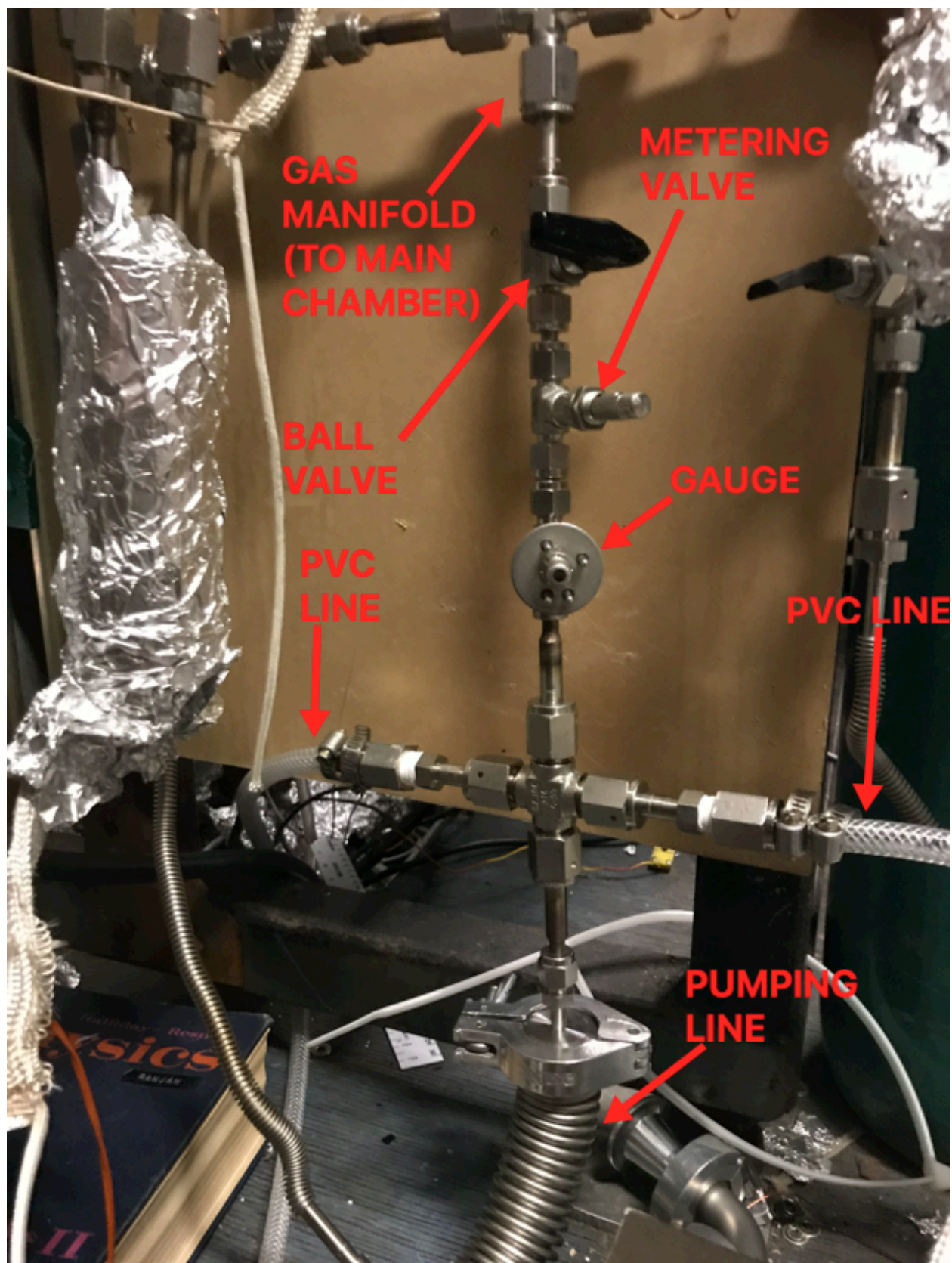
Figure 8: Mixing manifold connected to gas manifold.
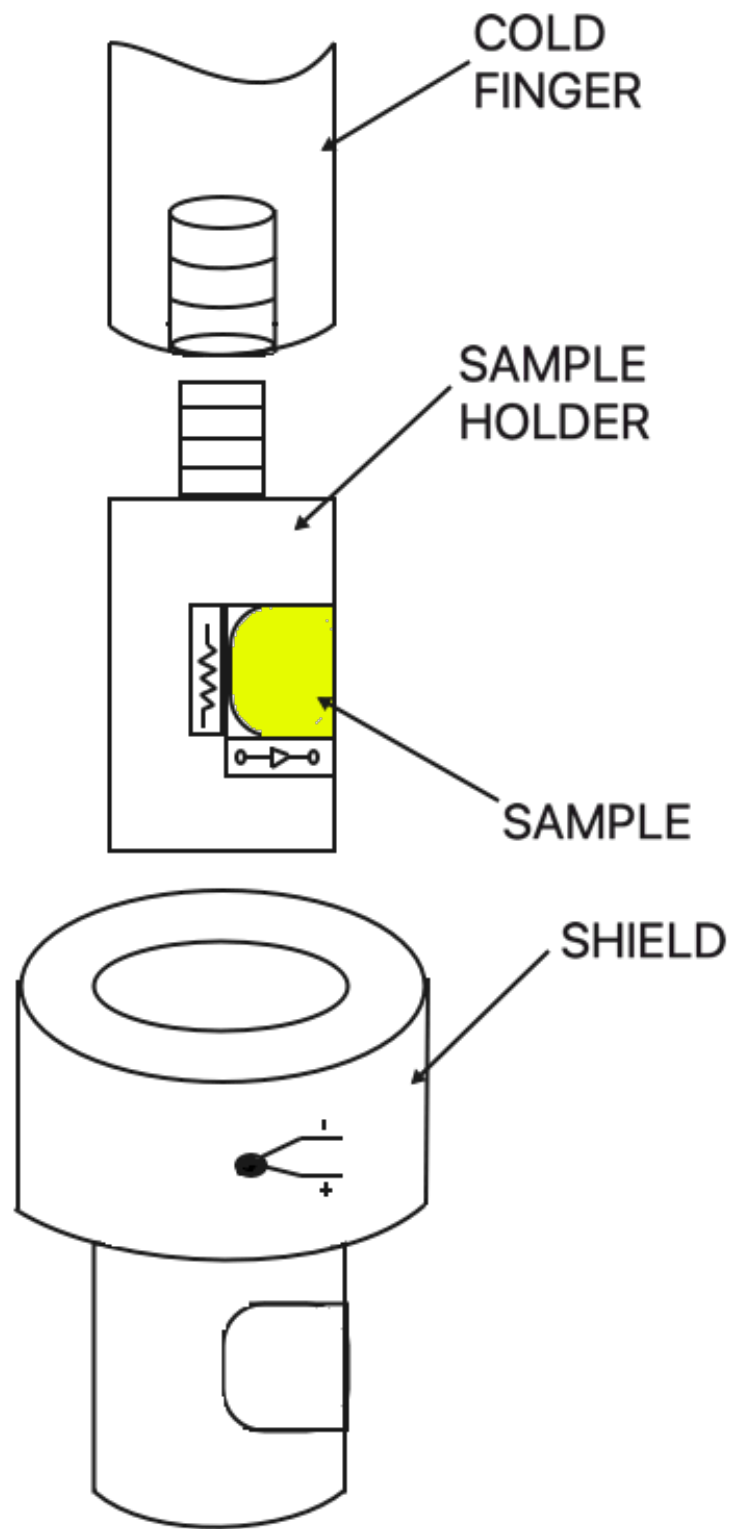
Figure 9: Sample, sample holder, cold finger and shield geometry.
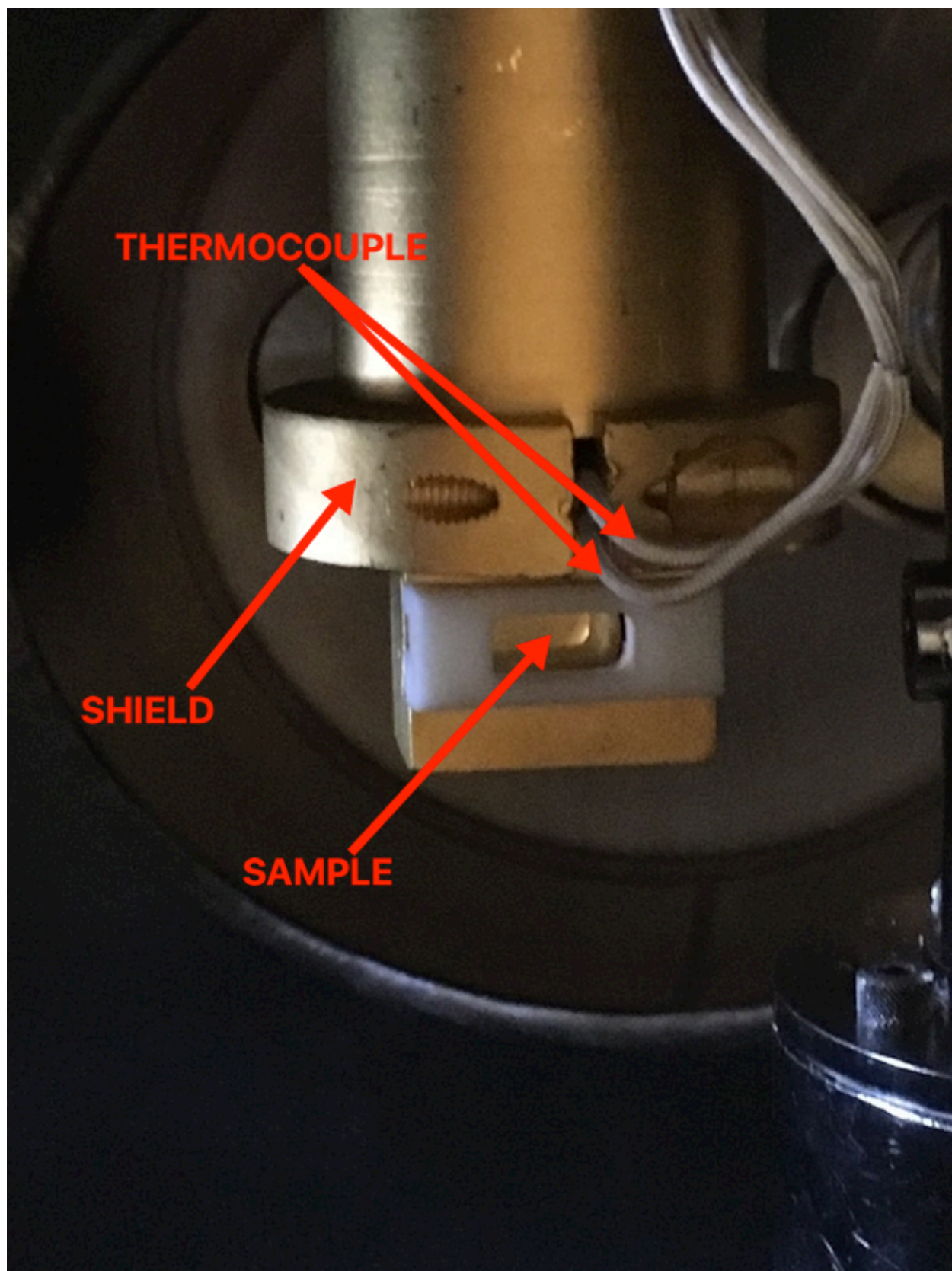
Figure 10: Photograph of shield when installed.
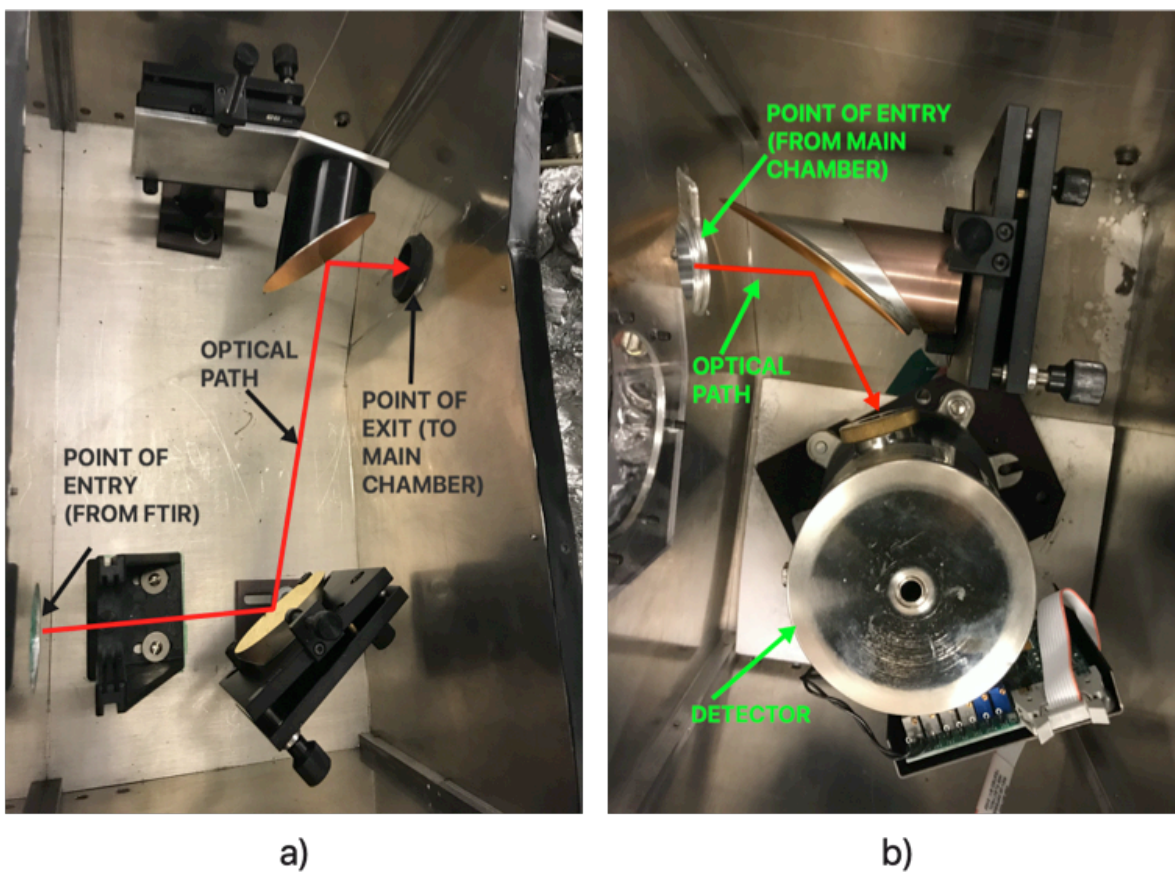
Figure 11: Optical path of FTIR laser.
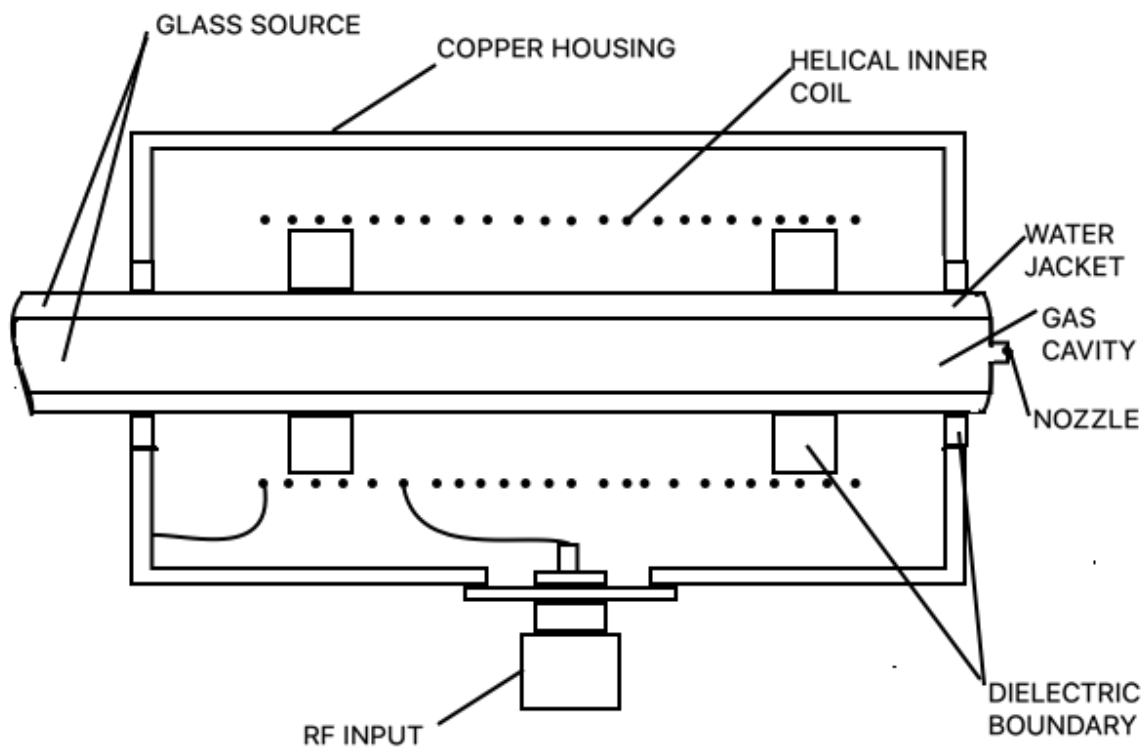
Figure 12: Coaxial Resonator with Helical Inner Conductor design with load pictured (not drawn to scale). Dimensions are provided in text.
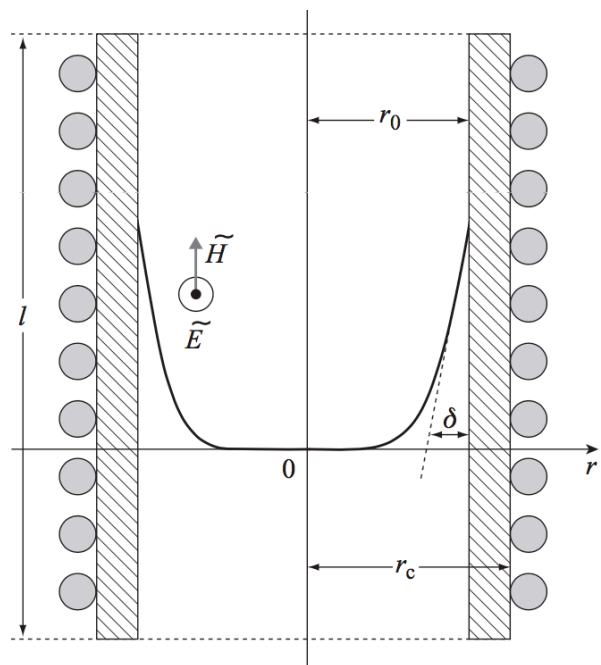
Figure 13: Plasma in filamentary mode where r_o represents the radius of the glass source, r_c represents the radius of the coil, and the shaded region is the dielectric boundary separating the coils from the glass source [7]
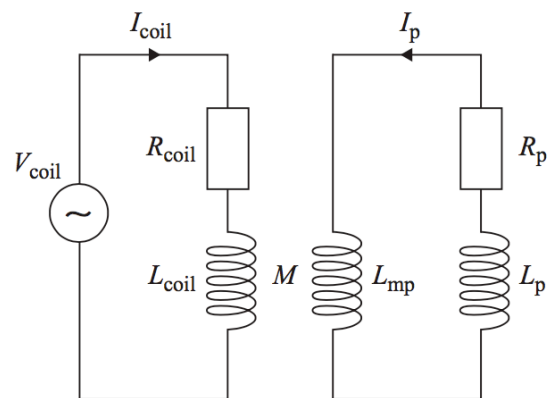
Figure 14: Plasma-coil model in which the plasma is represented as a resistor in series with two inductors one of which is coupled to the coil, L_{mp}, by mutual inductance M. [7]
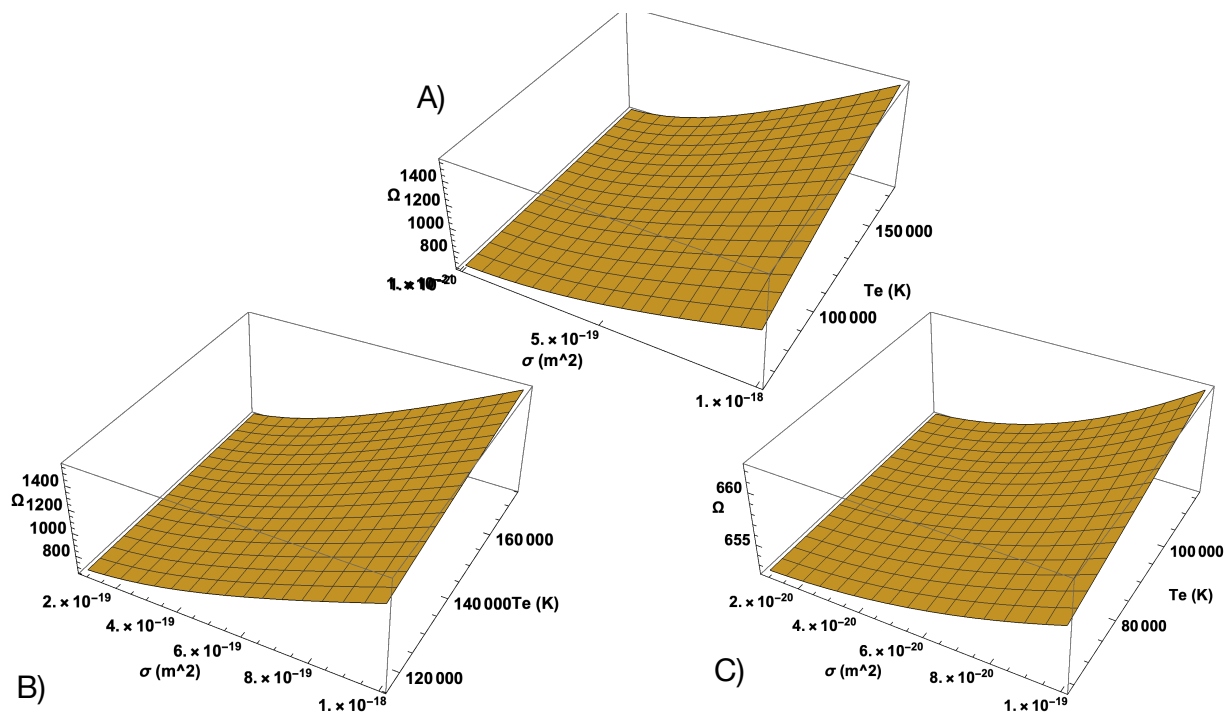
Figure 15: Plasma impedance as a function of collisional elastic cross section and electron temperature plotted for a) the entire region of interest for both N_2 and O_2 and b) only the region of interest for N_2 and c) the interest of region for O_2
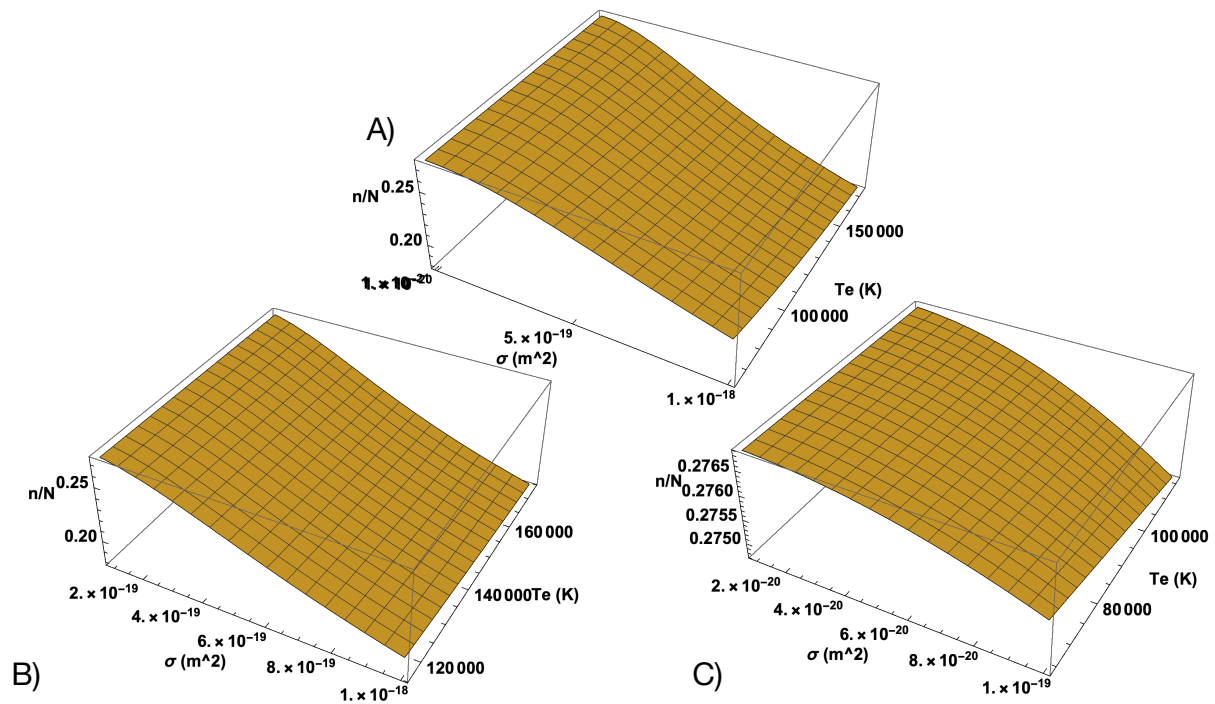
Figure 16: Turns ratio as a function of collisional elastic cross section and electron temperature plotted for a) the entire region of interest for both N_2 and O_2 and b) only the region of interest for N_2 and c) the interest of region for O_2
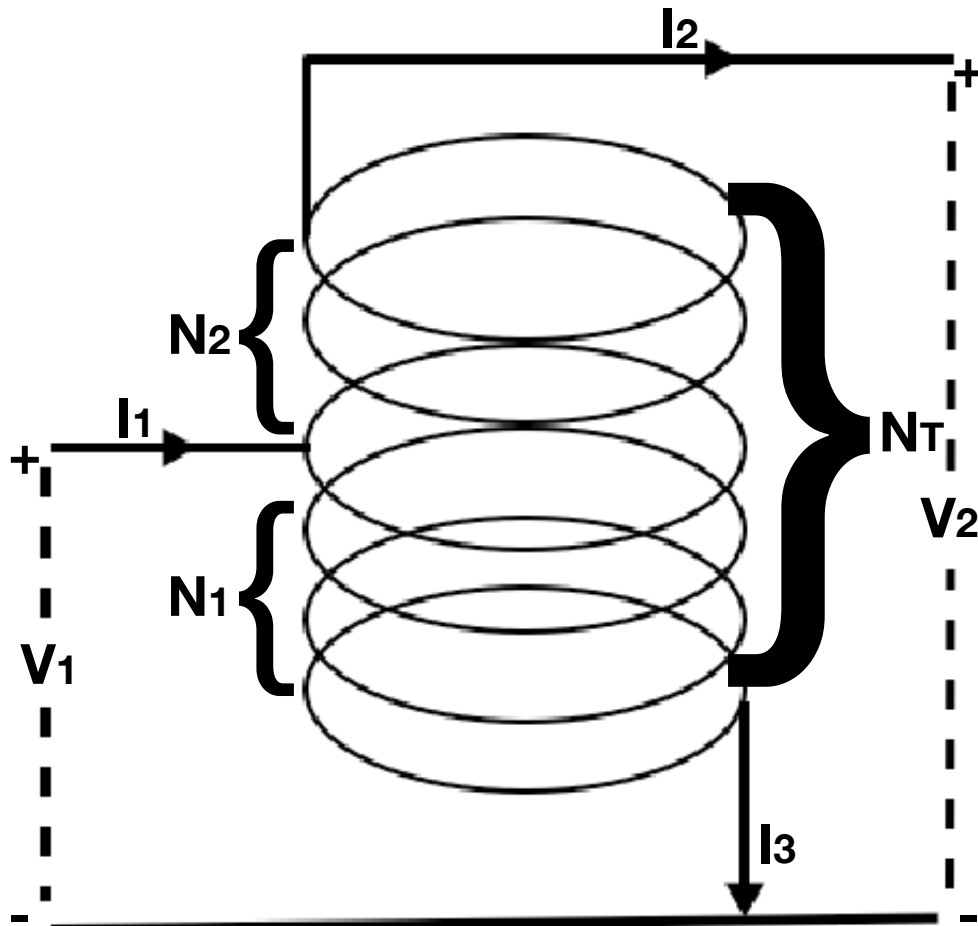
Figure 17: Basic circuit of a step up RF autotransformer
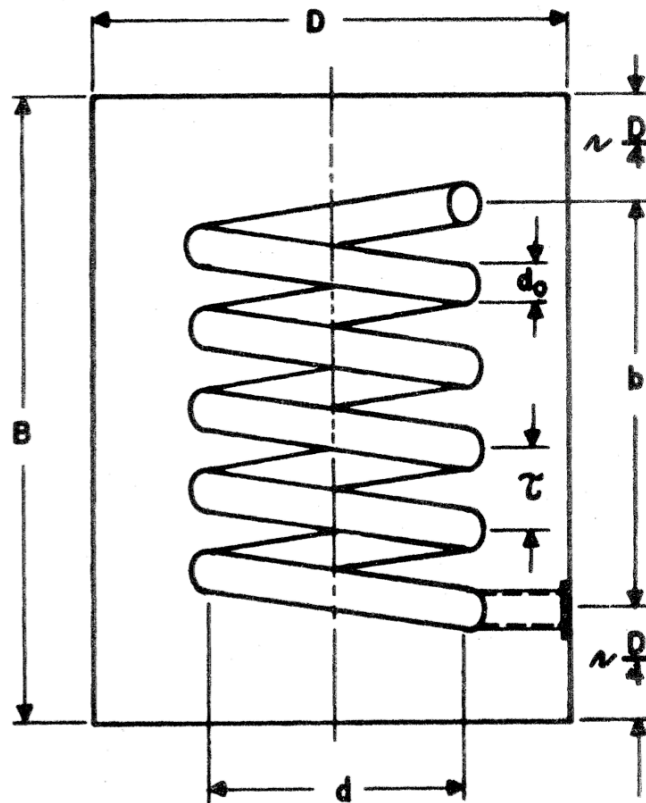
Figure 18: Parameters of interest for Coaxial Resonator with Helical Inner Conductor as provided by Macalpine and Schildsknecht [4]
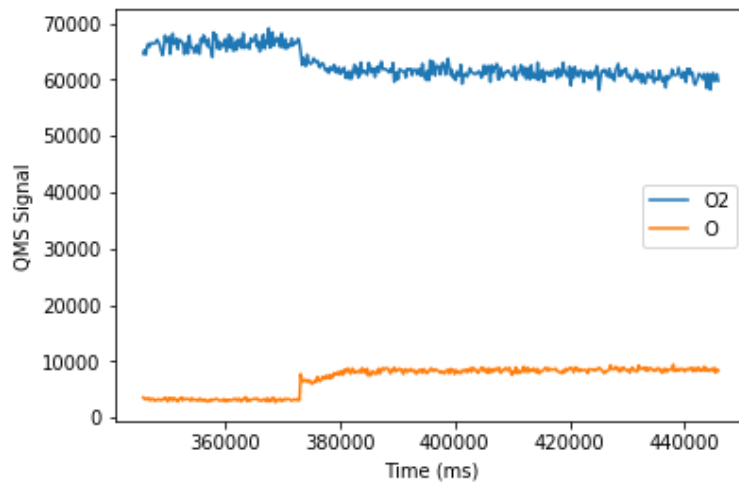
Figure 19: Dissociation test results for O_2 The marked decrease of O_2 and corresponding decrease of O are indicative of a $\sim 10\%$ dissociation rate.
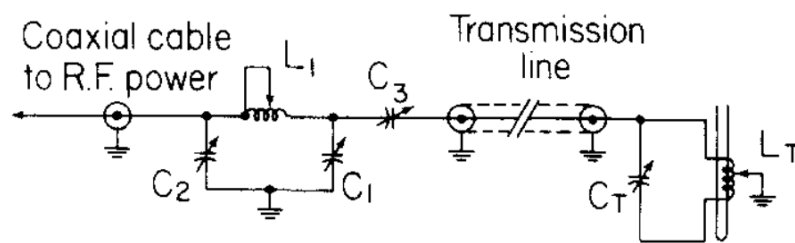
Figure 20: External impedance matching circuit with external Pi network used for fine tuning impedance matching of RF coaxial resonator. [8]
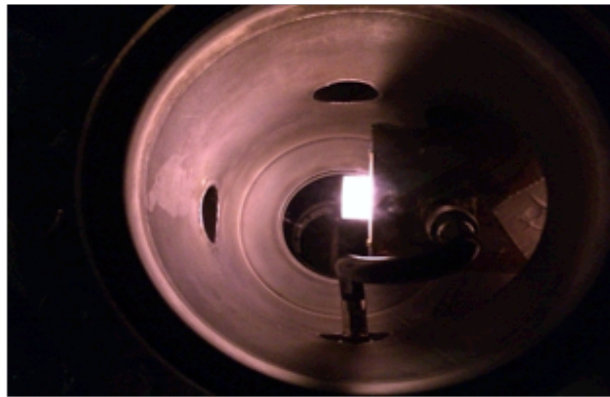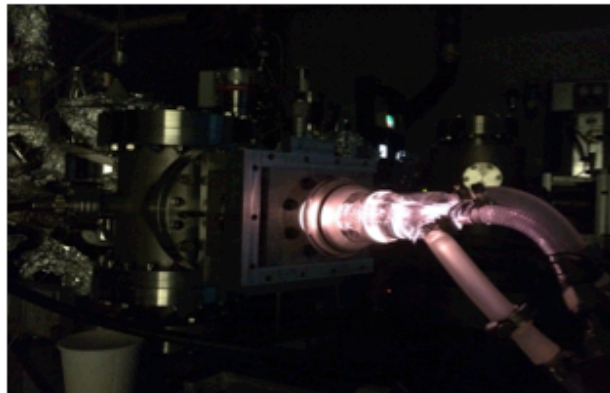
Figure 21: Photograph of dissociated N_2 gas a) in vacuum at tip of glass source b) outside of the vacuum at rear of glass source. The bright pink glow is indicative of high energy Nitrogen plasma as opposed to if the glow was yellow which would suggest low energy plasma.

Chapter 3

The Effective Surface Area of Amorphous Solid Water Measured by the Infrared Absorption of Carbon Monoxide

3.1 Introduction

The morphology of ice coated dust grains in dense interstellar clouds is crucial in facilitating the diffusion and storage of radicals and reaction products in ices. The ice provides a catalytic surface where atoms and molecules are stored and where reactions leading to the formation of many molecular species including complex organic molecules take place [15]. Yet, there is a considerable uncertainty about the structure of ISM ices, their ability to store volatiles and under what conditions. Particularly of interest is the catalytic role played by pore surfaces. Porous amorphous solid water (p-ASW) possesses a specific surface area up to a few hundred m^2g^{-1} and therefore may account for most of the catalytic surface on the dust grains [40].

A pore system is composed of microscopic voids between the molecules that make up the solid. These voids can cause some molecules in the solid to possess a deficit of covalent bonds with other water molecules. This defect is known as an immobilized free radical or dangling bond. Immobilized free radicals are reactive and unstable but more stable than mobilized free radicals due to their constrained kinetic environment and a phenomenon known as steric hindrance. Steric hindrance is a nonbonding intermolecular reaction in which, within a bulk, overlapping electron clouds provide a repulsive force that reduces chemical reactivity and slows decay rates. This results in immobilized free radicals having longer life times relative to that of mobilized free radicals [41]. Thus, important to the study of porosity is a careful examination of dangling

bonds. In fact, one useful signature of p-ASW is the presence of OH dangling bonds (dOH). Water molecules on surfaces of pores have approximately twice as many hydrogen bonds as covalent bonds around each molecule and can form two, three, or four hydrogen-bonds with neighboring water molecules. This is opposed to liquid water in which all molecules have at most one bond with neighboring molecules [42].These bonds are called one-, two-, three-, and four-coordinated. It is established that there are two types of dOH, for doubly and triply coordinated hydrogen-bonded water molecules at the ice surface [43]. Their presence is uncovered in the IR tail of the OH stretch, at 3720 cm^{-1} and 3696 cm^{-1} for doubly and triply coordinated water molecules, respectively.

Based on this information, it is conceivable to link the presence and strength of the dOH to the porosity of ice; however, this linkage has been proven difficult to establish through astronomical observation. As of now, observational evidence of dOH bands in ISM ices has not been found and this has led to the general consensus in the field that most ASW in the ISM is compact [44]. This consensus, however, is unsatisfactory in addressing a point of fundamental curiosity in molecular astrophysics; that being the formation, destruction, excitation, and storage of complex organic molecules.

Comets are often the source of this curiosity as the main component of comets is ASW; chemically stored in which is a pristine record of the composition of the solar nebula [45]. An explanation is lacking in the Rosetta mission detection of a number of molecules degassed from comet 67P/ Churyumov–Gerasimenko. Specifically, the detection of molecular oxygen at an abundance of 4% respect to water [46]. It has been argued that as the structure of the ice changes when the comet is exposed to solar irradiation, molecules can be trapped in the ice well beyond the temperature at which they would desorb if they were adsorbed on the surface [47, 48]. Bieler et al. [46] discussed the possibility of the comet undergoing molecular decomposition of water molecules by ionizing radiation resulting in the escaping of hydrogen and the trapping of molecular oxygen in voids or as otherwise interpreted closed pores. This work calls into question the ice morphology of comets, little of which is known, and the historical information they have to tell us about stellar evolution. It is possible that comets are composed of p-ASW in which molecules are trapped deep within open pores on inner surfaces of the comet or was porous at one point in its stellar evolution and compaction ensued trapping molecules in a lattice.

Furthermore, Oberg et al [45] observed the presence of simple and complex cyanides outside the water snow line in MWC480 protoplanetary disk. This finding suggests an unknown efficient disk chemistry by which large amounts of carbon originally in CO and other small molecules are converted into more complex organic molecules early in the disk's history (first million years). Agundez et al. [49] conducted radioastronomical observations of 9 dark clouds with the IRAM

30 m telescope and identified for the first time the presence of COMS; ketenyl radical (HCCO), ketene (H_2CCO), acetaldehyde (CH_3CHO), formyl radical (HCO) and propelyne (CH_2CHCH_3) in regions with high extinction. They argue that this discovery demands the revision of the chemistry of cold dense clouds and with regard to HCCO there must be a formation mechanism not previously considered that protects this radical from the efficient destruction through gas phase reactions with H, O, and N atoms. Efficient catalytic processes as provided by pore systems of interstellar p-ASW coated dust grains may offer useful insight into these observed phenomena.

Linkage between dOH bonds and porosity has also been proven difficult to establish unambiguously in the laboratory. Experimental studies [50, 51, 40, 52] show that the total number of dangling bonds is not proportional to the porosity, and some porosity is retained when the signature of dangling bonds disappears. This is an important point, since dOH IR signatures have not been seen in astronomical observations [53]. It is also known that the position and strength of dOH dangling bonds are affected by the presence of other atoms or molecules (see [54]) for a recent investigation of change in the IR bands of the dangling bonds due to adsorption of H_2, D_2, Ar, CO, N_2, CH_4, and O_2). Furthermore, the thermal treatment of ASW irreversibly changes the network of pores: as the temperature is increased, the ice morphology changes and pore collapse occurs. In this work, we investigate again the relation between dOH bands and porosity, and hope to find new insights into this decades-old problem.

In typical laboratory experiments under UHV conditions, the structure of ASW as porous or compact depends on the deposition methods [55, 56, 57, 58]. Generally, lower deposition temperature and higher deposition angle respect to surface normal favor a higher porosity. If ASW is grown from water vapor deposition onto a substrate at 130 K or above, the ice is compact. It was also reported that ASW grown from a collimated beam of water vapor at normal incidence forms a compact structure even at lower temperatures [56]. Omnidirectional deposition of water vapor when the substrate is at lower than 130 K forms porous ASW. Upon heating, porous ice gradually transforms into non-porous ice. This temperature dependence is explored in detail in the Results and Analysis section of this chapter.

Compared to the studies mentioned above, which mostly focused on measuring the porosity (or equivalently the density) of the ASW, fewer details are available about the link between morphology and catalytic properties of ices. Raut et al [51] performed energetic ion bombardment of ASW and found that the surface area of porous ice decreases at a faster rate than the pore volume during ion-induced compaction. The underlying reason for this difference is still not well understood, but several mechanisms have been proposed, including coalescence of micropores, preferential

destruction of smaller pores, and smoothing of pore wall topology [51]. Prior laboratory measurements of porosity based on density [59, 60] do not reflect the true catalytic potential of the ASW surface. It is important to measure the pore surface area that is accessible for the adsorption of volatiles from the gas phase. Palumbo et al [50] studied the accessible pore surface area after compaction of the ASW by energetic ions. However, in highly shielded gas clouds in the ISM, thermal processes should dominate over energetic processing, and the temperature dependence of the pore surface area is the most important.

Taking the above arguments and questions of interest in the field as motivation we use CO as a tool with which to probe p-ASW ice and the resulting infrared absorption spectrum to quantify the temperature dependence of the pore surface area of ASW that is accessible by volatile molecules condensed from the gas phase. Furthermore, we investigate the affect that the presence of volatiles in the ASW matrix have on dOH by applying the same methodology to ASW with the minority species of NH_3 and CO_2 (treated separately). We also present results obtained from a Monte Carlo model of ASW in which the morphology of the ice is visualized and quantified. The simulations were done by Robin Garrod and his student Aspen Clements of the University of Virginia in a joint collaboration [61].

3.2 Experimental Procedure

A detailed description of the Syracuse University Laboratory of Astrophysics and Surface Science UHV apparatus is given in chapter 2 of this thesis, and here only the main features that are relevant to this study are summarized. Ices are grown on the gold coated copper disk sample by vapor deposition from the chamber background when the sample is cooled to 10 K. Gas and water vapor enter the chamber via two separate manifolds attached to UHV precision leak valves, which are automated by stepper motors controlled with LabVIEW programs.

Water vapor is produced in a stainless-steel gas manifold that is connected to one of the leak valves on one end and an isolated 150 ml dewar on the other end. The procedure for depositing water vapor comprises: 1. Pumping down the manifold with an external pumping station to approximately 2 mTorr range; 2. Wrapping the manifold in heating tape and aluminum foil to heat the manifold so that it is hot to the touch - this prevents water vapor from stick to the walls; 3. Depositing distilled liquid water in to the dewar; 4. Wrapping the dewar in fiberglass heating tape and aluminum foil and heating the dewar so it is hot to the touch; 5. Preparing an isolated nearby sorption pump by cooling it with liquid nitrogen; 6. Isolating the pumping station from the manifold and then disconnecting the pumping station; 7. Connecting the sorption pump in place of the pumping station (still isolated from manifold) and exposing the water dewar to the gas manifold,

effectively filling it with hot water vapor; 8.After about 20 seconds, isolating the water dewar so as not to inundate the manifold; 9. Opening and controlling the leak valve via a LabVIEW program and stepper motor and beginning deposition (the program will automatically close the leak valve once target thickness is reached); 10. After deposition is complete, pumping down the manifold with the sorption pump (this is necessary as the water vapor would inundate and damage the pumping station); 11. Once a pressure of approximately 40 mTorr is reached, isolating the sorption pump and disconnecting it and reconnecting the pumping station in the place of the sorption pump (still isolated). For ice mixtures, this procedure differs only in that NH_3 and CO_2 are co-deposited individually in separate experiments through the gas leak valve at the same time that the water vapor leak valve is being operated. A different LabVIEW program is used that takes both species and leak valves in to account.

In all experiments, CO is deposited after the deposition of water vapor or water vapor mixtures. The deposition procedure for depositing CO comprises: 1. Pumping down the gas manifold with an external pumping station until the manifold reached a pressure of approximately 2 mTorr; 2. Isolating the pumping station from the manifold; 3. Introducing 20 psi of laboratory grade CO gas to the manifold; 4. Opening the leak valve via LabVIEW program and stepper motor and beginning deposition (the program will automatically close the leak valve once target thickness is reached); after deposition is complete pumping down the manifold with the external pumping station.

Ice thickness in monolayer (ML) are calculated from the impingement rate based on an integration of the chamber pressure [54]. One monolayer is defined as 10^{15} molecule cm^{-2} on a flat surface. The ion gauge correction factor and velocity of both water and CO were taken into account in the calculation. The relative uncertainty in CO dose and water dose are less than 0.1% and 1%, respectively. The main source of uncertainty is from the hot cathode ion gauge, which has absolute uncertainty up to 30%. More details of the deposition control are reported in He et al [54]. Spectroscopic features of the ice on the sample is measured using a Fourier Transform InfraRed (FTIR) spectrometer in the Reflection Absorption InfraRed Spectroscopy (RAIRS) configuration as is discussed in more detail in chapter two signal detection section.

In the first experiment we deposited 200 ML of porous ASW when the surface was at 10 K as described in the above procedure, then heated the ice at a ramp rate of 3 K/minute from 10 K to 200 K. The RAIR spectra were measured continuously during the heating and we monitored how the two dOH bands evolved with changing temperature. Next, we carried out a whole set of experiments of CO deposition on top of 200 ML of ASW ice annealed at different temperatures. The ASW samples were grown when the sample was at 10 K as described in the procedure above, and

then annealed at 20, 40, 60, 80, 100, 120, and 140 K for 30 minutes. Afterwards, the ice sample was cooled down to 20 K (except for the 20 K annealing) before depositing CO continuously until the ASW pore surface was fully covered by CO, as indicated by the emergence of the longitudinal optical (LO) mode of CO at ~ 2143 cm^{-1}. The optical (LO) mode is the typical one that is excited in the grazing mode geometry as it is representative of the vibration of molecules parallel to the surface as opposed to the optical transverse mode (TO) in which case the molecules vibrate perpendicular to the surface. The dOH bands were also continuously monitored during these experiments so as to measure how the these spectral features change when CO is deposited. The CO deposition rate was chosen so that there are enough data points during the deposition, and it varies between experiments. The CO deposition temperature was chosen to be 20 K, because at this temperature, CO has enough mobility on the surface of p-ASW ice [54]. Finally, a Temperature Programmed Desorption (TPD) was then done by heating up the sample from 20 K to 200 K at a ramp rate of 0.1 K s^{-1}. Spectral information was collected during the TPD and was used to correlate temperature dependence of the dOH bands with that of CO features to effectively show the trapping of CO in ASW ice (more details in the Results and Analysis section).

3.3 Modeling

Ice simulations are conducted using the off-lattice microscopic kinetic Monte Carlo model *MIM-ICK* (Model for Interstellar Monte Carlo Ice Chemical Kinetics), adapted from the works of Garrod et al [62] and Clements et al [63], with flat geometry and periodic boundary conditions. For studies involving porosity an off-lattice modeling approach is necessary as it offers a three-dimensional treatment of the dust grain. This approach is opposed to on-lattice techniques in which the grain surface is two dimensional and the atoms and molecules are not free to adapt to local conditions and may only diffuse between pre-defined lattice positions. The limitations given by the on-lattice approach are unacceptable for studying p-ASW as they do not allow for the investigation of the effects of large-scale grain morphologies on the surface chemistry and ice structure [62].

The model allows the diffusion of individual molecules to be traced over time, at various temperatures. As well as thermal diffusion (hopping) between surface potential minima, non-thermal diffusion is also allowed, immediately following the deposition of each water molecule onto the surface; the gas-phase translational energy of the molecule and the energy it gains as it enters the surface potential allow it to diffuse if its energy is sufficient to overcome the local diffusion barrier(s). The model uses isotropic Lennard-Jones potentials, which were parameterized within the model by Clements et al [63] using experimental density data from the literature for amorphous water formed through background deposition at various temperatures [64]. More specifically, the

model uses the Lennard-Jones potential to calculate local minima in effect determining the position of the water molecules after adsorption or diffusion on the grain surface [63].

The Lennard-Jones Potential represents the interaction between a pair of molecules by:

$$V = 4\varepsilon[(\frac{\sigma}{r})^{12} - (\frac{\sigma}{r})^6] \tag{3.1}$$

Where r is the distance between interacting molecules, ε is the depth of the potential well, and σ is the optimal distance between molecules; a finite distance at which the potential is zero. The second term that is to the sixth power accounts for the induced dipole-induced dipole attraction (Van der Waals Force) between the molecules. The first term the twelve power accounts for the close-range repulsion of molecules due to overlapping electron shells; a phenomenon known as Pauli Repulsion. This effect was already touched on in the introduction section of this chapter in the discussion of pore systems and their relation to dangling bonds and steric hindrance [41].

In the present models, water is deposited at interstellar dust grain temperatures (10 to 20 K) and then heated at laboratory rates (1 to 3 K min^{-1}) up to a temperature of 150 K. First, the water molecules are deposited using background deposition onto a square surface of length 650 Å, significantly smaller than a surface used in the experiments for computation time. A deposition rate of 10^{13} cm^{-2} s^{-1} and temperature of 10 K were used and two thicknesses were tested (25 ML and 200 ML). Surface area and density are calculated for each ice and measured during heating. The ice surface area (including pore surfaces) is calculated by counting the number of surface molecules. This value is then divided by the total number of water molecules in the ice. This ratio corresponds to the coverage of the surface to the total ice thickness in monolayers. With the microscopic model the surface coverage can be directly measured. An average of the thin ice (25 ML) and the thick ice (200 ML) was averaged to calculate the pore surface, as we later discuss the surface area is dependent of thickness between 10 to 200 ML. This method of calculating the pore surface area is comparatively more direct in comparison with how it is done experimentally through measuring the emergence of the longitudinal optical (LO) mode of CO at ~ 2143 cm^{-1} (see Experimental Setup section of this chapter) and thus puts our laboratory data to a rigorous and meaningful test. Images were created using the freeware POV–Ray to visualize the entire ice or, using cross sections, the connectedness of the pores.

3.4 Results and Analysis

3.4.1 Infrared Characterization of Pure ASW

We begin by examining the infrared spectral features of the dOH bands of 200 ML of ASW ice when no CO is deposited. This first phase of study is important as the interaction of CO with porous ASW ice has its own distinct effect of shifting the dOH bands [54]. Thus, in order to clearly understand the phenomena of temperature dependence of the ASW ice and the effect of CO deposition we must be able to distinguish between the two.

ASW has three main vibrational modes in the mid-infrared region: OH stretching at ~ 3300 cm^{-1}, bending mode at 1640 cm^{-1}, and libration mode at ~ 700 cm^{-1}. On the blue shoulder of the OH stretch band, there are two small absorption features at ~ 3696 cm^{-1} and ~ 3720 cm^{-1}, generally attributed to 3-coordinated and 2-coordinated water molecules, respectively [43]. These features are the dOH bands and contain important information regarding the pore structure of the ASW. The dOH region of the RAIR spectra of the 200 ML ASW during heating is shown in Figure 22. As the ice temperature is raised, both dOH bands decrease. By 60 K, the 3720 cm^{-1} band is almost gone, while the 3696 cm^{-1} band persists until above 140 K.

To quantify the temperature dependence of both bands, we use two Gaussian functions to fit the two dOH bands. Gaussian and Lorentzian functions are very often used to fit solid state infrared absorption features. Typically, disordered ices have relatively broad Gaussian line shapes, while crystalline ices have narrower Lorentzian line shapes. This is due to the fact that the molecules in disordered ices, ASW ice being an example of such, experience a statistical distribution of environments which results in a more diverse collection of vibrational energy states and thus a softer and broader peak that upon wider view reveals a bell curve or Gaussian profile. This is a direct consequence of two fundamental facts of IR spectroscopy that the line shape originates from the sum of all the individual vibrations and the exact vibrational frequency of a particular molecule is controlled by its environment [65].

We tried (1) one Gaussian; (2) one Lorentzian; (3) two Gaussians; and (4) one Gaussian and one Lorentzian functions to fit the blue side of the OH stretch peak; the two dOH bands are also included in the fitting. Figures 23 and 24 show the fitting and the residuals, respectively. It can be seen that the fitting using one Gaussian and one Lorentzian, in addition to two Gaussians for the dOH bands achieve the best results. For analyses that do not require high accuracy, one Gaussian function also fits the blue half of the OH stretch well. In the remaining of this work, we use one Gaussian and one Lorentzian to fit the OH stretch band. Based on the above fitting scheme, the band areas of both dOH bands during warming of the 200 ML ASW are calculated and presented in

Figure 25. At ~60 K, the 3720 cm^{-1} band becomes negligible, which suggests the disappearance of 2-coordinated dangling bonds. This is consistent with previous experimental studies [51, 66, 67]. The 3696 cm^{-1} band drops linearly with temperature from 60 K to above 140 K. The residual 3696 cm^{-1} band at above 140 K is largely due to the dangling bonds located on the outer surface [66].

3.4.2 Infrared Characterization of ASW:NH$_3$

We turn our attention to the infrared spectral features and temperature dependence of the dOH bands of 200 ML of ASW at 3720 cm^{-1} and 3696 cm^{-1} when the minority species NH$_3$ is present in the ASW matrix. This is important as stated in the introduction of this chapter; it is well known that the presence of minority species in the ASW matrix has its own unique effect on the dOH bonds. Furthermore, NH$_3$ is a minority molecule of particular interest given it is a volatile commonly detected in the water rich layer of ice coated dust grains in the ISM.

Figure 26 shows the dOH spectral features for ASW with 0%, 10%, and 20% NH$_3$ present. We observe a marked decrease in the two-coordinated 3720 cm^{-1} immediately upon the presence of NH$_3$ before thermal energy is imparted to the ice during heating. The presence of NH$_3$ causes the two-coordinated water molecule bonds to vanish from the ASW matrix. The 3696 cm^{-1} dOH feature is also significantly diminished in intensity by the presence of NH$_3$. It quickly vanishes upon application of thermal energy.

We performed an identical fitting of the dOH band at 3696 cm^{-1} as was done in the last section. Figure 27 shows the band area of the three-coordinated 3696 cm^{-1} band during the warm up of all ice mixtures. The 3696 cm^{-1} band area for 0% NH$_3$ drops linearly with temperature from 20 K to 120K and beyond whereas for 5% to 15% becomes negligible at ~ 120 K as does for 20% at ~ 85 K and below. This result clearly illustrates the powerful effect that minority species in the ASW ice matrix have on reducing the intensity of dOH.

In the next two sections we take these conclusions even farther and explicitly measure the pore surface area accessible to volatiles in the gas phase. We use the deposition of CO to explicitly calculate the pore surface area for pure ASW and ASW mixtures.

3.4.3 CO on pure ASW

We know that the dOH bonds are indicative of pore systems in the ASW ice (discussed in section 3.1) and that the intensity of the dOH spectral bands is diminished if the temperature of the ice is increased or minority species are present in the ASW matrix. We do not know, however, how best to relate reduction of dOH band intensity to pore surface area that is accessible to adsorption from species in the gas phase. To meet this need by using the infrared spectra of CO deposited on

ASW ice as a tool to map the accessible pore surface area as a function of CO ice thickness and temperature of the sample.

It is with this rationale in mind that we turn our attention to the next set of experiments, in which we use the infrared bands of CO to probe the pore surface area of ASW annealed at different temperatures. It is well-established that the infrared absorption feature of CO interacting with water ice is different from that of pure CO ice. The RAIRS of pure CO shows the longitudinal optical longitudinal mode (LO) at 2143 cm^{-1} while CO interacting with water shows two bands at $\sim$2140 cm^{-1} and $\sim$2152 cm^{-1}. According to our previous laboratory measurement of the diffusion of CO on the surface of p-ASW ([54]), diffusion of CO becomes significant at about 15 K. At 20 K, the diffusion is very efficient. If CO is deposited on top of ASW at 20 K, CO should diffuse into the pores and occupy the pore surface of the ASW. Once the whole surface area is covered by CO, and CO begins to build up as "pure" CO ice, the LO mode emerges. By examining the amount of CO deposited at which the LO peak emerges, the accessible surface area of p-ASW can be obtained. Furthermore, following this same analytical procedure but for ASW ice annealed at different temperatures we can reveal the temperature dependence of the pore system of ASW ice as compaction takes place. In the following, we first present a detailed analysis of the results of CO deposition on ASW annealed at 60 K and cooled to 20 K, and then show the results at other annealing temperatures.

Figure 28 shows the RAIR spectra of C-O stretching mode during deposition of CO on ASW annealed at 60 K and cooled to 20 K. At low CO deposition doses, there are two broad components centered at $\sim$2140cm^{-1} and 2152 cm^{-1}. When the CO dose is over $\sim$30 ML, the LO mode at 2143 cm^{-1} emerges, which we take as a sign of full coverage of the pore surface.

There have been several experimental studies of the interaction between CO and ASW surface [e.g. 68, 69]. Although It is generally accepted that the $\sim$2152 cm^{-1} component is due to the adsorption of CO on the dOH sites of ASW, there is no direct experimental evidence, as far as we know, that demonstrates the correlation between dOH bands and the 2152 cm^{-1} component. We used two Gaussian functions to fit the 2140 cm^{-1} and 2152 cm^{-1} components, and one Lorentzian function to fit the 2143 cm^{-1} component, and then we studied how these three components change with CO deposition dose. An example of fitting is shown in Figure 30. We apply similar fitting to all of the spectra in this experiment. The resulting band areas for the three components are shown in Figure31.

As was discussed in the section 3.1, introducing CO in ASW shifts the dOH bands. In Figure29, the dOH region of the RAIR spectra before and after the CO deposition is shown. Before CO deposition, the dOH band is at 3694–3696 cm^{-1} (the peak position varies between 3694 and 3696

cm^{-1}, depending on the annealing temperature; hereafter we refer to this peak as the 3696 cm^{-1} peak), while after CO deposition, the area of the 3696 cm^{-1} peak decreases to zero and the dOH induced by CO shows up at $\sim$3636 cm^{-1}. We used one Gaussian function to fit the 3696 cm^{-1} peak and one Gaussian function to fit the 3636 cm^{-1} peak, and obtained how the two peaks change with increasing CO deposition. The area of the 3696 cm^{-1} peak is shown in Figure 31, together with the peak areas of the three components of C-O stretching mode. Between 0 and 12 ML, the 3696 cm^{-1} band area decreases to zero. At the same time, the band area of 2152 cm^{-1} component increases from 0 to the saturation level. The anti-correlation between these two bands is evident. This is direct evidence that the 2152 cm^{-1} component is associated with CO binding to the dOH bonds. This evidence is not only experimentally novel in the field, but also justification for using CO a tool to investigate porosity in ASW; a species with a spectral feature we know is closely associated with dOH bonds.

Referring back to Figure 31 we see that at about 27 ML of CO deposition, the 2140 cm^{-1} band begins to saturate, while at the same time the 2143 cm^{-1} LO band emerges. This demonstrates that at about 27 ML of CO deposition, all the pore surface area is occupied, and pure CO starts to build up. This happens at a higher CO dose than the full covering of the dOH bonds, likely because CO molecules preferentially occupy the dOH sites over the non-dOH sites. In a prior study by Zubkov et al [70], it is reported that the full coverage of pore surface by nitrogen adsorption happens simultaneously with the saturation of the shifted dangling bond intensity. They suggested that N$_2$ does not preferentially bind to dangling OH groups. The difference between that work and this one is possibly due to the relative interaction energies of the two adsorbates. While nitrogen adsorption shifts the 3-coordinated dangling OH peak to 3668 cm^{-1}, CO adsorption shifts it by a larger amount, to 3635 cm^{-1} [54]. We take the CO dose at which 2143 cm^{-1} component just starts to show up, 27 ML in this case, to be the pore surface area of the 200 ML ASW ice annealed to 60 K. It is worth noting that the fact that the 3696 cm^{-1} band vanishes after CO deposition indicates that all of the pore surface area is accessible for CO adsorption, and the ASW ice does not contain closed non-accessible cavities inside the ASW ice. These cavities would have been detected by residual dOH bonds.

Similar CO depositions were carried out on 200 ML ASW samples that were annealed at 20, 40, 80, 100, 120, and 140 K, and cooled down to 20 K. RAIR spectra were recorded during CO depositions at 20 K and are shown in Figure 32. We determine the pore surface areas for the ASW annealed at different temperatures by visually examining the CO deposition dose at which the 2143 cm^{-1} component emerges. The ASW surface area versus annealing temperature is shown in Figure 33. The accessible pore surface area decreases linearly with annealing temperature almost up to

120 K, above which the surface area becomes about 2 ML. Considering that the surface of ASW is rough, it is likely that 2 ML covers the very top of the surface, (i.e. the ice-vacuum interface).

3.4.4   CO on ASW:NH$_3$ and ASW:CO$_2$

We now turn our attention to spectra of CO deposited on 220 ML 10 % ASW:NH$_3$ and 240 ML 20 % ASW:CO$_2$ samples that were annealed at 20, 40, 60, 80, 100, and 120 K, and cooled down to 20 K for deposition of CO. The same experimental and analytical procedure is followed as in the previous section regarding CO on pure ASW (section 3.4.3). Recall that the minority species NH$_3$ and CO$_2$ and the mixing ratios of 10 % and 20 % were utilized because they are representative of observations of ice coated dust grains in the ISM as discussed in section 3.1. We saw in Figure 27 and discussed in section 3.4.2 that the presence of NH$_3$ in the ASW matrix reduces the intensity of dOH spectral features and reduces the temperature at which they vanish. Now we are in a position to continue this intellectual thread by seeing if this translates to a mitigation of pore surface area and also determining if this trend translates to CO$_2$.

Figure 34 shows the spectra for CO interacting with water ($\sim$2140 cm^{-1} and $\sim$2152 cm^{-1}) during deposition on pure ASW (the same data as was shown in Figure 32) alongside that of 220 ML 10 % ASW:NH$_3$ and 240 ML 20 % ASW:CO$_2$ that are all annealed at different temperatures. Once again we use the coverage at which the CO LO mode at 2143 cm^{-1} emerges as indicative of the pore surface area. It can be deduced by visual inspection from Figure 34 that the presence of the minority species NH$_3$ or CO$_2$ does indeed reduce the accessible pore surface area. This point, however, is made abundantly clear in Figure 35 where particularly for CO$_2$ there is a marked decrease in accessible pore surface area relative to that of pure ASW.

This result paired with that of section 3.4.2 offers valuable insight in to the the confounding fact that dOH bonds have never been observed in the ISM but yet the porosity of ASW ice remains allusive. With these two results we have shown that the minority species NH$_3$ and CO$_2$ can disguise dOH bands by reducing their spectral signature significantly in effect blocking dOH sites and reducing the accesible pore surface.

3.4.5   Trapping of CO in ASW

In the previous section, we focused on the infrared spectra during CO depositions. Here in this section, we focus on the TPD stage of the same set of experiments. After the deposition of CO on ASW at 20 K, the ice was heated up from 20 K to 200 K at a ramp rate of 0.1 K/s while RAIR spectra were measured continuously. The band area of the C-O stretching mode was calculated for each spectrum during warming up (see Figure 36). For ices that are annealed at 60 K and above,

the C-O stretch band area becomes zero after the temperature goes past 60 K. This is in agreement with the study by Horimoto et al [71] who carried out similar experiments using methane instead of CO. In Figure 3.4.5, the desorption of CO from the ice can be separated into three regions. The first region is below about 55 K, which is the temperature at which CO on ASW surface (including the surface of pores) desorbs. The second region is from about 55 K to about 150 K, during which the CO band area drops linearly with temperature. These are the CO molecules that are trapped in the ASW matrix and released back into the gas phase gradually. Here we don't exclude the possibility that the band strength of CO buried inside bulk ASW can change with temperature. Indeed, experimental measurements by Schmitt et al [72] have found that the band strength of C-O stretching for CO buried in water ice has a reversible component that decreases almost linearly with the temperature between 50 K and 120 K. The irreversible component corresponds to the gradual releasing of CO from the bulk ASW. The third desorption happens when the ASW crystallizes, and all of the remaining CO molecules are forced out of the ice. This is sometimes referred to as the "molecular volcano" [47]. The amount of CO that is in the ice at about 60 K represents the CO that is trapped inside the ASW matrix, and we define it as the trapping amount. When the ASW is annealed to 60 K or above, the ASW does not trap any CO. The lower the annealing temperature, the higher the number of CO molecules that can be trapped. Based on this result one can also make the statement that the lower the annealing temperature the deeper and more complex the pore system of the ASW. This morphology temperature dependence probably results in some pores that are not directly connected to the vacuum-ice surface but are interconnected to those that are thus making the entire pore system accessible to CO as was confirmed in the last section.

Furthermore, the linear decrease of C-O stretching band area during heating is similar to that of CO_2 (see Figure 4 of He et al [73]). This suggests that the linearity may be a general phenomenon that occurs to all volatiles that are trapped in ASW. As was stated in the introduction section of this chapter there is a lack of knowledge pertaining to the structure of ASW in comets and how gas is released as a comet is exposed to solar irradiation. Perhaps this linearity, if explored further with other volatiles, may provide meaningful clues as to the elusive cometary relationship between trapping of volatiles and ice structures.

3.4.6 Dangling OH bonds during CO deposition

We now turn our attention to the dOH spectra during CO deposition on ASW. As the pore surface is gradually covered by CO, the dOH band at 3696 cm^{-1} decreases, and the band at 3636 cm^{-1} increases as is seen in Figure 29 . We applied the fitting scheme as discussed above to obtain the area of the dOH band during CO deposition. Figure 37 shows the area of the 3696 cm^{-1} dOH

band during CO deposited on ASW that has been annealed at different temperatures. For the ASW that was annealed at 140 K, the dOH band area is too small, and is not presented in the figure. The main finding from Figure 37 is that the dOH band area always drops to zero at high enough CO doses, regardless of the annealing temperature. This suggests that almost all the pore surface inside the ASW are accessible to CO, and the pores throughout the whole ice are interconnected as was also pointed out in the subsection 3.4.3. This conclusion also agrees with the previous results by Raut et al [58] which demonstrated that all of the pores are interconnected and are accessible to CH$_4$ adsorption.

3.4.7 Modeling of ASW Ice Porosity

Thus far in this chapter we have experimentally measured the accessible pore surface area for different annealing temperatures of ASW, ASW:CH$_4$, and ASW:CO$_2$ found a direct correlation between the CO and dOH spectral bands demonstrating that the CO molecules interact directly with the dOH bonds, measured the trapping amount of CO within an ASW pore system, and confirmed the accessibility of pore systems in ASW to CO. Now we direct our attention to theoretical simulations and modeling in order to clearly visualize the morphology of ASW ice and further justify these findings.

Figure 38 shows the structure of simulated water ice; the column-like structure becomes smoother with increasing temperatures, until eventually an entirely smooth structure is obtained at 140 to 150 K. In the model, the initial ice was deposited at 10 K and then heated to ∼150 K where the ice starts to desorb into the gas phase. The first two images of the model (at 10 and 70 K) have essentially the same structure. The model indicates there is little to no re-arrangement of the ice until the temperature of 60 K is reached. For the most part this is in agreement with the findings of the trapping section 3.4.5 seen in Figure 37 in which we observed that ASW ice does not trap CO molecules beyond an annealing temperature of 60 K thus demonstrating the marked difference between morphological evolution of ASW ice (i.e. re-arrangement) before and after 60 K. At 60 to 80 K, diffusion of water becomes efficient enough to play a role in the surface area and porosity, and increases at higher temperatures. The structure begins to smooth, by eliminating first the smaller pores until gradually all the pores are removed. Through this process, the ice reaches its maximum density at 150 K. It is important to note the model does not include the phase change from amorphous to crystalline ice, which would begin to occur at ∼140 K; this does not alter the results of the model as the main focus is between temperatures of 10 to 140 K.

In the laboratory results shown in Figure 33, we see that the accessible surface area decreases steadily up to 140 K. As stated in the earlier section regarding pure ASW 3.4.1, the 3-coordinate

dOH absorption band (3696 cm^{-1}) linearly decreases from 60 to 140 K (see Figure 25), likely corresponding to the beginning of significant pore collapse and thus the decrease in the surface area; this matches the decrease of the exposed surface in the model (Figure 39. The model shows in Figure 39 that the coverage begins to reduce between 60 K and 80 K and then steadily decreases after 80 K is reached. Until those temperatures are reached, very little rearrangement and pore collapse occur; this is probably due to the fact that the model uses isotropic potentials and thus is not sensitive to defects (OH dangling bonds) or orientational realignment of water molecules to which the experiment is sensitive. However, within the model we see a reasonable match at lower temperatures given that CO is a proxy for the extent of the accessible exposed H$_2$O network. It is worth noting that one of the limitations of the experiment is we do not have a data point corresponding to CO deposition on a ASW sample at 10 K (i.e. ice that has not been annealed at all) and it is fair to assume that if we had this result then the model would match the experimental results even better.

Figure 40 shows the modeling results of the ratio of the number of surface molecules to the total number of molecules during the deposition of 200 ML water onto a 10 K surface. In the first few monolayers, there is a large fraction of surface molecules. After the thickness reaches more than ∼10 ML, the fraction of surface molecules is no longer dependent on the thickness. This suggests that the structure of the ASW film is homogeneous and the conclusions in this work based on measurements of 200 ML ASW can be generalized to other thicknesses as well, as long as the ice is thicker than a threshold, in this study, ∼10 ML. This is more or less in agreement with previous studies by [55, 56, 74, 66].

Previously, Kimmel et al. 2001b.[74] used a kinetic model where a hit and stick method was used. Each individual molecule sticks to the surface being placed depending on the trajectory angle provided. This model does not include kinetic energy, but a parameter that designates how many times each incoming particle is allowed to hop before being permanently sticking. The images presented from Kimmel et al. show that the pores are also interconnected at the temperature of deposition, but does not include a linear warm-up of the ice. The model presented here is a kinetic model and hopping is set by the temperature, which in this case is essential as we linearly increase the temperature to replicate the experimental results. We show that the pores are interconnected and maintain this structure for high temperatures.

Unlike the experiments, within the model no rearrangement occurs below 60 K, because of the isotropic treatment used. Essentially, the model does not show the small-scale rearrangement due to orientational re-alignment of water molecules within their original potential. While the model cannot achieve these changes, it can provide a direct way to measure the surface coverage

of water ice. The surface area can be monitored during heating instead of requiring CO adsorption experiments where the water ice must be cooled down to 20 K to measure the amount of CO adsorbed on the ASW. Furthermore, the determination of surface area using CO adsorption as in the laboratory experiments may not be exactly the same as that from counting the number of water molecules on pore surfaces as in the modeling. A small difference between these two methods is possible.

Figure 41 shows the interconnectedness of the pores. A portion of ice was imaged to show the inner structure and not the total structure. Visually it shows that most pores are connected within the shown plane. As the ice is heated the pores collapse until eventually empty cavities within the water ice are left. The cavities appear to be the remnants of the initial column-like structure, which minimize their potentials by forming approximately spherical structures. The encapsulated pores are fairly small in size with widths around 2 to 3 nanometers. These cavities may allow entrapment of some volatile species such as CO until a later temperature. By 150 K all cavities have collapsed and the volatiles have either been desorbed or are trapped within a water matrix. These findings are in agreement with what was suggested by Bieler et al [46] but with regard to trapping of molecular oxygen in comets after molecular decomposition occurs as discussed in the introduction of this chapter.

3.5   Summary

In this study we measured the pore surface area of ASW that is annealed at different temperatures, and also quantified the temperature dependence of dOH band area during heating of ASW. We found a clear anticorrelation between the CO band $2152 cm^{-1}$ and the ASW dOH band $3696 cm^{-1}$ (see Figure 31) which revealed a remarkably clear and proportional relationship between dOH bonds and pore surface area. This finding warranted our moving forward with our study. We have shown in Figure 25 the 3-coordinated dOH absorption band ($3696 cm^{-1}$) decreases almost linearly between 60 and 140 K. This linear decrease with temperature can be compared with the linear decrease of pore surface area shown in Figure 33. Both seem to decrease linearly with temperature, although the curve in Figure 33 drops to the minimum at a slightly lower temperature than in Figure 25. This difference can be attributed to the fact that the ice represented in Figure 33 was annealed for thirty minutes and the ice represented in Figure25 was continuously heated. Our results are bolstered by computational modeling in which the pore surface area of ASW during heating was calculated by computing directly the total number of surface molecules (Figure 39). Taking in to account the fact that the model does not include orientational disorder it agrees with these experimental findings.

These proportional relationships are encouraging given it is well established in the field that the presence of dOH bonds is a key indicator that an ASW sample is porous. It is not so well established, however, whether or not this presence is a trustworthy tool with which to interpret porosity measurements such as accessible pore surface area. An example of such would be the work of Palumbo et al [50] in which they performed energetic ion bombardment on ASW and found that the decrease of pore surface area is four times less than the decrease in dOH absorption. From this experiment, one might conclude that the dOH band area is not proportional to the pore surface area. These results produce an unclear relationship between dOH band area and pore surface area for ASW as ion bombardment also induces chemistry that produces molecules such as O_2, O_3, H_2O_2, which may interact with the dOH bonds and shift or shield the dOH bands [54]. Furthermore, it shows that it is more appropriate to work with thermal processing of ASW; especially considering we are interested in simulating the conditions of highly shielded gas clouds in the ISM where the dominant mechanism by which energy is imparted to ice coated dust grains is through thermal processes.

The presence of cavities inside ASW has been reported or mentioned in several prior studies [75, 71, 76]. However, it is unclear whether these cavities are closed inside the bulk ASW or interconnected and accessible from the vacuum-ice interface. In Figure 3 of Raut et al [51] and Figure 8 of Cazaux et al [60], it was hinted that there are closed cavities, but there was no discussion about the connectivity of the cavities. In Figure 37, it is evident that after CO adsorption, the 3696 cm^{-1} band always drops to zero, regardless of the annealing temperature. This suggests that there is an insignificant number of closed cavities inside the bulk ASW, and almost all of the cavities (pores) are interconnected as well as connected to the vacuum-ice interface. This result is verified by the modeling by which the morphology is imaged in three and two dimensions (Figure 38 and Figure 41) demonstrating the interconnectedness of the pore system. This is also in agreement with the experimental results of Raut et al [58], who found that the number of closed pores is insignificant in a 1000 ML ASW. Furthermore, the threshold thickness is also computationally modeled and shows that for ASW ice of thicknesses greater than 10 ML the experimental work seen in this chapter with regard to porosity can be generalized for deposition for other volatiles (Figure 40). This is important as the experimental interconnectivity result (Figure 37) is in agreeance with the work of Raut et al [58] who demonstrated interconnectivity of ASW using a deposition volatile of CH_4.

With regard to astrophysical implications the fact that all pores are connected all the way to the vacuum–ice interface suggests the possibility that volatile molecules that are formed on the pore surface can diffuse and desorb from the ice before the desorption of water. The desorption

of molecules before water desorption has the potential to explain the observations which found complex organic molecules in regions with high-extinction [77, 49] and regions outside the water snow line in protoplanetary disks [45] and the low abundance of molecular oxygen detected from comet67P/ Churyumov–Gerasimenko [46]. Findings from this study:

- Experimental results show that the total pore surface area in 200 ML of ASW at 20 K is equivalent to 46ML, and decreases linearly with annealing temperature to ∼120 K.

- Almost all pores are connected to the vacuum–ice interface and accessible for volatiles adsorption.

- The 3720 cm^{-1} dOH band, which is due to 2-coordinated water molecules, disappears when the ASW is heated to 60 K.

- The 3720 cm^{-1} dOH band disappears if a 5% or greater minority species of NH_3 is present in the ASW matrix.

- The 3696 cm^{-1} dOH band, which is due to the 3-coordinated water molecules, is reduced in intensity if a minority species of NH_3 is present in the ASW matrix.

- The 3696 cm^{-1} dOH band decreases more or less linearly between ∼50 K and 140 K.

- The temperature at which the 3696 cm^{-1} dOH band vanishes reduces with increasing presence of the minority species NH_3.

- The accessible pore surface area decreases with increasing minority species of NH_3 or CO_2 present in the ASW matrix.

- The accessible pore surface area is reduced with the lessening in intensity of the 3696 cm^{-1} dOH band.

- The 2152 cm^{-1} absorption peak observed for CO on ASW is due to the interaction of CO with dOH bonds on pore surfaces.

- ASW annealed to 60 K or above loses the capability to trap CO molecules from the gas phase.

- After the first ∼10 ML, the fraction of surface molecules to the total number water molecules does not change with thickness.
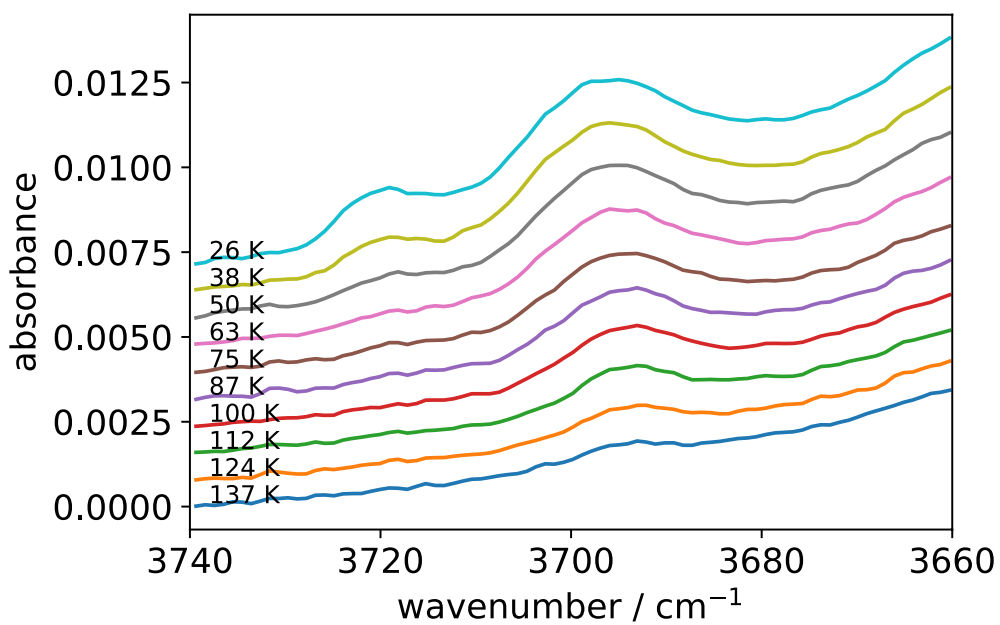
Figure 22: RAIR spectra of 200 ML water ice during heating at various temperatures. The water ice is deposited from the background when the surface is at 10 K. The heating ramp rate is 3 K/minute. Spectra are offset for clarity.[9]
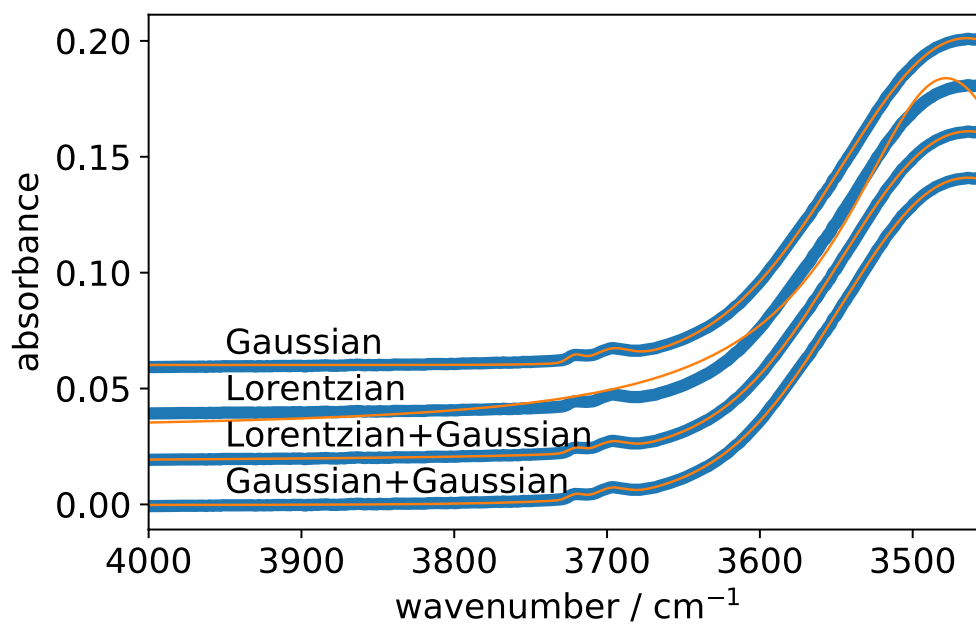
Figure 23: Example of fitting of the RAIR spectrum of bulk water OH stretching mode absorption using different fitting schemes. The small features of the dangling OH (dOH) bonds located at $\sim$3696 cm^{-1} and $\sim$3720 cm^{-1} are each fitted with a Gaussian function. The left side of the main peak is fit using the four schemes labeled in the figure. [9]
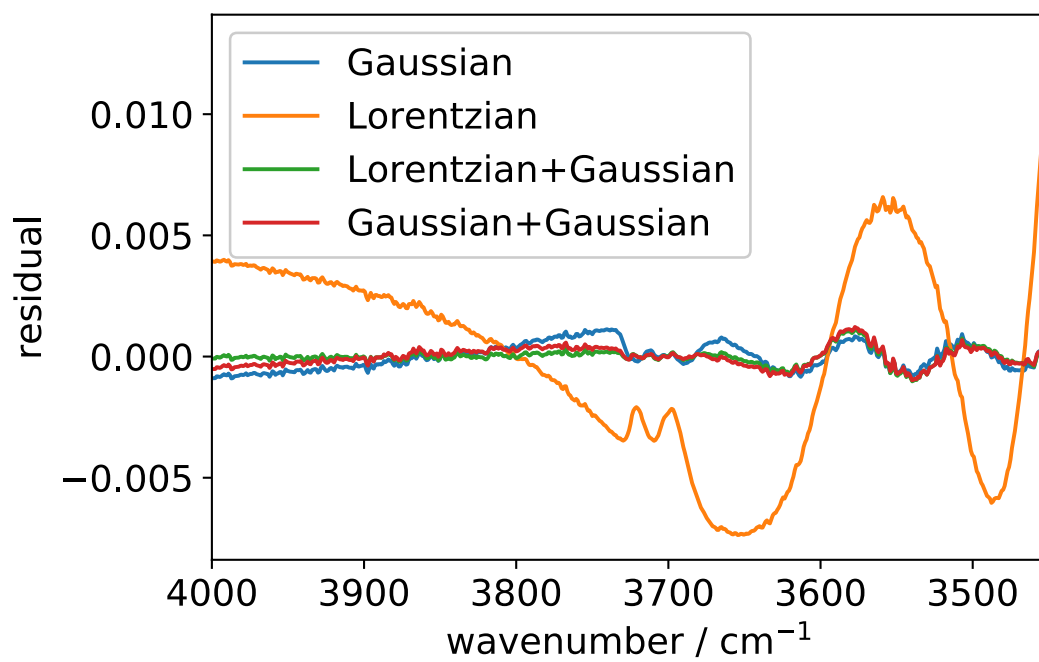
Figure 24: Residual of the fittings in Figure23. [9]
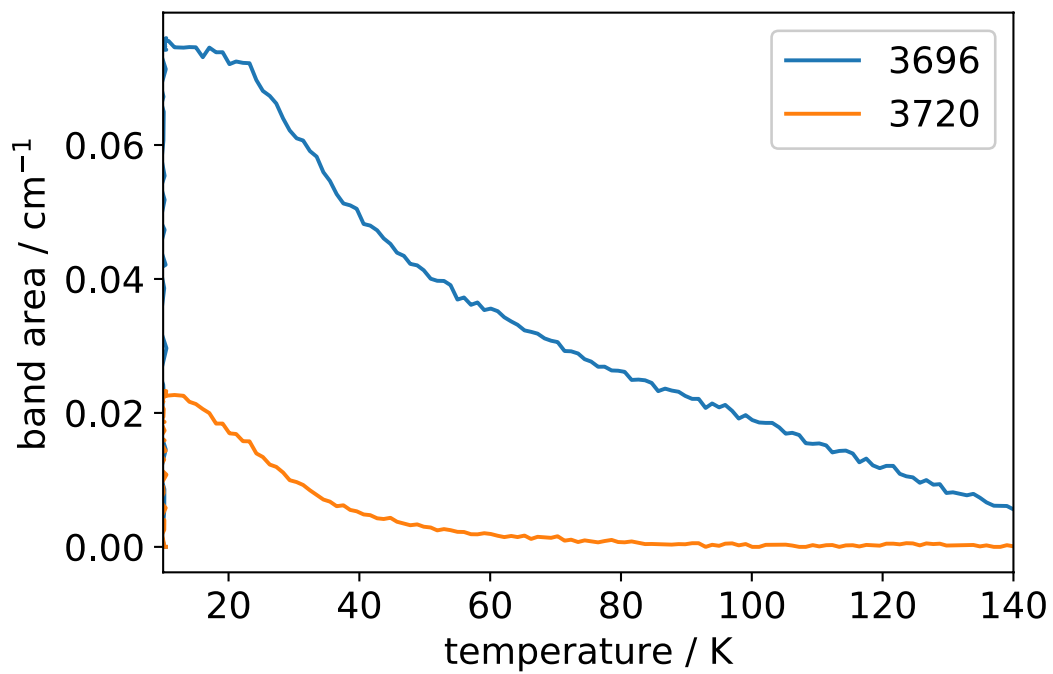
Figure 25: The area of the two dOH absorption bands during warming up of a 200 ML water ice grown at 10 K and heated at 3 K/minute. [9]
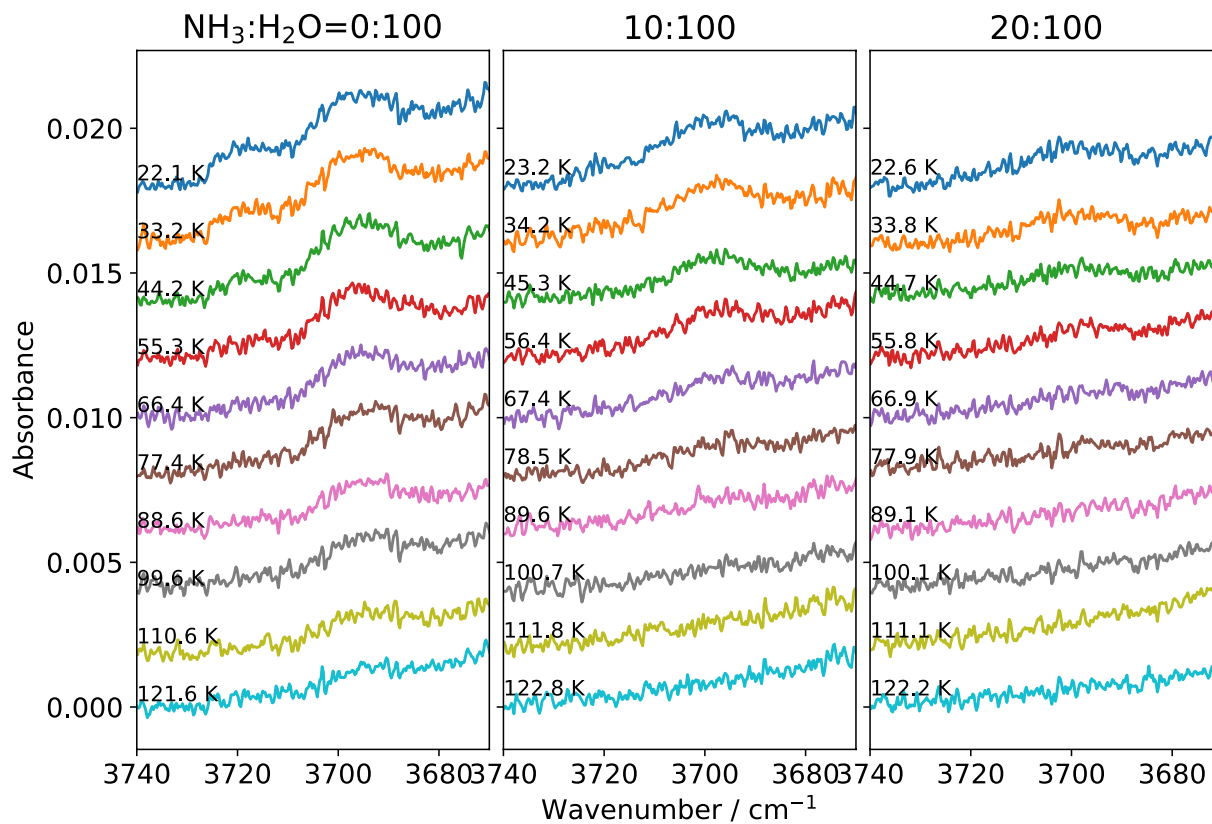
Figure 26: RAIR spectra of 200 ML water ice and 200 ML water ice with minority species NH_3 present during heating at various temperatures. The water ice is deposited from the background when the surface is at 10 K. The heating ramp rate is 3 K/minute. Spectra are offset for clarity. [9]
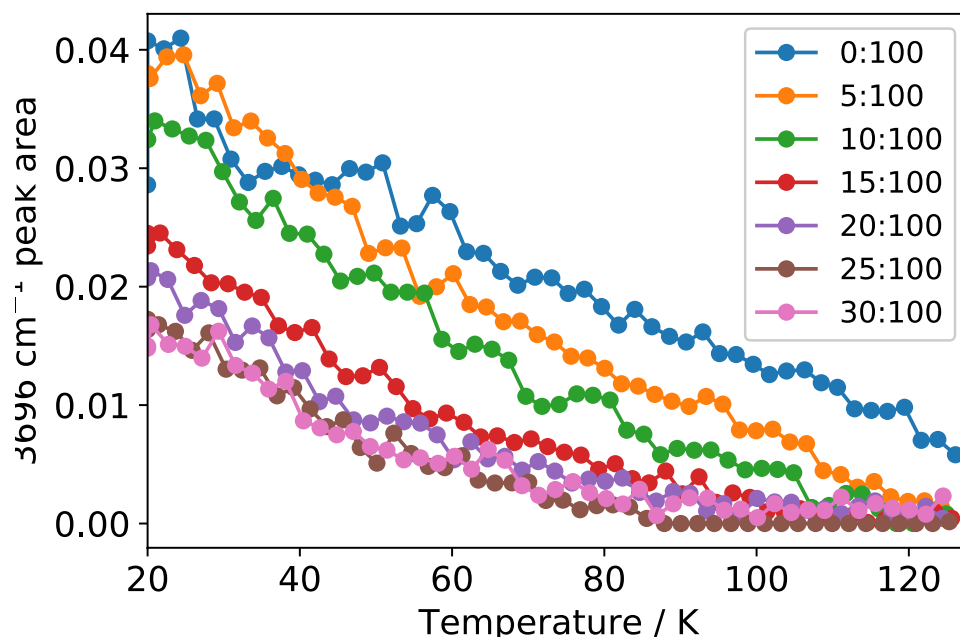
Figure 27: The area of the three-coordinated dOH absorption band during warming up of a 200 ML water ice with different percentages of minority species NH_3 present; grown at 10 K and heated at 3 K/minute. [9]
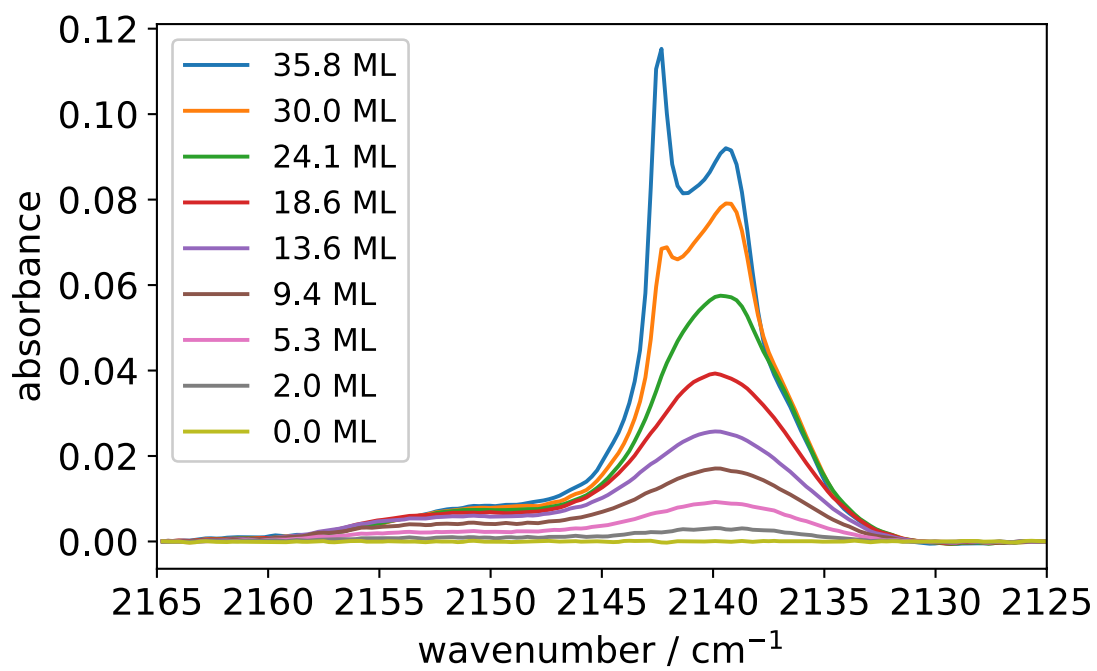
Figure 28: The RAIR spectra of CO deposited on top of 200 ML ASW that is annealed at 60 K for 30 minutes and cooled down to 20 K. The CO dose for each spectrum is shown in the inset. [9]
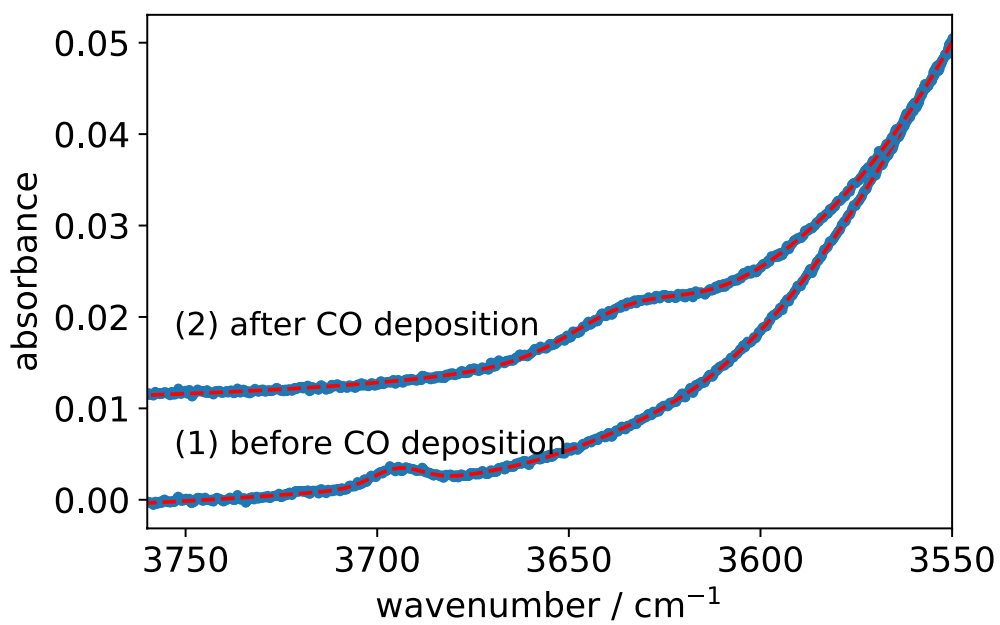
Figure 29: The dOH region of the RAIR spectra of 200 ML water ice annealed at 60 K and cooled down to 20 K (1) ; and after 21 ML of CO deposition (2). Dashed lines are the fitting. Spectra are offset for clarity.[9]
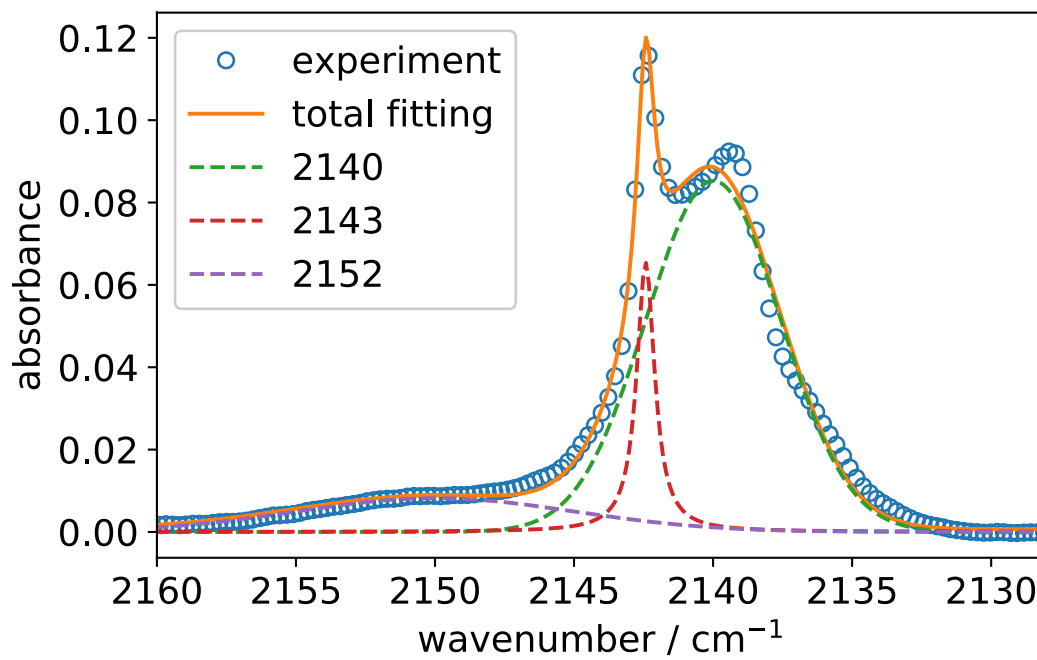
Figure 30: An example fitting of the spectra in Figure 28 using two Gaussian functions and one Lorentzian function. [9]
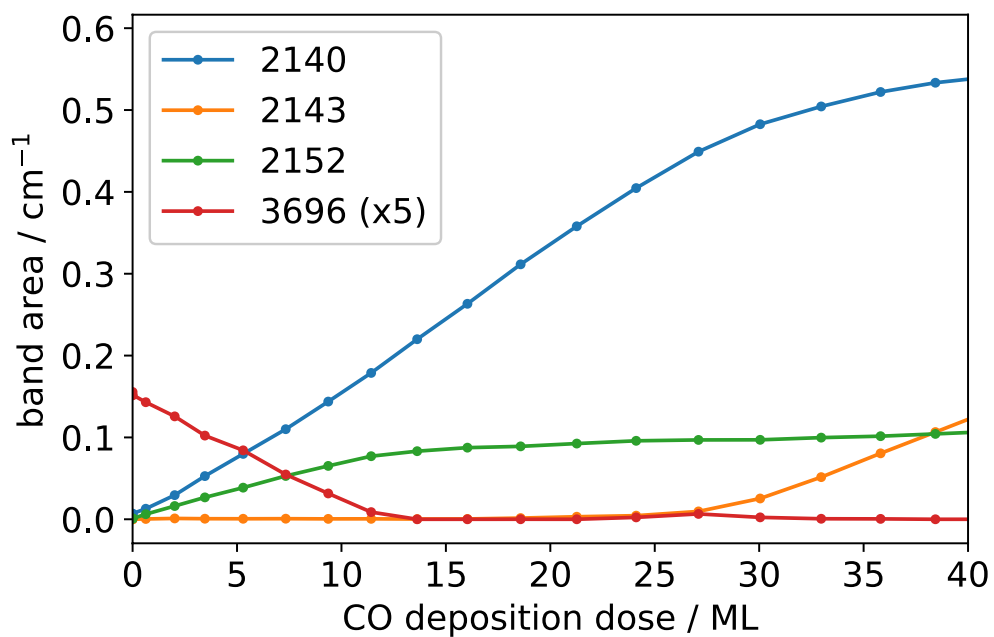
Figure 31: The band area of the three components of the CO absorption profile and the dOH band at 3696 cm^{-1} during CO deposition on 200 ML ASW annealed to 60 K. Fittings are done as shown in Figure30 [9]
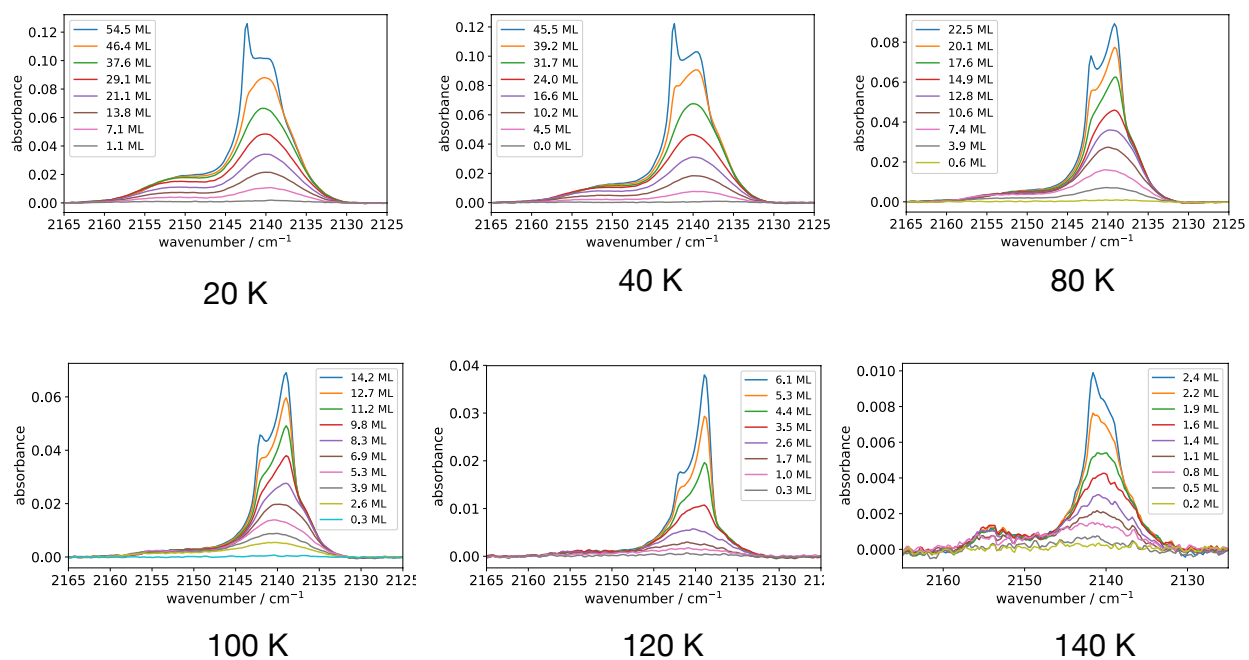
Figure 32: The RAIR spectra of CO deposited on top of 200 ML ASW that is annealed at 20, 40, 80, 100, 120, and 140 K, and cooled down to 20 K. The CO dose for each spectrum is shown in the inset.

[9]
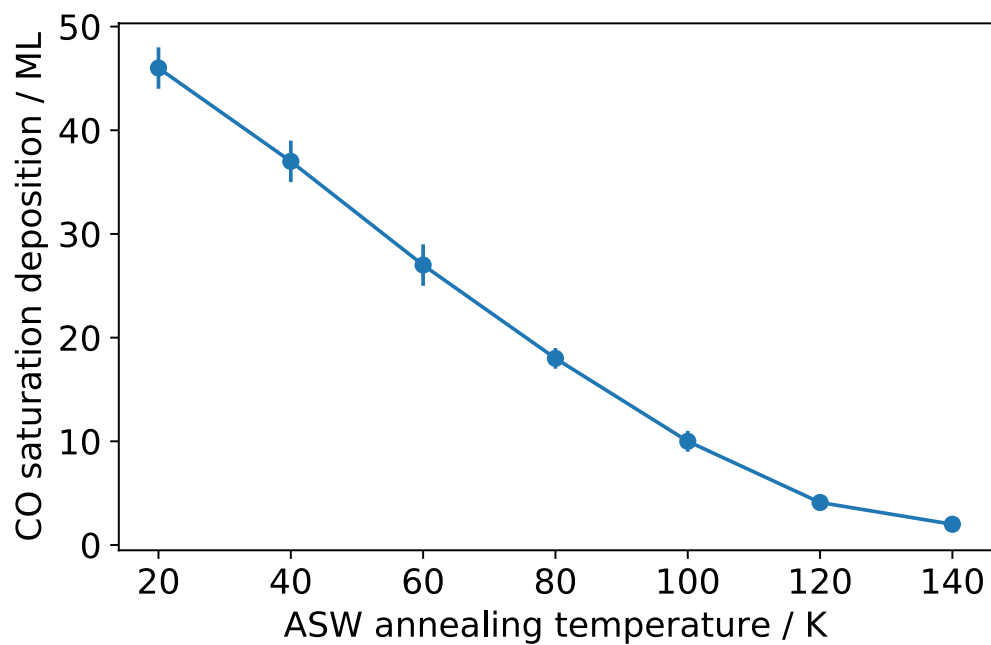
Figure 33: Accessible pore surface area in 200 ML of ASW that are annealed at different annealing temperatures. The pore surface area is measured by the amount of CO that fully covers the pore surface.

[9]
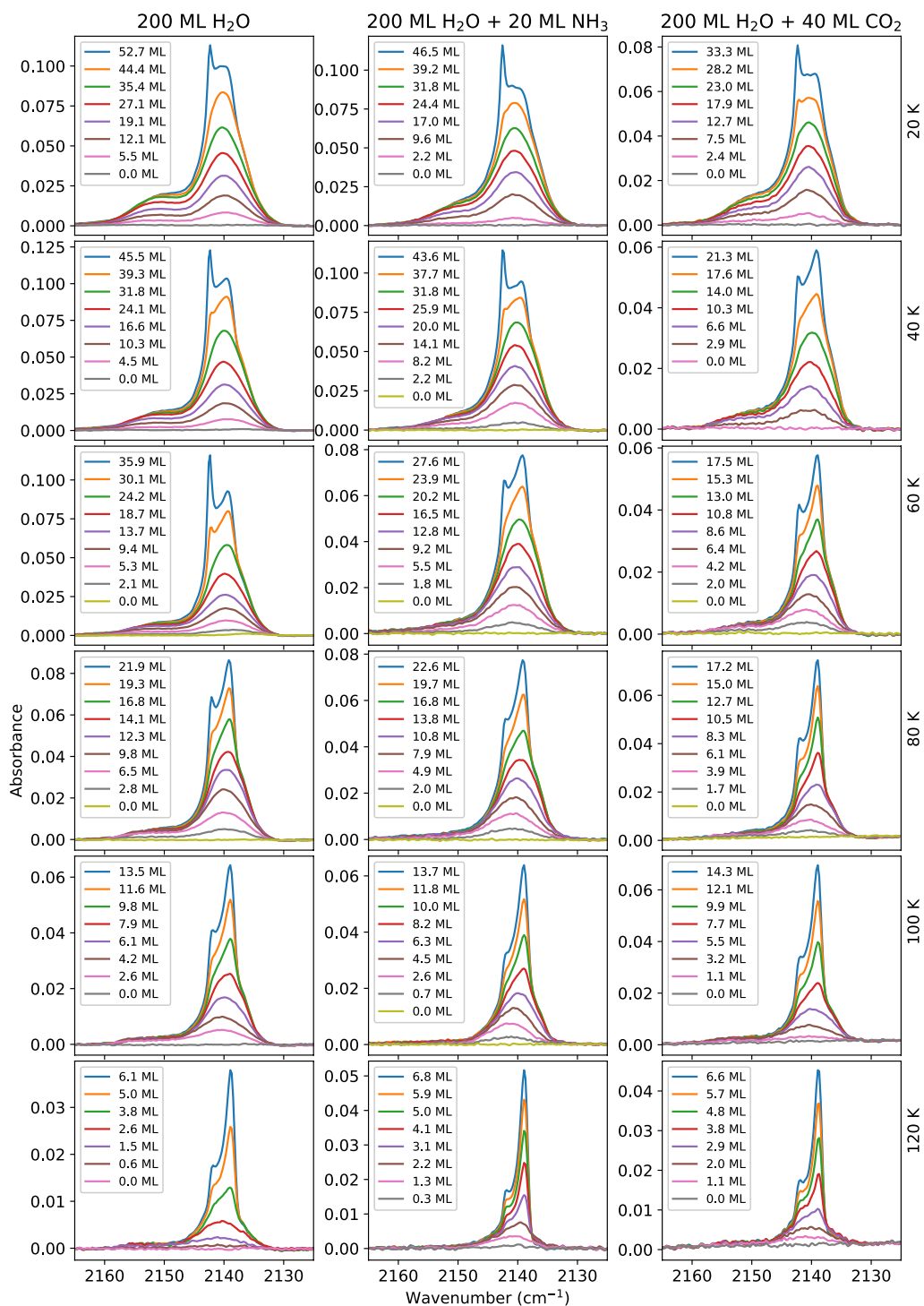
Figure 34: The RAIR spectra of CO deposited on top of 200 ML ASW, 220 ML 10 % ASW:NH$_3$ and 240 ML 20 % ASW:CO$_2$ that are annealed at different temperatures and cooled to 20 K for CO deposition. The CO dose for each spectrum is shown in the inset. [9]
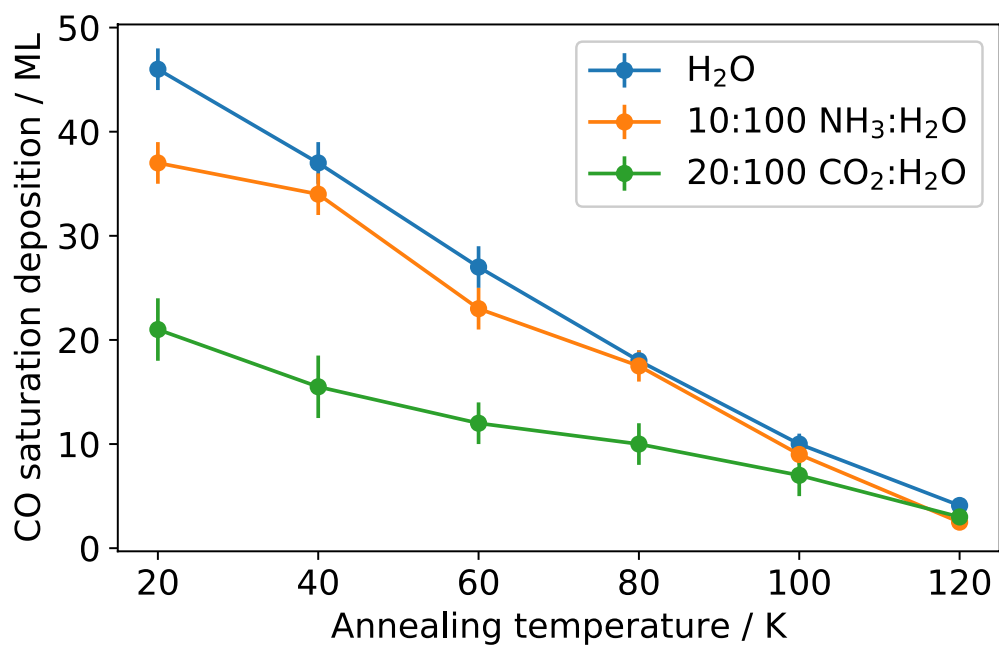
Figure 35: Accessible pore surface area in 200 ML ASW, 220 ML 10 % ASW:NH_3 and 240 ML 20 % ASW:CO_2 that are annealed at different temperatures. The pore surface area is measured by the amount of CO that fully covers the pore surface. [9]
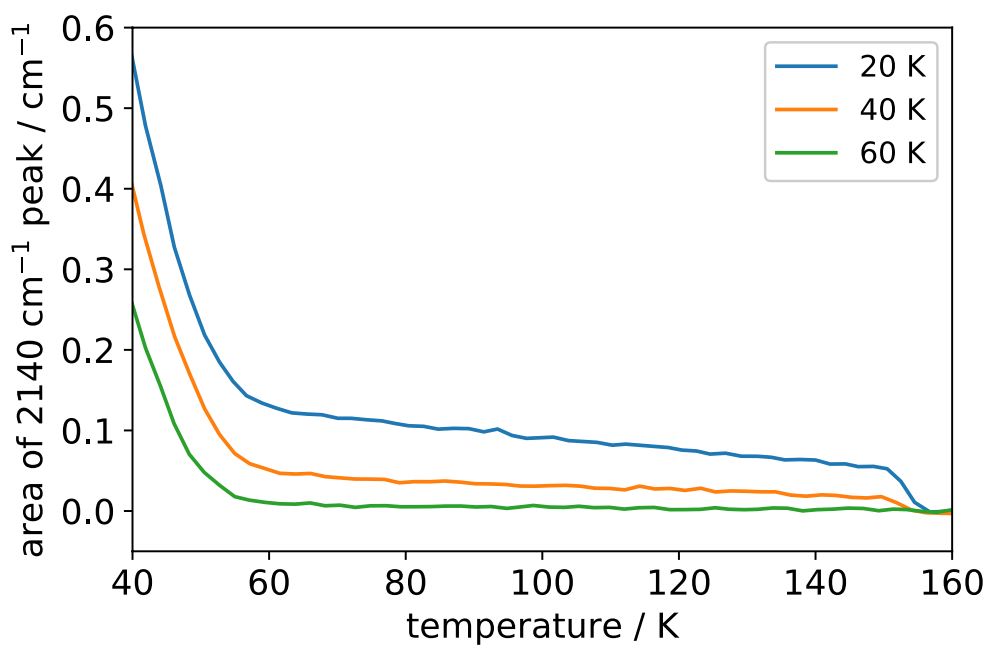
Figure 36: Band area of the 2140 cm^{-1} peak during warming up of (1) CO adsorbed on ASW that is annealed at 20 K; (2) CO adsorbed on ASW that is annealed at 40 K and cooled down to 20 K; (3) CO adsorbed on ASW that is annealed at 60 K and cooled down to 20 K. Band area for all curves are 21 ML for CO and 200 ML for ASW. [9]
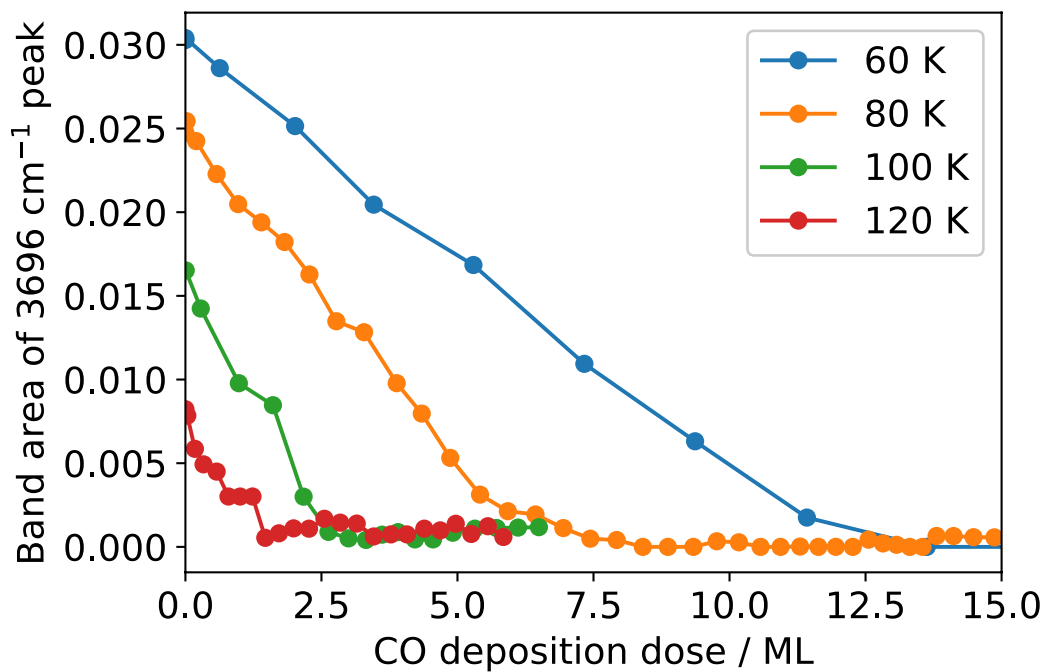
Figure 37: Band area of the dOH bond absorption at 3696 cm^{-1} after deposition of CO at 20 K on 200 ML ASW that has been annealed at 60, 80, 100, and 120 K. [9]
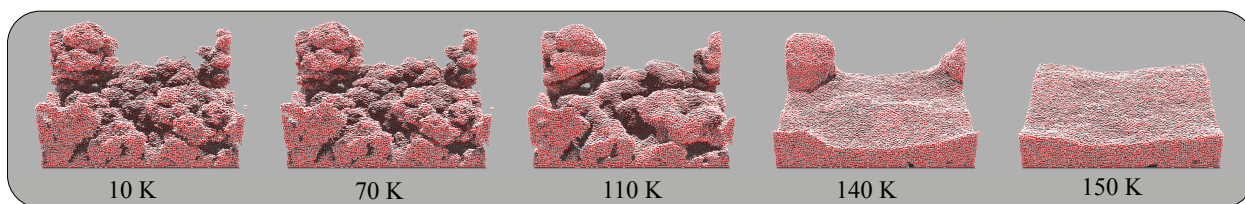
Figure 38: 25 ML amorphous water deposited and heated at 3 K min^{-1} to 160 K. Simulations were done by Robin Garrod and his student Aspen Clements of the University of Virginia in a joint collaboration. [9]
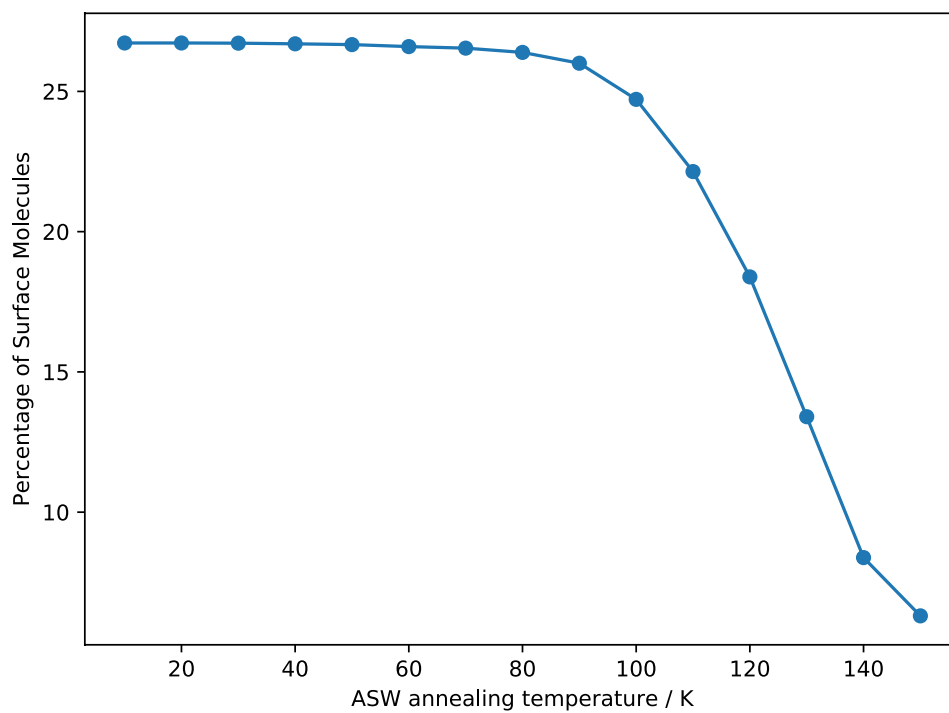
Figure 39: Accessible pore surface area in the model of ASW as it is heated at 1 K min^{-1}. The pore surface area is measured by the percentage of surface to total water molecules. The error bars are calculated by using both 25 and 200 ML model coverages, and are essentially insignificant. Simulations were done by Robin Garrod and his student Aspen Clements of the University of Virginia in a joint collaboration. [9]
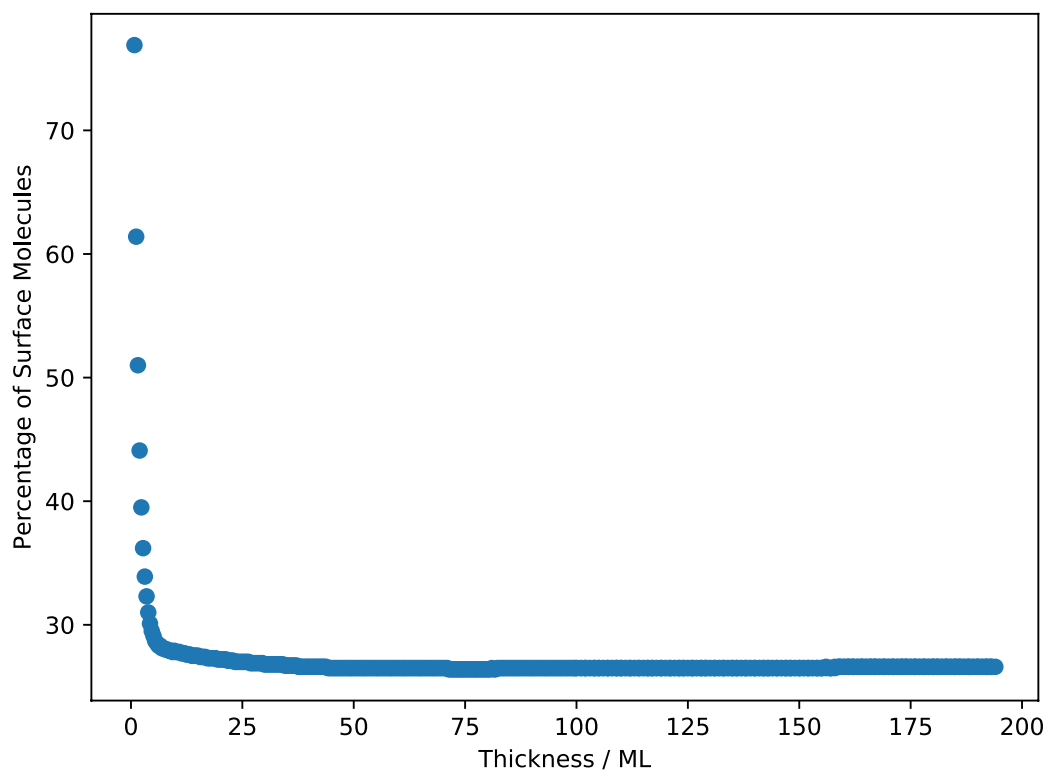
Figure 40: Ratio of the number of surface water molecules to the total number of water molecules obtained in modeling during deposition of 200 ML water at 10 K. Simulations were done by Robin Garrod and his student Aspen Clements of the University of Virginia in a joint collaboration. [9]
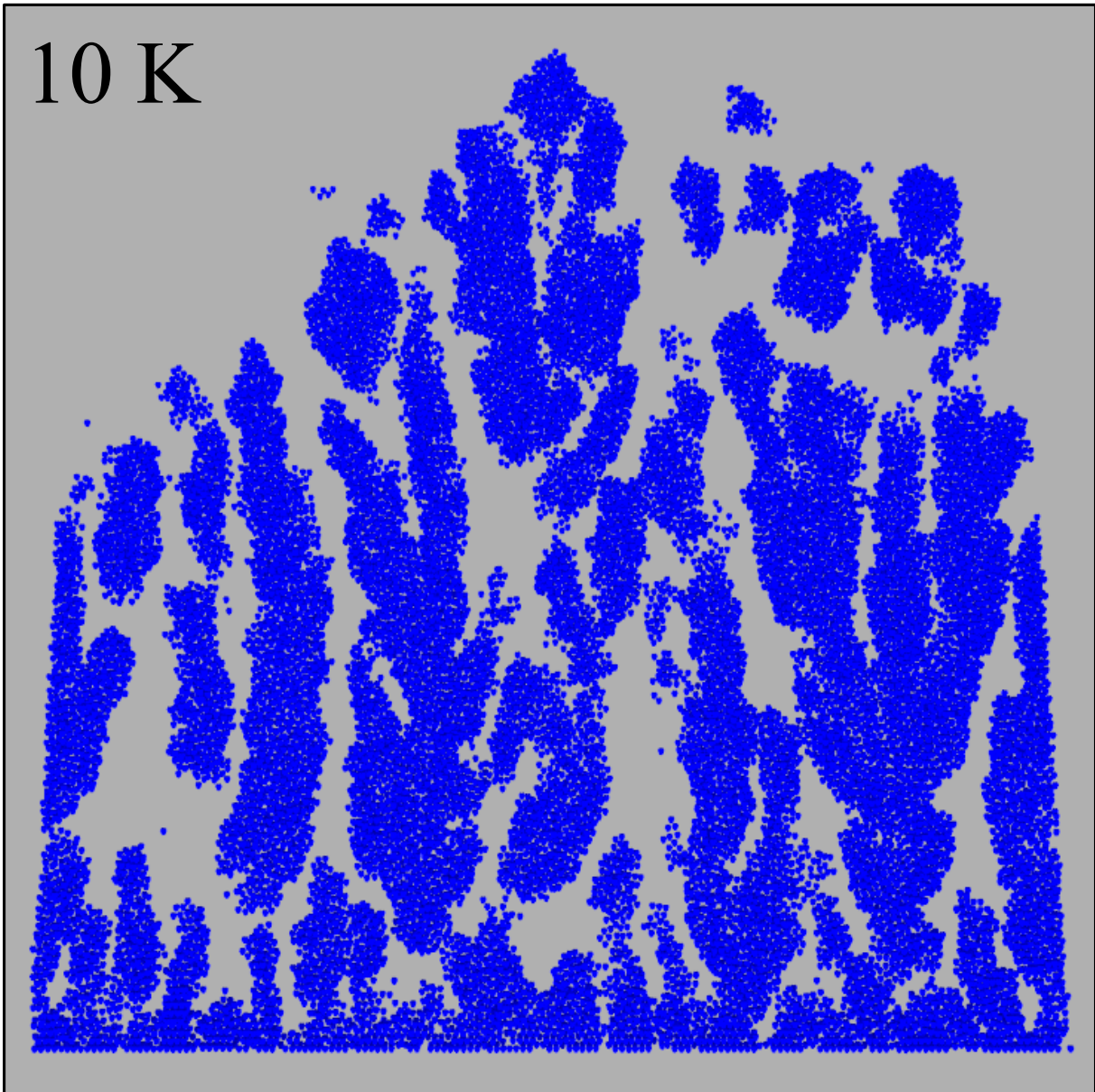
Figure 41: A slice of a 200 ML thick amorphous water deposited at 10 K imaged with POV–Ray. The thicker ice was used to demonstrate the interconnectedness as it was more obvious than in the much thinner ice of 25 ML. Simulations were done by Robin Garrod and his student Aspen Clements of the University of Virginia in a joint collaboration. [9]

Chapter 4

Phase Transition of Interstellar CO Ice

4.1 Introduction

In the last chapter, we used the spectral features of the adsorption of CO on and in ASW and ASW mixtures as a tool with which to measure the available pore surface area and draw a connection between this parameter and dOH spectral features. This allowed us a useful analytical perspective from which to discuss predictive insights into the astrophysical phenomena of trapping of gas species in comets and potential mechanisms of COM formation on and in the water-rich (i.e. CO-poor) layer of interstellar ice mantles. In this chapter we direct our attention to the transition of CO itself from a disordered state to one that is more ordered as a potential diffusive mechanism by which COM formation occurs on and in the water-poor (i.e. CO-rich) outer layer of interstellar ice mantles (see chapter one for a detailed discussion on interstellar ice composition and geometry).

One of the primary motivations of this study is that laboratory experiments and astrophysical models all suggest that many COMs are formed in the CO-rich layer yet little is known about its morphology [78] [79]. In fact, interstellar CO-rich ice morphology has never been the main focus of a prior study. In 2017 Chuang et al performed laboratory experiments in which they showed that several COMs (most notably: methyl formate (MF), ethylene gycol (EG), glycolalhyde (GA)) form in CO-rich ice following hydrogenation and UV irradiation at 13 K [78]. A year prior to this Chuang demonstrated the feasibility of COMs formation without the aid of energetic particles/radiation in the identification of two-carbon COMs in a laboratory experiment of H atom addition to CO ice at 10 K [80]. Simons et al built a CO hydrogenation network model using quantum chemical calculations for rate constants in combination with microscopic Monte Carlo for positional information of molecules. They used CO hydrogenation experiments to bench mark their model and were able to simulate, in agreement with observed COM ratios, that MF, GA, and EG

are formed under all interstellar conditions, even at extremely low temperatures such as 8 K [79].

As discussed in chapter 1 the driving mechanism by which the phenomenon of molecular formation is thought to occur on interstellar ice mantles is diffusion [5]. The question, however, as to how diffusion of molecules becomes energetically favorable at extremely low dense cloud core temperatures of 10-15 K remains an unsolved fundamental problem of molecular astrophysics as at this temperature range the probability of overcoming a typical activation energy barrier is exceedingly small[81]. COM formation in the solid-state phase of cold dense cloud cores vs that of the gas-phase of hot cores makes for a useful debate in illuminating this issue. The standard model of hot core complex chemistry is generally described as icy mantles of cold cloud cores being rapidly warmed by a nearby protostar. Consequentially they are injected back into the gas phase in which COM formation is stimulated [81] [82]. Motivated by failings of this model to predict the production of complex molecules from precursor methanol [83] Garrod et al used a gas-grain network of reaction modeling to investigate the formation of methyl formate, dimethyl ether, formic acid, formaldehyde and methanol during protostellar warm-up and evaporative phase [81]. They found, in agreement with observation, a strong coupling between gas-phase and grain surface reactions. Implicit in their findings is that the observed COMs in hot cores may have very recently evaporated giving meaningful credit to the theory of COM formation on and in interstellar ice as opposed to taking place only in the gas phase [81]; in effect calling back in to question the pivotal and elusive role of a diffusive mechanism and the lack thereof a satisfactory explanation.

The morphology of water ice has been studied extensively both experimentally and theoretically [84, 85, 86]. As is known from the prior studies, the phase transition of water ice is typically accompanied by the segregation and possible desorption of the minority species. Trapped gases in amorphous water ice are released through cracks that develop in the crystallization process. The eruption of volatiles during the crystallization is known as a molecular volcano [47]. Molecules more volatile than water ice desorb during the molecular volcano, but less volatile molecules remain in a segregated form and desorb at higher temperatures. We decided to see whether a similar transition happens in CO ice, what is the temperature of the transition, and whether minority species segregate into clusters during the transition. If the minority species happen to be reactive, chemical reactions between them could form COMs. To verify it, laboratory experiments were performed under dense cloud relevant conditions to study the crystallization of CO ice, with and without minority species, on an amorphous solid water ice film that emulates the inner layers of the ice mantle. The results are shared and discussed in this chapter.

As stated earlier there is a significant lack of interstellar CO ice morphology studies. There are some prior works of interest, however, but many of them do not take into account astrophysically

relevant temperature ranges and thicknesses for the CO-rich ice layer which are 10-15 K and approximately 0.01 μm or 3 ML respectively [11, 21] [87]. An example of such a study would be that of Mizuno et al who performed X-Ray Diffraction measurements on 6μm of CO deposited on to a 3×3 cm^2 silicon substrate at 3 K. The purpose of their study was to investigate structural properties of molecular glass. They performed annealing experiments from which they were able to make a convincing argument for the existence of an amorphous CO phase [88]. The extremely low temperature, even for interstellar standards, at which Mizuno et al. observes this groundbreaking morphological property demonstrates the challenging nature of studying CO ice morphology. This elusive quality can be seen in the work of Kang et al. who applied strong external electric fields across CO crystal films of thicknesses 0.0081, 0.0224, and 0.024 μm deposited at 10 K and studied the vibrational stark effect and dipolar inversion in CO crystals via infrared spectroscopy (RAIRS). While their experimental method and analysis regarding the head-to tail inversion of CO dipoles is sensible and quite interesting their conclusions regarding the CO ice temperatures that constitute crystalline and amorphous structure are misguided. They claim that CO ice is amorphous when deposited on to ASW at 10 K and it is crystalline when either deposited at or heated up to 20 K [89]. However, we have measured a marked structural change in CO ice on ASW in a temperature range that is lower than 10 K. We find that what Kang et al considers to be "amorphous" is in actuality more ordered and is referred to as polycrystalline in our work . It is evident that what they deem to be amorphous is in actuality a state that is more ordered. This point is revisited and discussed in greater detail in the results section of this chapter. It is important to note that the morphology of thin CO ice was not the main focus of this group's study. Furthermore, despite the astrophysically relevant temperature and thickness ranges utilized by this group there was no motivation to draw astrophysical relevance from the data. This study, however, demonstrates clearly how subtle and easily an amorphous CO ice phase disguises itself.

Astrophysical studies involving CO ice often don't focus on CO itself but instead other species. Simon et al. measured the entrapment of CO molecules on CO_2 ice by depositing 7-53 ML of 1:1 and 9:1 CO_2:CO mixtures at 17 K. This work was done with the astrophysical motivation of exploring whether or not CO_2 as a common cometary component is able to trap CO in the same manner for which water ice is known. Essentially, they use CO ice not as a main subject of study but as a probe with which to characterize CO_2 ice [90]. Inversely, in the work of this thesis we use CO_2 as a probe with which to characterize CO ice through the use of CO:CO_2 9:1 mixtures as is discussed in detail in the results section of this chapter. In fact, we consulted the work of Simon et al in designing our gas mixing manifold and determination of appropriate mixing times (this is discussed in more detail in the experimental procedure section of this chapter).

4.2   Experimental Procedure

A detailed description of the apparatus is given in Chapter 2 of this thesis as well as in prior published works [91, 92], and here only the main features that are relevant to this study are summarized. In all experiments, 30 ML of compact water ice was grown by introducing water vapor into the UHV chamber through a stepper motor controlled UHV precision leak valve when the sample is cooled to 10 K. The details of the water vapor deposition procedure are identical to those discussed in the experimental procedure section of chapter 3. During water vapor deposition, the temperature of the sample was kept at 10 K. After the water deposition was completed, the sample was then heated to 130 K and annealed for at least an hour to ensure that it was compact ASW.

Two types of experiments were done, one in which a CO ice was grown on compact (non-porous) ASW, and another in which a vapor mixture of CO and CO_2 was grown on compact ASW. For the types of measurements we planned, it was important to make ice thin films reliably and with the desired thickness. The following procedures were implemented.

In one set of experiments 9 ML of pure CO ice were grown on compact water ice at 6 K and then heated at 12 K/min to various temperatures at which experiments of ordering kinetics were performed. In another set of experiments different thicknesses of pure CO ices were grown on the compact water surface at 6 K and then slowly heated to 20 K at 0.2 K/min. (We also performed a slow heat-up experiment of 10 ML of a 9:1 $CO:CO_2$, see next paragraph for details). The procedure for depositing CO comprised: 1. Pumping down the gas manifold with an external pumping station until the manifold reached a pressure of approximately 2 mTorr; 2. Isolating the pumping station from the manifold; 3. Introducing ~ 20 PSI of laboratory grade CO gas to the manifold; 4. Opening the leak valve via Labview program and stepper motor and beginning deposition (the program will automatically close the leak valve once target thickness is reached). After deposition was complete the manifold was pumped down with the external pumping station. The ice was characterized by IR spectroscopy using a FTIR spectrometer in the RAIRS configuration (see Chapter 2 for more details).

In another set of experiments 10 ML of $CO:CO_2$ 9:1 mixtures were grown in the same fashion on compact water ice at 6 K and then heated to various temperatures at 12 K/min at which isothermal experiments were performed. $CO:CO_2$ 9:1 mixtures were made inside a 500 ml canister that is connected to a stainless steel VCR sealed gas manifold. CO and its minority CO_2 were introduced consecutively into the manifold and canister through a specially constructed mixing manifold that is discussed and shown in Chapter 2. The ratios were determined by measuring the pressure in the gas manifold with a heated MKS Baratron high accuracy absolute capacitance manometer. We determined that at least one hour was required for sufficient mixing. This mixing time was also

found to be most effective for Simon et al. in their studies of CO2:CO mixtures [90].The procedure for preparing and depositing the mixture was: 1. Pumping down the gas manifold and mixing manifold with two separate external pumping stations until both manifolds reached a pressure of approximately 2 mTorr; 2. Isolating the pumping stations from their respective manifolds; 3. Introducing $\sim$ 20 PSI of 99.99 percent purity research grade CO gas into the mixing manifold; 4. Opening the mixing manifold to the gas manifold and introducing the CO gas in to the gas manifold until 90 mTorr was measured; 5. Isolating the mixing manifold from the gas manifold; 6. Pumping down the mixing manifold with the external pumping station until a pressure of 2 mTorr was reached; 7. Isolating the pumping station from the mixing manifold; 8. Introducing $\sim$ 20 PSI of laboratory grade CO_2 gas in to the mixing manifold; 9. Opening the mixing manifold to the gas manifold and introducing the CO gas in to the gas manifold until 100 mTorr was measured; isolating the mixing manifold from the gas manifold; 10. Isolating the canister from the gas manifold; 11. Pumping down both manifolds with their respective pumping stations until a pressure of 2 mTorr was reached; 12. Waiting at least one hour for the gas to thoroughly mix ; 13. Isolating the pumping stations from their respective manifolds; 14. Opening the canister introducing the mixture in to the gas manifold; 15. Opening the leak valve via a LabVIEW program and stepper motor and beginning deposition (the program automatically closes the leak valve once target thickness is reached). After deposition was complete the gas manifold was pumped down with the external pumping station.

The UHV base pressure prior to deposition was $\sim$ 4 X 10^{-10} Torr, the pressure during deposition was $\sim$ 4 X 10^{-7} Torr, and the typical duration of deposition was $\sim$ 2 minutes.

4.3 Results and Analysis

4.3.1 Experiments of Kinetics of Pure CO

We begin by examining the CO infrared spectral features of 9 ML of pure CO deposited on 30 ML of compact ASW at 6 K and then heated at a fast 12 K/min rate in five separate experiments to 8.0, 8.2, 8.3, 8.4, and 8.6 Kelvin. In these experiments the time evolution of key IR bands is measured in order to obtain information about the kinetics of structural transformation and diffusion. Figure 42 shows the 8.6 K isothermal experiment and as it can be seen CO has two primary components; a sharp peak at 2143 cm^{-1} fitted by a Lorentzian function and a broader peak lesser in amplitude at 2140 cm^{-1} fitted by a Gaussian function. With time, the 2143 cm^{-1} sharpens and increases in amplitude slightly while the 2140 cm^{-1} feature decreases in amplitude. You will notice a slight overshooting of the fitting of the 2143 cm^{-1} peak. This is due to the limitations of the spectral

resolution of the detector which during all experiments discussed in this chapter was set at its most optimal value of $\Delta\lambda = 1$ cm^{-1}. You will also notice a slightly less than ideal fit of the initial t=0 seconds 2140 cm^{-1} peak. The band profile of amorphous CO is notoriously difficult to fit and many methods including using multiple curves were used to get a better fit but this arrangement of just a single Lorentzian and single Gaussian gave us the best and most clearly interpreted fit of the data. Furthermore, notice that once the spectral features begin to evolve with time, the Gaussian fit quickly improves and fits the data quite well. In the discussion in chapter 3, the reasoning as to the use of Lorentzian and Gaussian functions to fit IR spectral features is that Gaussian functions are indicative of disordered solid states. In these states ices experience a more diverse environment with more diverse vibrational energy states and thus a softer and broader spectral peak [65]. Thus, it is likely that this initial slightly ill-fitting of the 2140 cm^{-1} peak which in time is quickly rectified is a subtle indication as to the decrease in diversity of energy states and thus a transition from a disordered to a more ordered phase which for the remainder of this thesis will be be referred to as a polycrystalline phase. We use the term polycrystalline and not simply crystalline because the Gaussian feature does not completely vanish and is indicative of a remaining degree of disorder [88].

A stronger and more obvious indicator of a transition from disordered to polycrystalline phase is the time evolution of the band area of the 2143 cm^{-1} Lorentzian fitted peak and the 2140 cm^{-1} Gaussian fitted peak (also pictured in figure 42). With time the 2143 cm^{-1} peak increases as the 2140 cm^{-1} peak correspondingly decreases. We fitted the 2140 cm^{-1} band area vs. time curves for all the isothermal experiments using the following exponential decay equation.

$$Area = a \, \exp\left(-k(t - t_o)^n\right) + b \tag{4.1}$$

Where *Area* is the band area, t is the time in seconds, t_o is an experimental offset to account for varying start times for each individual isothermal experiment, k is the decay constant in units $\frac{1}{s^n}$ and the fit parameter of most interest, and a + b is the band area at $t = t_o$. The value of n to which the time parameter is raised is determined from the linearization of the Johnson-Mehl-Avrami-Kolmogorov (JMAK) equation which describes how solids transition from one phase to another under isothermal conditions [93]:

$$Y = 1 - \exp\left(-kt^n\right) \tag{4.2}$$

Where Y is the fraction of ice that has transformed and is referred to as the degree of crystallinity (DOC) and n is the Avrami exponent. For now we assume an n value of 0.8 but in the next section this parameter is explicitly calculated and discussed in further detail. Figure 43 compares

the 8.6 K isothermal exponential decay fitting of the Gaussian 2140 cm^{-1} peak band area vs time with a n value of 1.0 to that of 0.8. One can see from both visual inspection as well as from the residuals (also shown in figure 43) that 0.8 produces a much better fit.

With the decay rate constant k calculated for all isothermal experiments we can then use the Arrhenius equation which describes how reaction rates depend on isothermal temperatures:

$$k = \nu \exp(-\frac{E}{T}) \tag{4.3}$$

where ν is the pre-exponential factor and is in units $\frac{1}{s^{0.8}}$, E is the activation energy of the transformation in units of Kelvin, and T is the isothermal temperature. We write equation [4.3] in linear form by taking the natural log of both sides giving:

$$\ln(k) = -E\frac{1}{T} + \ln(\nu) \tag{4.4}$$

$\ln(k)$ vs. T is plotted, fitted with equation 4.4, and shown in figure 44 giving an activation energy of $E = 222 \pm 17$ K and $\nu = 2$ x 10^9 $\frac{1}{s^{0.8}}$.

4.3.2 Experiments of Kinetics of Carbon Monoxide:Carbon Dioxide 9:1 Mixture

Next we examine the infrared spectral features of 10 ML of CO:CO$_2$ 9:1 mixture deposited on 30 ML of compact ASW at 6K and then heated at 12 K/min to 7.9, 8, 8.1, 8.2, 8.3, 8.4, 8.5, 8.6 K for nine separate isothermal experiments. Figure 45 shows the CO$_2$ ν_3 band at selected times during the 8.6 K isothermal experiment. Also shown is the band area vs time for the entire isotherm for the initial single broad peak at 2344.9 cm^{-1} that is fitted with a Gaussian function and the blue-shifted narrower peak that emerges with time at 2346.7 cm^{-1} that is fitted with a Lorentzian function.

The experimental role that the CO layer plays is a proxy of the CO rich layer in dense ISM clouds (with trace minority species of H, CO, HCO, and CO$_2$ [5]) . As mentioned in the Introduction of this chapter, it is well known that the phase transition of the CO-poor layer, alternatively understood as the water-rich layer, from amorphous to crystalline triggers the diffusion of minority species resulting in segregation and clustering [47]. With this in mind, we attribute the initial Gaussian peak at 2344.9 cm^{-1} to isolated CO$_2$ molecules and the emergence of the Lorentzian peak at 2346.7 cm^{-1} to clusters of CO$_2$ molecules [61]. It is important to note that the CO$_2$ structural change within the CO ice matrix occurs simultaneously with the sharpening and increased intensity of the CO peak at 2140 cm^{-1}. This behavior is explicitly shown and discussed in further detail in the next section in which we explore the slow heat-up of CO-rich ices.

Now we turn our attention to the calculation of n as given by the JMAK equation (eq [4.2]. First we linearize equation[4.2] giving:

$$\ln\left(-\ln\left(1-Y(t)\right)\right) = \ln(k) + n\ln(t) \tag{4.5}$$

Recall Y is the degree of crystallinity (DOC) and is the fraction of the solid that has transformed to a more ordered state. With this principle in mind we define it experimentally as the ratio between the band area underneath the Lorentzian peak at 2346.7 cm^{-1} to the sum of the area under this peak and the Gaussian peak at 2344.9 cm^{-1}. This is plotted in Figure 46. An n value of approximately 0.8 is obtained. It is worth noting that in the conventional theory of crystallization, the n value for a three dimensional solid is usually between 3 and 4. However, in a geometrically confined solid lower values are possible. In fact, crystallization studies of ASW reveal that the Avrami exponent is thickness dependent and decreases from 4 to about 1 when the thickness of ASW decreases from 18 to about 5 ML [94]. Another study found deposition temperature dependence and that the Avrami exponent for 100 nm of ASW decreases from 2.17 to 1.0 when the ice growth temperature drops from 90 K to 14 K [95]. Because the thickness of the CO ices in our experiments 9 ML and 10ML are much smaller and deposited at an even lower temperature 6 K, $n = 0.8$ is reasonable.

With our n value now confirmed and explicitly calculated we can move on to the exponential fitting of the band area vs time using equation [4.1] and following the same analytical treatment from last section we calculate the activation energy of the transformation. Figure 47 shows the fitted exponential decay of the Gaussian peak at 2344.9 cm^{-1} for all isothermal experiments. In Figure 48 $\ln(k)$ vs. T for all isothermal experiments is plotted, fitted with the linearized Arrhenius equation 4.4, and shown in Figure 48, giving an activation energy of $E = 235 \pm 26$ K and $\nu = 8$ x $10^9 \; \frac{1}{s^{0.8}}$.

Taking into account the two measured values of E for the pure CO 2140 cm^{-1} band and the CO:CO$_2$ 9:1 mixture 2345 cm^{-1} band and referring to table 5 in which they are summarized together, we see the activation energy measurements are in agreeance with one another. This is an important conclusion as it is evidence that the presence of CO$_2$ does not alter the activation energy of the transformation, thus justifying the use of CO$_2$ as a probe and showing that the CO ice matrix is not affected by the presence of minority species. Averaging the measured ν values together we obtain 5 X $10^9 \; \frac{1}{s^{0.8}}$. This ν value will be used in the next section for building a predictive model.

4.3.3 Slow Heat-up Experiments

We now turn our attention to experiments in which the temperature of the CO-rich ice was not held constant but slowly heated at a ramp rate of 0.2 K/min. We will be examining these slow heat-up experiments for the CO-ice thicknesses of 2, 5, 7, 9 and 11 ML. The primary motivation for doing so is to investigate how the crystallization temperature depends on the thickness of the pure

CO-rich ice layer. With this accomplished, we will be able to make a predictive model that can be applied to an astrophysical parameter space. Before addressing this, however, we must consider the secondary motivation for the slow heat-up experiments: the confirmation that in the $CO:CO_2$ 9:1 mixtures the structure change for both species occurs simultaneously as was alluded to in the last section. Figure 49 is a two-dimensional density plot that shows the slow heat-up of 10 ML of $CO:CO_2$ 9:1 mixture from 6 K to 13 K at 0.2 K/min and includes both the CO vibrational band at 2143 cm^{-1} and the CO_2 v_3 band at 2345 cm^{-1}. The morphological change occurs between 8 and 9 K and both bands intensify and blue-shift simultaneously at a crystallization temperature of approximately 8.6 K. This results provides us with the impactful conclusion that the structure change of CO facilitates the diffusion of CO_2 molecules within the CO ice matrix.

Moving on to our primary motivation we refer to Figure 50 which is a two-dimensional density plot for the different CO ice thicknesses during the slow heat-up experiments. It is clear that the crystallization temperature increases with reduced thickness. It is likely that this relationship is a consequence of a more confined geometry with increasing thickness. The fact that the crystallization kinetics associated with CO-rich ice reveal themselves in a strong and meaningful manner only at both low temperature and low thickness are contributing factors to the subtlety and elusiveness that makes this particular phenomenon so challenging to study. It is worth noting that the thicknesses studied and presented in Figure 50 are comparable to thicknesses estimated to be in the ISM.

We begin building our predictive model by extracting from Figure 50 the crystallization temperatures and corresponding ice thicknesses, plotting those data points and fitting them with an exponential curve as is shown in Figure 51. This gives the dependence of crystallization temperature on ice thickness and gives the empirical equation:

$$T_{crys} = 16.5 \, \exp(-0.2 \, d) + 6.0 \tag{4.6}$$

We now move away from empiricism for the moment and build a simulation that will give us crystallization temperature as a function of activation energy which in turn when set equal to equation [4.6] will yield an activation energy and ice thickness dependence. The temperature during the slow heat up experiments can be simply related to time by:

$$T(t) = T_o + \beta t \tag{4.7}$$

Where T_o is the initial temperature (6 K) and β is the heating ramp rate (0.2 K/min). Solving equation [4.7] for t gives:

$$t = \frac{T - T_o}{\beta} \tag{4.8}$$

Next, we recall the JMAK equation [4.2] and differentiate it yielding:

$$\frac{dY}{dT} = \frac{dY}{dt}\frac{dt}{dT} = \frac{1}{\beta}\,k\,n\,t^{n-1}\exp\left(-kt^n\right) \tag{4.9}$$

We substitute k and t in equation [4.9] with the Arrhenius equation [4.3] and equation [4.8] respectfully yielding:

$$dY = \frac{1}{\beta}\nu\exp\left(-\frac{E}{T}\right)\,n\,\left(\frac{T-T_o}{\beta}\right)^{n-1}\exp\left[-\nu\exp\left(\frac{E}{T}\right)\left(\frac{T-T_o}{\beta}\right)^{n}\right]dT \tag{4.10}$$

We assume the previously discussed values: $\beta = 0.2$ K/min, $n=0.8$, $\nu=5$ x 10^9 $\frac{1}{s^{0.8}}$. We also assume the fixed E values of 200, 250, 300, 350, 400, 450, 500, 550 K and numerically integrate for each of these E values with respect to temperature between the limits of 6 and 22 K. This produces the degree of crystallinity (DOC) vs. temperature curves shown in Figure 52.

Next, using these simulated curves we define the crystallization temperature (T_{crys}) for each individual curve as the temperature at which the DOC reaches half of its maximum value. We plot the energy value (E) associated with that curve versus T_{crys} and fit it with a linear equation as shown in Figure 53. The line of best fit is given by:

$$T_{crys} = 0.03E + 0.62 \tag{4.11}$$

We set equation [4.11] equal to the empirical equation [4.6] and we obtain the thickness dependence of the activation energy:

$$E(d) = 500\,\exp\left(-0.15d\right) + 126 \tag{4.12}$$

We are now in the exciting position to finish building our predictive model. We will need the JMAK equation [4.2], the Arrhenius equation [4.3], and thickness dependence of the the activation energy [4.12]. We assume in the JMAK equation [4.2] a DOC of $Y = 0.5$ as this is our definition for what constitutes a sufficiently crystallized ice and thus consequentially redefines t in equation 4.2 as the time required for the ice to crystallize (t_{crys}). We also substitute for k in the JMAK equation [4.2] the Arrhenius equation [4.3] (just as we did for the numerical integration of [4.10]) yielding the revised JMAK equation:

$$Y = 0.5 = 1 - \exp\left(-\nu\exp(\frac{E}{T})t_{crys}^n\right) \tag{4.13}$$

We solve equation [4.13] for t$_{crys}$ and substitute for E with equation [4.12] yielding:

$$t_{crys}(d,T) = [\frac{ln(2)}{\nu} \exp(\frac{500\exp(-0.15d) + 126}{T})]^{\frac{1}{n}} \qquad (4.14)$$

Figure 54 shows both the logarithmic three dimensional and two dimensional density plotting of equation [4.14]. We consider parameters of astrophysical relevance that are representative of dense interstellar cloud conditions and plotting a time range of 10^{-10} to 10^{10} years, an ice thickness range of 0 to 10 ML, and the temperature of the ice to be 10 to 15 K. A particularly important distinction is the temporal range as the laboratory time scale over which the temperature is raised and the CO-rich ice crystallizes is simply dwarfed by that of the ISM (hours versus thousands of years) [5].

The best way in which to view the two dimensional plot in Figure 54 and draw meaningful conclusions is to focus our attention on the $10^5 \, t_{crys}$ curve as this is the typical prestellar core lifetime. With this key point of reference it becomes clear that with the exception of the coldest and thinnest CO-rich ice (less than 2 ML and approximately 10 K) the time required for all other crystallization to occur is within the lifetime of the prestellar core. This leads to the larger prediction that according to this model by the time cloud collapse occurs and a protoplanetary system begins to form most of the CO-rich ice in the ISM is in the polycrystalline phase and the diffusion of minority species in the CO-rich ice has been precipitated by this crystallization facilitating COM formation.

4.4 Summary

The structure of CO ice is important for the chemistry on dust grains. However, it has largely been overlooked in previous astronomical/astrochemical studies, including observations, computer modeling, and laboratory simulations. Future endeavors should combine efforts from all of the three aspects. In observations, comparing observed spectra with the laboratory spectra of CO of different morphologies would make it possible to confirm the structure of CO ice on dust grains, as it was done for water ice [96]. In astrochemical models of the interstellar medium, it is crucial to take into account the phase transition of CO ice as a mechanism for solid-state reactions in addition to the conventional mechanism of thermal diffusion. This is especially important for well-shielded clouds where the dust grain temperature is too low for thermal diffusion to be efficient. Computational chemistry would also lend help in systematically studying how the crystallization depends on the substrate material, temperature, thickness, and composition of the ice.

In the laboratory, at least four types of experiments would be highly valuable. Firstly, infrared spectra of CO ice of different morphologies, with and without segregated minority species, need

to be measured. The spectra of the minority species are likely to be affected by the morphology of CO ice and may provide a powerful tool to probe the physical environment of the ice mantle and even provide an insight into the formation mechanism of molecules. Secondly, more experimental studies are needed to further constrain the crystallization kinetics of pure CO ice and CO ice with minority species. Thirdly, experiments in which CO ice with minority species are hydrogenated, nitrogenated, or oxygenated would be advantageous. The in-vacuum helical coaxial resonator presented in chapter two could prove particularly useful in the production of atomic nitrogen. Fedoseev et al. [97] experimentally investigated the formation routes of NH_3 and HNCO through non-energetic surface reactions in interstellar ice analogues at astrophysically relevant temperatures. They co-deposited different ratios of H + N + CO at 13 K monitoring the ice with a RAIRS setup and then performed TPD experiments to monitor via QMS desorption of formed species. They confirmed the formation of NH_3 in H:N:CO upon deposition by measuring the emergence of two signature spectral features. They confirmed the formation of HNCO in by detecting it in the gas phase desorbed during the TPD [97]. In our case, an experiment such as this could be done for CO ice but at temperatures and thicknesses low enough (less than 10 K and less than 10 ML respectively) such that we could observe how the phase transition of CO ice from amorphous to polycrystalline affects molecular formation. This work would allow us to continue to learn about and explore the connection between this transition and molecular formation that is indicative of eventual formation of COMs or COM precursors. Furthermore, infrared spectroscopy, which has been used in this study, should be paired with other techniques such as neutron scattering, X-ray diffraction (such as in the case of Mizuno et al. [88]), and Reflection high-energy electron diffraction (RHEED), which are widely used to characterize the structure of molecular solids. RHEED would be particularly helpful as it has been successfully demonstrated in studies of thin ice films[98]. They would certainly provide further insight into the structure of CO ice and crystallization kinetics[99]. Lastly, laboratory simulations of the chemistry in the ice mantle that take into account the thickness of the CO ice will be fruitful. In the last two decades, numerous laboratory studies of the chemistry in CO-containing ices have probed thermally activated and ionizing irradiation driven reactions [100, 101, 23, 78] without considering the role of the thickness. As is shown in Figure 49, the crystallization of CO ice strongly depends on its thickness. Experiments that utilize a thicker CO ice, as in most existing laboratory studies, likely overestimated the yield of complex organic molecules. Further laboratory studies will help to better constrain the formation of COMs in interstellar clouds.

Findings from this study:

- 9 ML of pure CO ice transforms from amorphous to polycrystalline at isothermal temperatures greater than ~ 7.5 K. The 2143 cm^{-1} Lorentzian spectral peak of pure CO ice sharpens and increases in band area with time while the Gaussian peak at 2140 cm^{-1} correspondingly broadens and decreases in band area.

- The activation energy of the transformation from amorphous to polycrystalline of 9 ML of pure CO ice is measured to be: $E = 222 \pm 17$ K.

- 10 ML of 9:1 CO:CO$_2$ ice transforms from amorphous to polycrystalline at isothermal temperatures approximately greater than ~ 7.5 K. This transformation facilitates the mobilization and clustering of CO$_2$ molecules in the CO ice matrix. There is a sharpening of the 2143 cm^{-1} CO Lorentzian spectral peak and increase in band area with time while the CO Gaussian peak at 2140 cm^{-1} correspondingly broadens and decreases in band area; identical to the first conclusion of this itemized list. Simultaneously, the CO$_2$ Gaussian peak at 2344.9 cm^{-1} decreases in band area as correspondingly a CO$_2$ Lorentzian peak emerges at 2346.7 cm^{-1}.

- 9 ML of pure CO ice and 10 ML of 9:1 CO:CO$_2$ ice transforms from amorphous to crystalline at ~ 8.6 K. This is observed in slow heat up experiments of 9 ML of pure CO and 10 ML of CO:CO$_2$ ice.

- The activation energy of the transformation from amorphous to polycrystalline of 10 ML of 9:1 CO:CO$_2$ ice is measured to be: $E = 222 \pm 17$ K; in agreeance with that of pure CO ice (see Figures 44 and 48 and Table 5).

- CO ices with thicknesses and surface temperatures greater than ~ 2 ML and ~ 10 K respectively require a crystallization time that is within the average prestellar core lifetime of ~ 10 Myrs.

Figure 42: 8.6 K Isothermal experiment for 9 ML of pure CO deposited at 6 K on 30 ML of compact ASW. Top Panel: Fitted IR spectra at selected times. Bottom Panel: The band areas vs time for the entire isothermal experiment.

Table 5: Activation Energy Measurements

Isothermal Experiment	Wave Number	Activation Energy Measurement
Pure CO	$2140 \, cm^{-1}$	222 +/- 17 K
CO:CO2 mixture	$2345 \, cm^{-1}$	235 +/- 26 K
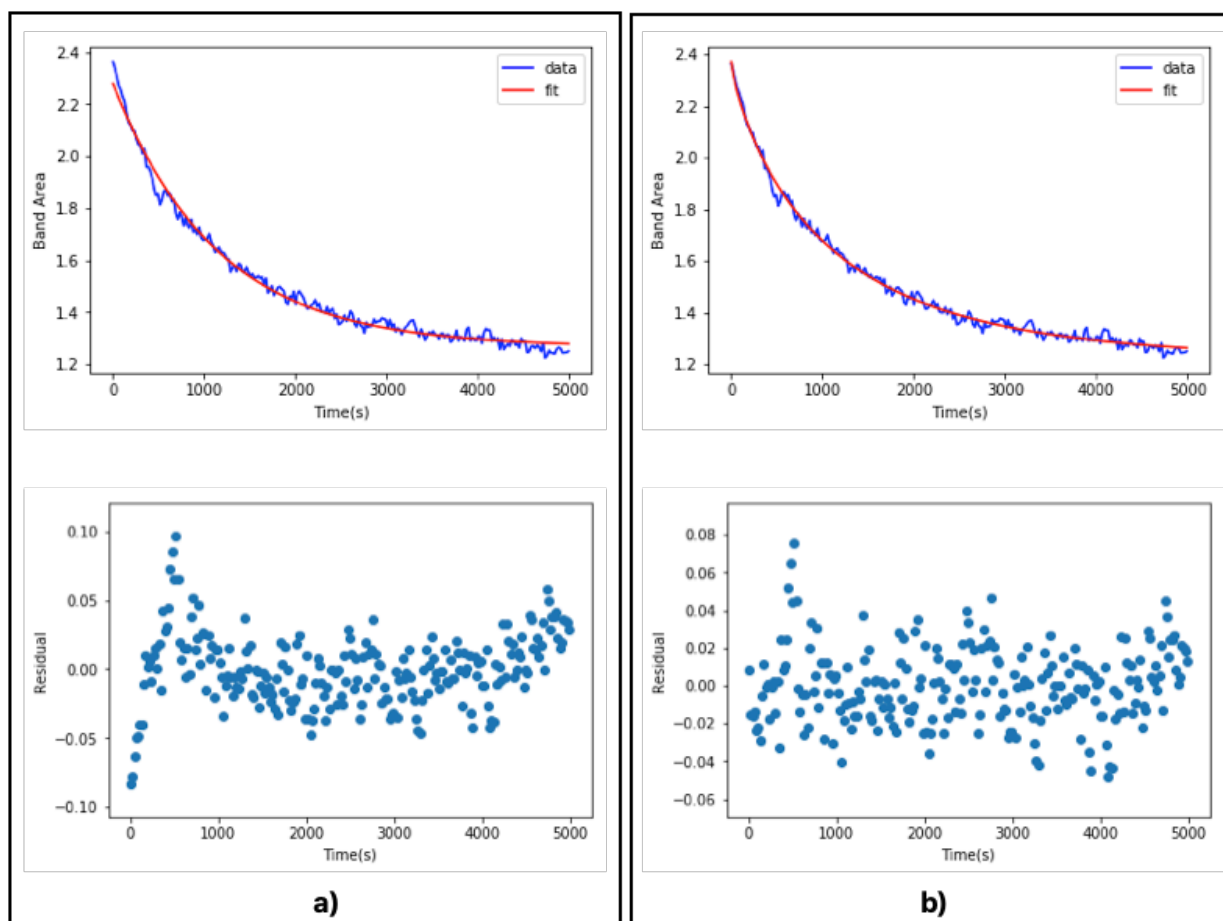
Figure 43: a) Exponential fitting of 2140 cm^{-1} Gaussian component of pure CO during the 8.6 K isotherm using an *n* value of 1.0 b) Exact same as a) but with the exception that an *n* value of 0.8 is used instead.
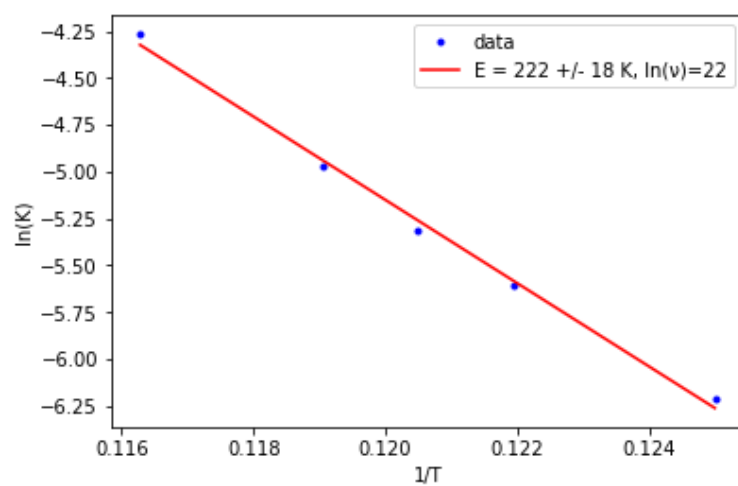
Figure 44: Arrhenius type plot for isothermal experiments of 9 ML of pure CO deposited at 6 K on 30 ML of compact ASW
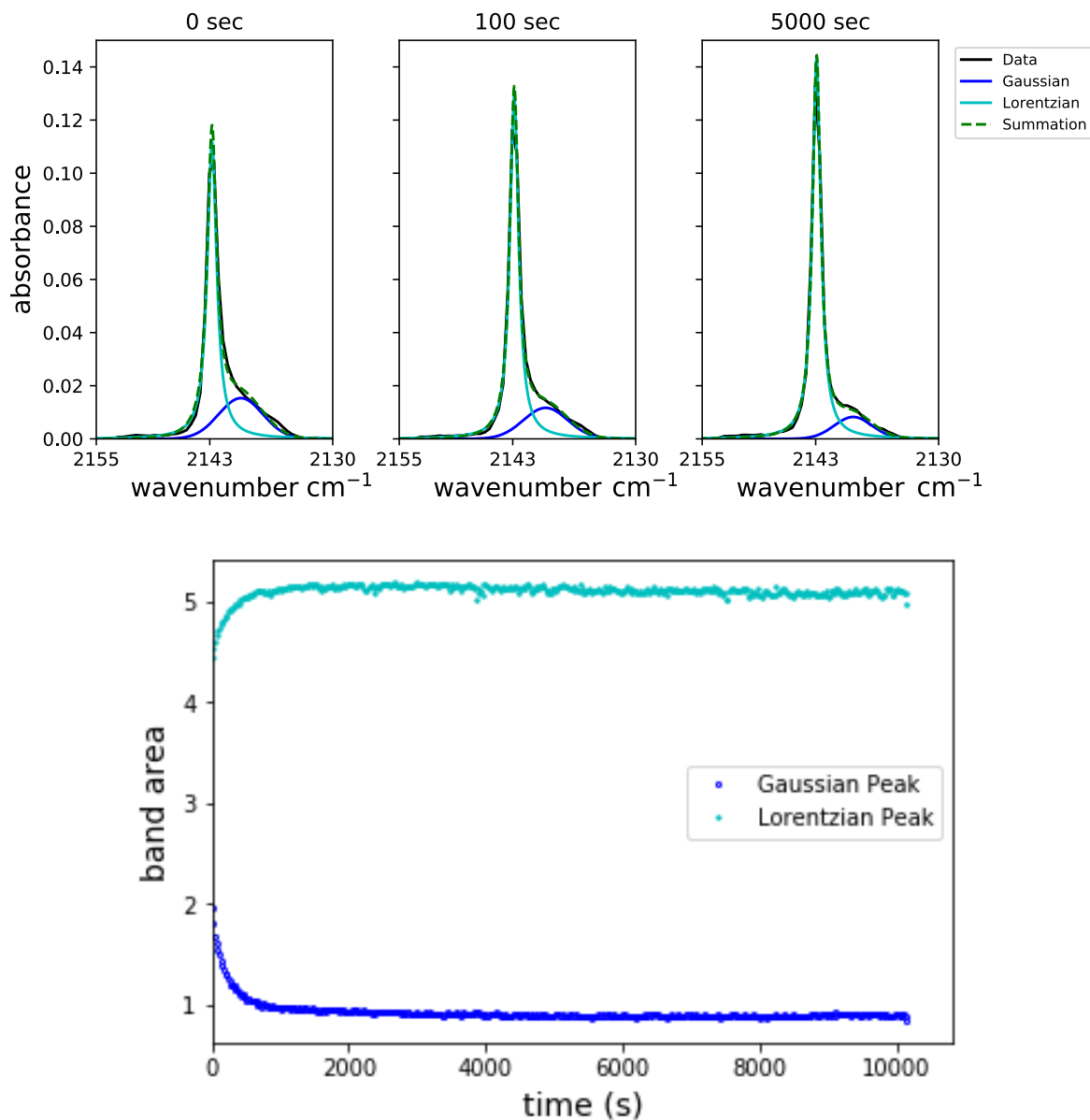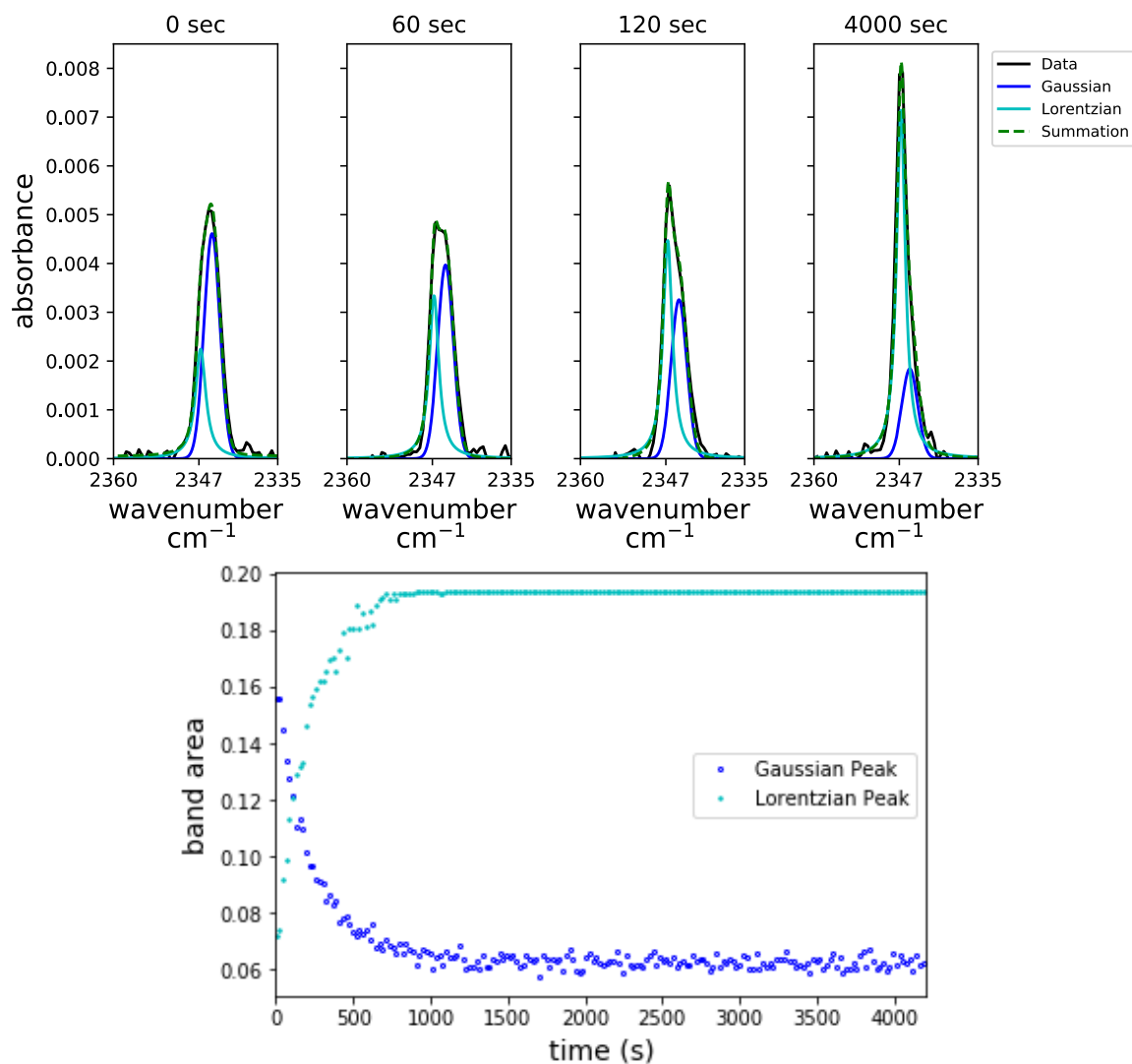
Figure 45: 8.6 K Isothermal experiment for 10 ML of 9:1 CO:CO$_2$ deposited at 6 K on 30 ML of compact ASW. Top Panel: Fitted IR spectra CO$_2$ spectral feature at selected times. Bottom Panel: The band areas vs time for the entire isothermal experiment.
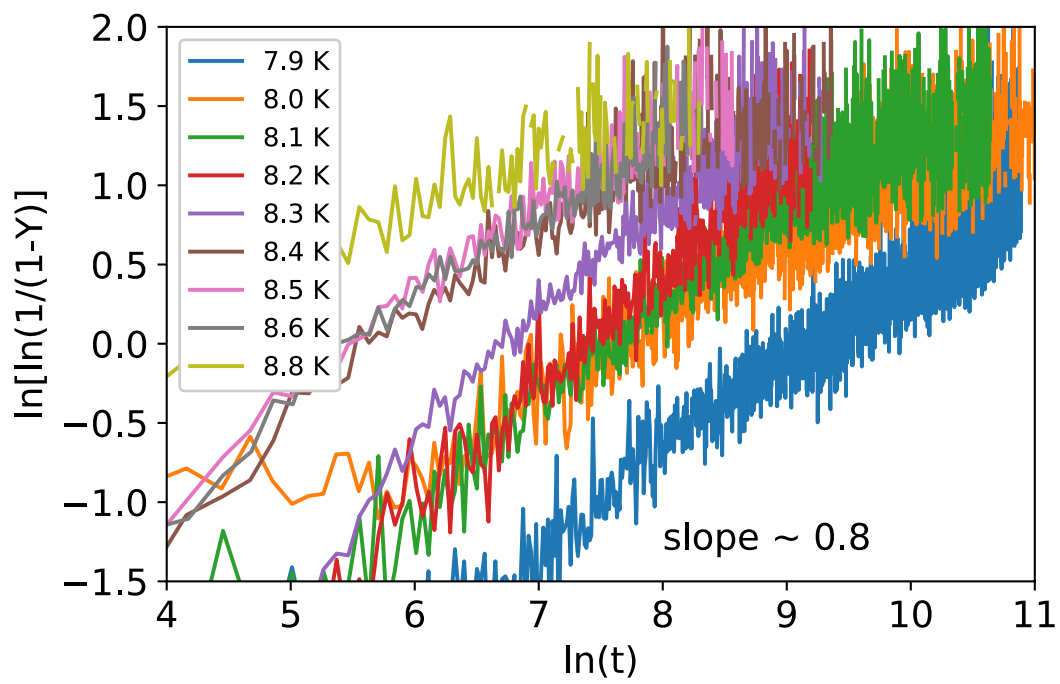
Figure 46: $ln(-ln(1-Y))$ versus $ln(t)$, where Y is the degree of crystallinity.
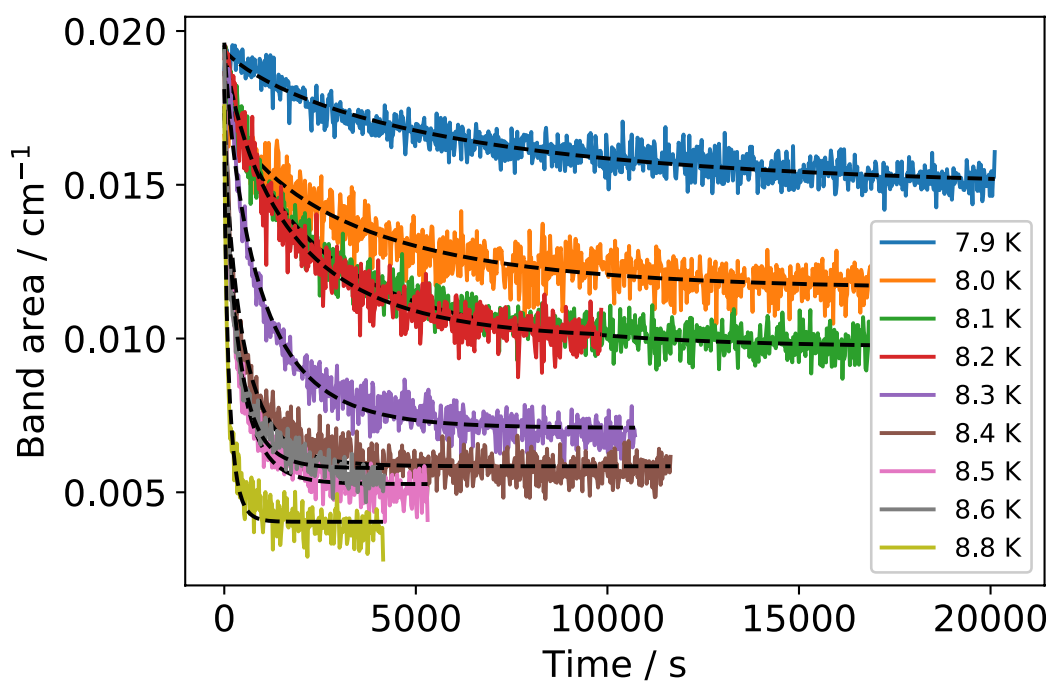
Figure 47: Area the CO_2 2346.7 cm^{-1} band during isotherm experiments at the temperature indicated in the inset. The fitting using $Area = a\exp(-k(t-t_0)^{0.8}) + b$ is shown in black dashed lines.
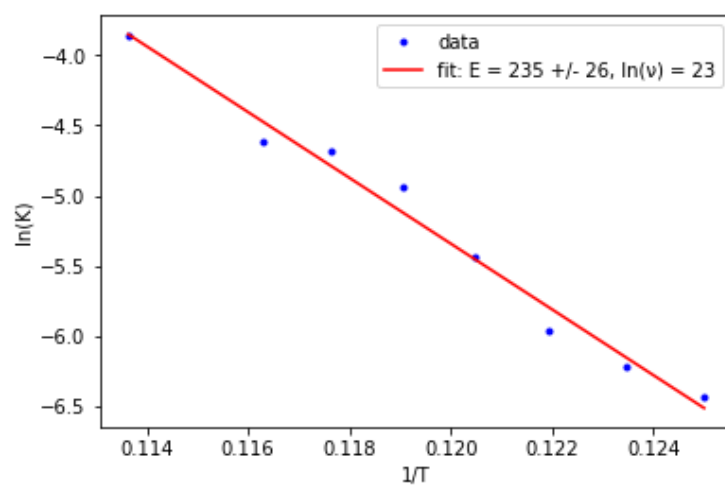
Figure 48: Arrhenius type plot for isothermal experiments of 10 ML of CO:CO$_2$ 9:1 mixture deposited at 6 K on 30 ML of compact ASW
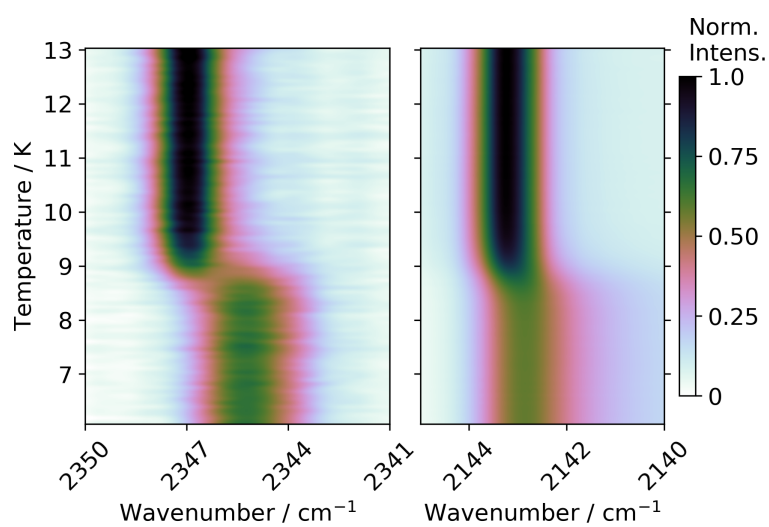
Figure 49: Two dimensional density plot for slow heat up of 10 ML of 9:1 CO:CO_2. On the left is density profile for CO_2 and on the right is the density profile for CO. The ices are deposited on top of np-ASW surface at 6 K and then warmed up at 0.2 K/minute.
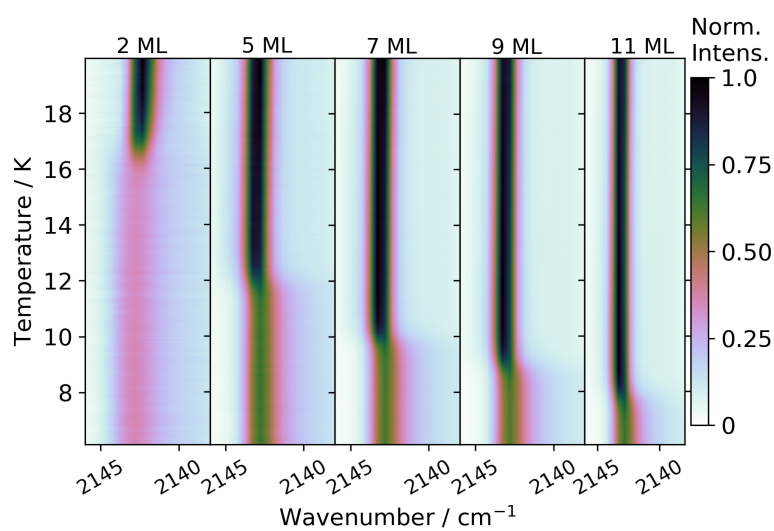
Figure 50: 2D plot of the RAIRS spectra measured during warm-up of CO ice of different thickness. The CO ices are deposited on top of np-ASW surface at 6 K and then warmed up at 0.2 K/minute. The ice thickness is marked on top of each column. The intensity is normalized to the maximum intensity reached in the warm-up.
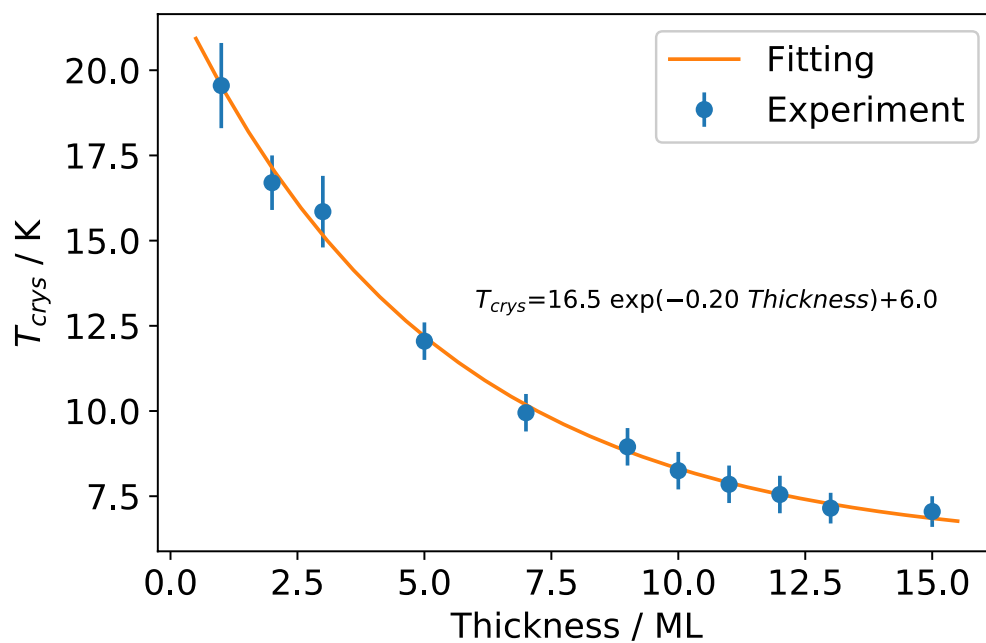
Figure 51: The crystallization temperature of CO ice versus the thickness (blue circles) and the fitting with an empirical function (orange line). The CO ices were grown on np-ASW at 6 K and then warmed up at a ramp rate of 0.2 K/minute.
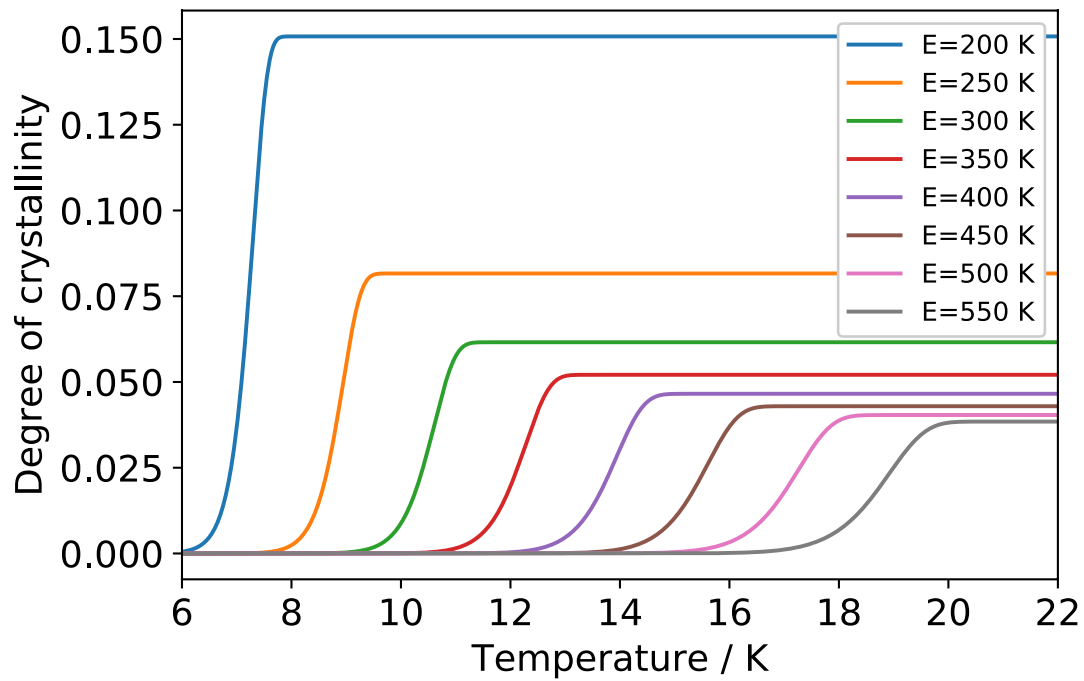
Figure 52: Simulated degree of crystallinity versus temperature using Avrami equation and assuming different activation energies for crystallization. The heating ramp rate is 0.2 K/minute.
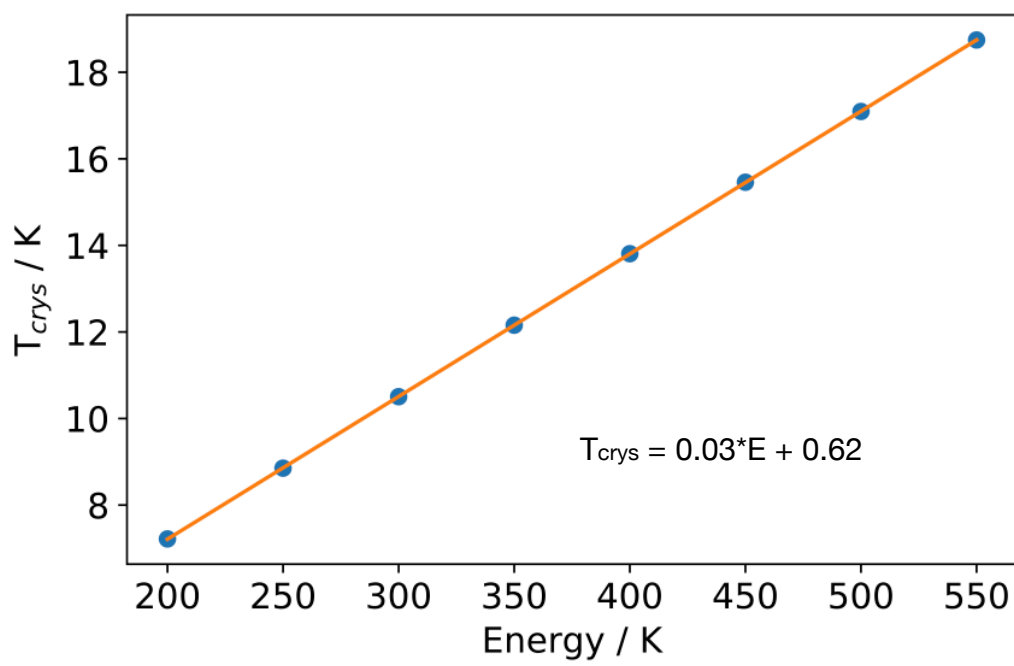
Figure 53: Crystallization temperature versus activation energy extracted from Fig 52. A linear fitting is shown with the orange line.
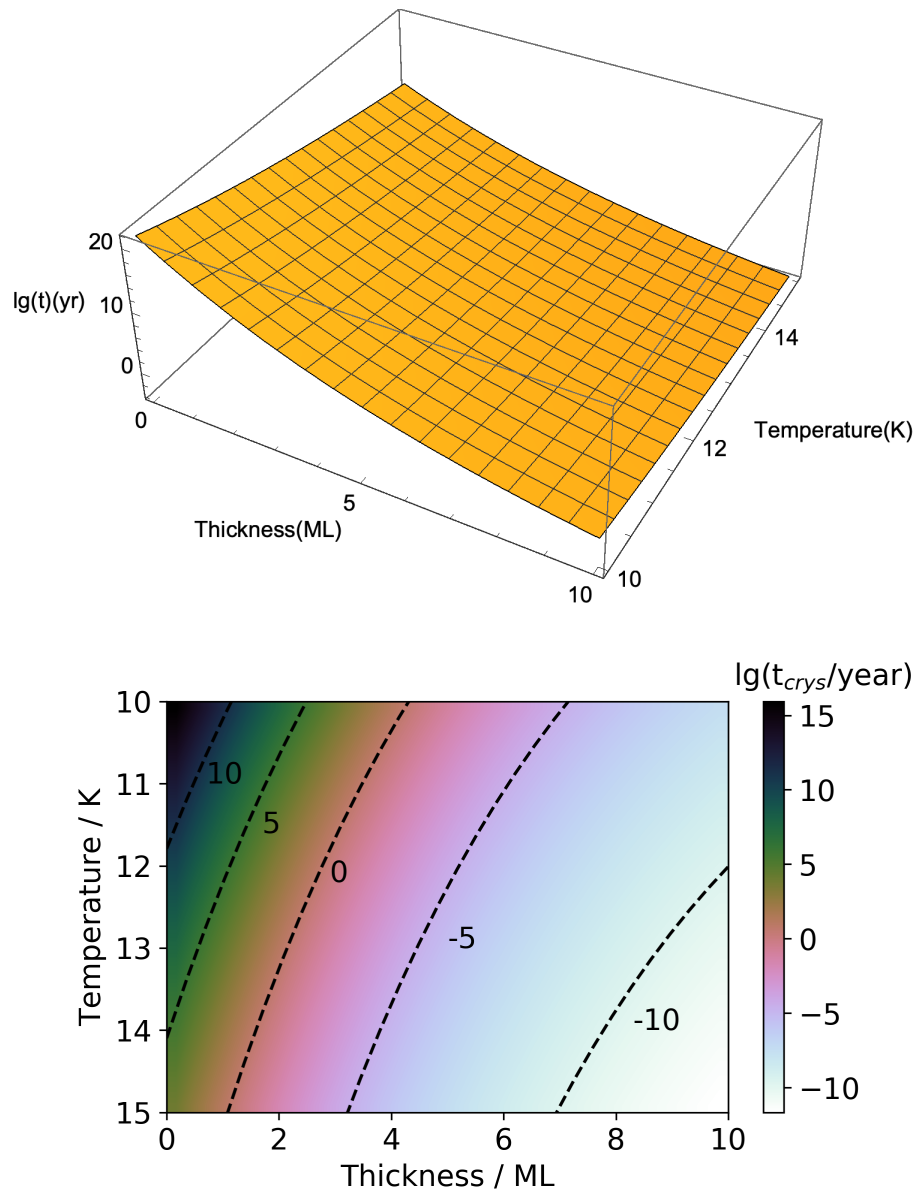
Figure 54: Crystallization time (t_{crys}) as a function of CO ice thickness and temperature. The crystallization time is defined here as the time for the degree of crystallinity to reach half maximum. The time is represented in the logarithmic scale as $lg(t_{crys}/\text{year})$. Top: three dimensional plot Bottom: same as top but plotted two-dimensionally.

Chapter 5

Conclusions

5.1 In-Vacuum Helical Coaxial Resonator (Chapter 2, Section 2.6)

In this section I showed the detailed mathematical modelling, design and implementation of an in-vacuum helical coaxial resonator; built for the dissociation of gaseous molecules and ultimately the production of atomic beams. The primary motivation was to explore the potential that in-vacuum atomic beam sources have with regard to the investigation of COM formation via radical-induced chemistry of interstellar ice analogues. A strong competing motivation was to make a move away from empiricism and develop a more theoretical understanding of the turns ratio parameter and its mathematical relationship to efficient dissociation of gas species; particular interest being taken in the dissociation of N_2 and O_2. Both the plasma impedance and the turns ratio were calculated as a function of electron temperature and electron elastic collisional cross section. We saw that the plasma impedance and required turn ratio in the region of interest for O_2 varied very slightly relative to that of N_2 giving novel theoretical insight in to the challenges associated with the production of atomic nitrogen beams. I was successful in dissociating N_2 but was unable to produce an atomic beam. I was successful in producing an oxygen atomic beam but of relatively low dissociation ($\sim$ 10 %). These shortcomings were useful, however, as they provided a clear understanding of how this important laboratory tool could be improved for future work as was discussed in detail.

5.2 The Effective Surface Area of Amorphous Solid Water Measured by the Infrared Absorption of Carbon Monoxide (Chapter 3)

In this study we sought to characterize the structure of p-ASW with regard to temperature dependence, surface area, the ability to trap molecules, accessibility to adsorption of volatiles from the

vacuum-ice interface, and the presence of minority species. We also sought to visualize p-ASW and its associated phenomena through the use of modeling. The primary motivation for doing so was the exciting promise of efficient catalytic processes that p-ASW may have to offer with regard to the production of COMs in the ISM. In tandem with this was the goal of making a meaningful contribution to the long standing issue of how best to study dOH bonds in order to gain a deeper insights in to the dynamics of p-ASW.

5.3   Phase Transition of Interstellar CO Ice (Chapter 4)

In this study we sought to characterize the morphological transformation of CO-rich ice from amorphous to polycrystalline. It is worth noting that this transformation has never been reported or studied before and constitutes a discovery. We performed isothermal experiments for 9 ML of pure CO and 10 ML of a 9:1 $CO:CO_2$ mixture. The latter was done so as to investigate the effect had on astrophysically relevant CO ice minority species; a potential mechanism of zeroth generation COM formation [5]. To confirm the independence of the CO ice morphological transition from the presence of CO_2 in the ice matrix we performed slow heat up experiments of pure CO and a 9:1 $CO:CO_2$ mixture. We also performed slow heat up experiments of various thicknesses of pure CO ice so as to discern an ice thickness dependence on the temperature at which this transition occurs. This dependence allowed us to build an astrophysically relevant predictive model for the duration of time required for this transition to occur for ices of different thicknesses and temperatures in dense molecular clouds in the ISM.

Bibliography

[1] Tetsuya Hama and Naoki Watanabe. Surface Processes on Interstellar Amorphous Solid Water: Adsorption, Diffusion, Tunneling Reactions, and Nuclear-Spin Conversion. *Chemical Reviews*, 113(12):8783–8839, 2013.

[2] C. F. McKee and J. P. Ostriker. A theory of the interstellar medium: three components regulated by supernova explosions in an inhomogeneous substrate. *The Astrophysical Journal*, 218:148–169, November 1977.

[3] Hincelin, U., Wakelam, V., Hersant, F., Guilloteau, S., Loison, J. C., Honvault, P., and Troe, J. Oxygen depletion in dense molecular clouds: a clue to a low o2 abundance? *Astronomy and Astrophysics*, 530:A61, 2011.

[4] W. W. Macalpine and R. O. Schildknecht. Coaxial Resonators with Helical Inner Conductor. *Proceedings of the IRE*, 47(12):2099–2105, 1959.

[5] Ewine F. van Dishoeck. Astrochemistry of dust, ice and gas: introduction and overview. *Faraday Discuss.*, 168:9–47, 2014.

[6] Jiao He. *Laboratory Studies of Gas-Grain Processes on Cosmic Dust Analogues* . PhD thesis, Syracuse U.

[7] Pascal Chabert and Nicholas Braithwaite. *Physics of Radio Frequency Plasma*. Cambridge University Press, New York, NY, 2011.

[8] Steven J. Sibener, Richard J. Buss, Cheuk Yiu Ng, and Yuan T. Lee. Development of a supersonic O(3PJ), O(1D2) atomic oxygen nozzle beam source. *Review of Scientific Instruments*, 51(2):167–182, 1980.

[9] Jiao He, Aspen R. Clements, SM Emtiaz, Francis Toriello, Robin T. Garrod, and Gianfranco Vidali. The Effective Surface Area of Amorphous Solid Water Measured by the Infrared Absorption of Carbon Monoxide. *The Astrophysical Journal*, 878(2):94, jun 2019.

[10] Alexander Dalgarno. A Serendipitous Journey. *Annual Review of Astronomy and Astro-physics*, 46(1):1–20, 2008.

[11] A. C. A. Boogert, P. A. Gerakines, and D. C. B. Whittet. Observations of the icy universe. *Annual Review of Astronomy and Astrophysics*, 53:541–581, August 2015.

[12] C.W. Allen. *Astrophysical Quantities*. Athlone Press, 1973.

[13] Sarah M R Jeffreson and J M Diederik Kruijssen. A general theory for the lifetimes of giant molecular clouds under the influence of galactic dynamics. *Monthly Notices of the Royal Astronomical Society*, 476(3):3688–3715, 03 2018.

[14] Kobayashi K. *Complex Organic Molecules*. Springer, Berlin, Heidelberg, September 2011.

[15] Eric Herbst and Ewine F. van Dishoeck. Complex Organic Interstellar Molecules. *Annual Review of Astronomy and Astrophysics*, 47:427–480, September 2009.

[16] Eric Herbst and Ewine F. van Dishoeck. Complex organic interstellar molecules. *Annu. Rev. Astron. Astrophys.*, 47(1):427–480, September 2009.

[17] Arnaud Belloche, Robin T. Garrod, Holger S. P. Müller, and Karl M. Menten. Detection of a branched alkyl molecule in the interstellar medium: iso-propyl cyanide. *Science*, 345(6204):1584–1587, 2014.

[18] B. A. McGuire, P. B. Carroll, R. A. Loomis, I. A. Finneran, P. R. Jewell, A. J. Remijan, and G. A. Blake. Discovery of the interstellar chiral molecule propylene oxide (CH3CHCH2O). *Science*, 352(6292):1449–1452, June 2016.

[19] E. Casuso and J. E. Beckman. EXPLAINING THE GALACTIC INTERSTELLAR DUST GRAIN SIZE DISTRIBUTION FUNCTION. *The Astronomical Journal*, 139(4):1406–1412, mar 2010.

[20] J. S. Mathis, W. Rumpl, and K. H. Nordsieck. The size distribution of interstellar grains. *The Astrophysical Journal*, 217:425–433, October 1977.

[21] Klaus M. Pontoppidan, A. C. A. Boogert, Helen J. Fraser, Ewine F. van Dishoeck, Geoffrey A. Blake, Fred Lahuis, Karin I. Öberg, Neal J. Evans II, and Colette Salyk. The c2d sSpitzer spectroscopic survey of ices around low-mass young stellar objects. II. CO2. *Astrophys. J.*, 678(2):1005–1031, May 2008.

[22] D. M. Hudgins, S. A. Sandford, L. J. Allamandola, and A. G. G. M. Tielens. Mid- and Far-Infrared Spectroscopy of Ices: Optical Constants and Integrated Absorbances. *The Astrophysical Journal Supplement Series*, 86:713, June 1993.

[23] H. Linnartz, S. Ioppolo, and G. Fedoseev. Atom addition reactions in interstellar ice analogues. *Int. Rev. Phys. Chem.*, 34(2):205–237, April 2015.

[24] K. M. Pontoppidan, H. J. Fraser, E. Dartois, W.-F. Thi, E. F. van Dishoeck, A. C. A. Boogert, L. D'Hendecourt, A. G. G. M. Tielens, and S. E. Bisschop. A 3-5um VLT spectroscopic survey of embedded young low mass stars I. *Astron. Astrophys.*, 408(3):981–1007, September 2003.

[25] V. Ásgeirsson, H. Jónsson, and K. T. Wikfeldt. Long-Time Scale Simulations of Tunneling-Assisted Diffusion of Hydrogen on Ice Surfaces at Low Temperature. *The Journal of Physical Chemistry C*, 121(3):1648–1657, 2017.

[26] Gianfranco Vidali. Cosmic Low Temperature Physics: Making Molecules on Stardust. *Journal of Low Temperature Physics*, 170(1-2):1–30, January 2013.

[27] Campargue. *Atomic and Molecular Beams, The State of the Art 2000*. Springer, New York, NY, 2001.

[28] J. Valleau and J. Deckers. SUPERSONIC MOLECULAR BEAMS: II. THEORY OF THE FORMATION OF SUPERSONIC MOLECULAR BEAMS. *Canadian Journal of Chemistry*, 43:6–17, 02 2011.

[29] Schnepal Fadini. *Vibrational Spectroscopy*. Ellis Horwood Limited, Market Cross House, Cooper Street, Chichester, West Sussex, PO191EB, England, 1989.

[30] Dawson. *Quadrupole Mass Spectrometry and its application*. Elsevier Scientific Publishing Company, New York, NY, 1976.

[31] McPherson DW, Rahman K, Martinez I, and Shevlin PB. The formation of amino acid precursors in the reaction of atomic carbon with water and ammonia at 77 k. *Orig Life Evol Biosph*, 17, 1987.

[32] K. Hiraoka, A. Yamashita, Y. Yachi, K. Aruga, T. Sato, and H. Muto. Ammonia Formation from the Reactions of H Atoms with N Atoms Trapped in a Solid N 2 Matrix at 10–30 K. *The Astrophysical Journal*, 443:363, April 1995.

[33] Michele Alagia, Vincenzo Aquilanti, Daniela Ascenzi, Nadia Balucani, David Cappelletti, Laura Cartechini, Piergiorgio Casavecchia, Fernando Pirani, Giampaolo Sanchini, and Gian G. Volpi. Magnetic Analysis of Supersonic Beams of Atomic Oxygen, Nitrogen, and Chlorine Generated from a Radio-Frequency Discharge. *Israel Journal of Chemistry*, 37(4):329–342, 1997.

[34] R B Piejak, V A Godyak, and B M Alexandrovich. A simple analysis of an inductive RF discharge. *Plasma Sources Science and Technology*, 1(3):179–186, aug 1992.

[35] Livesey. *Foundations of Vacuum Science and Technology*. Wiley, New York, NY, 1998.

[36] Yukikazu Itikawa. Cross Sections for Electron Collisions with Nitrogen Molecules. *Journal of Physical and Chemical Reference Data - J PHYS CHEM REF DATA*, 35, 03 2006.

[37] Yukikazu Itikawa. Cross sections for electron collisions with oxygen molecules. *Journal of Physical and Chemical Reference Data - J PHYS CHEM REF DATA*, 38:1–20, 03 2009.

[38] Abdullah Eroglu. *RF Circuit Design Techniques for MF-UHF Applications*. CRC Press, Boca Raton, FL, 2013.

[39] Vasco Guerra, Paulo A Sá, and Jorge Loureiro. Nitrogen pink afterglow: the mystery continues. *Journal of Physics: Conference Series*, 63:012007, apr 2007.

[40] K. Isokoski, J. B. Bossa, T. Triemstra, and H. Linnartz. Porosity and thermal collapse measurements of H2O, CH3OH, CO2, and H2O:CO2 ices. *Physical Chemistry Chemical Physics (Incorporating Faraday Transactions)*, 16:3456, January 2014.

[41] Sing Gregg. *Adsorption, Surface Area, and Porosity*. Academic Press Inc, New York, NY, 1982.

[42] Chaplin, Martin. Hydrogen Bonding in Water. http://www1.lsbu.ac.uk/water/water_hydrogen_bonding.html, May 2020.

[43] V. Buch and J. P. Devlin. Spectra of dangling OH bonds in amorphous ice: Assignment to 2- and 3-coordinated surface molecules. *J. Phys. Chem*, 94:4091–4092, March 1991.

[44] Karolina Marga-Riitta Guss. *Physics and Chemistry of Interstellar ice* . PhD thesis, Leiden U.

[45] Karin I. Öberg, Viviana V. Guzmán, Kenji Furuya, Chunhua Qi, Yuri Aikawa, Sean M. Andrews, Ryan Loomis, and David J. Wilner. The comet-like composition of a protoplanetary disk as revealed by complex cyanides. *Nature*, 520:198–201, April 2015.

[46] A. Bieler, K. Altwegg, H. Balsiger, A. Bar-Nun, J. J. Berthelier, P. Bochsler, C. Briois, U. Calmonte, M. Combi, J. de Keyser, E. F. van Dishoeck, B. Fiethe, S. A. Fuselier, S. Gasc, T. I. Gombosi, K. C. Hansen, M. Hässig, A. Jäckel, E. Kopp, A. Korth, L. Le Roy, U. Mall, R. Maggiolo, B. Marty, O. Mousis, T. Owen, H. Rème, M. Rubin, T. Sémon, C. Y. Tzou, J. H. Waite, C. Walsh, and P. Wurz. Abundant molecular oxygen in the coma of comet 67P/Churyumov-Gerasimenko. *Nature*, 526:678–681, October 2015.

[47] R. Scott Smith, C. Huang, E. K. L. Wong, and Bruce D. Kay. The molecular volcano: Abrupt ccl$_4$ desorption driven by the crystallization of amorphous solid water. *Phys. Rev. Lett.*, 79:909–912, Aug 1997.

[48] R. Alan May, R. Scott Smith, and Bruce D. Kay. The release of trapped gases from amorphous solid water films. II. "Bottom-up" induced desorption pathways. *J. Phys. Chem.*, 138:104502–104502, March 2013.

[49] Agúndez, Marcelino, Cernicharo, José, and Guélin, Michel. Discovery of interstellar ketenyl (HCCO), a surprisingly abundant radical. *Astronomy and Astrophysics*, 577:L5, 2015.

[50] M. E. Palumbo. Formation of compact solid water after ion irradiation at 15 K. *Astronomy and Astrophysics*, 453:903–909, July 2006.

[51] U. Raut, B. D. Teolis, M. J. Loeffler, R. A. Vidal, M. Famá, and R. A. Baragiola. Compaction of microporous amorphous solid water by ion irradiation. *J. Phys. Chem*, 126:244511–244511, June 2007.

[52] Christian Mitterdorfer, Marion Bauer, Tristan G. A. Youngs, Daniel T. Bowron, Catherine R. Hill, Helen J. Fraser, John L. Finney, and Thomas Loerting. Small-angle neutron scattering study of micropore collapse in amorphous solid water. *Physical Chemistry Chemical Physics (Incorporating Faraday Transactions)*, 16:16013, July 2014.

[53] J. V. Keane, A. G. G. M. Tielens, A. C. A. Boogert, W. A. Schutte, and D. C. B. Whittet. Ice absorption features in the 5-8 μm region toward embedded protostars. *Astronomy and Astrophysics*, 376:254–270, September 2001.

[54] Jiao He, SM Emtiaz, and Gianfranco Vidali. Measurements of Diffusion of Volatiles in Amorphous Solid Water: Application to Interstellar Medium Environments. *The Astrophysical Journal*, 863:156, August 2018.

[55] K. P. Stevenson, Greg A. Kimmel, Z. Dohnalek, R. Scott Smith, and Bruce D. Kay. Controlling the Morphology of Amorphous Solid Water. *Science*, 283:1505, March 1999.

[56] Greg A. Kimmel, K. P. Stevenson, Z. Dohnálek, R. Scott Smith, and Bruce D. Kay. Control of amorphous solid water morphology using molecular beams. I. Experimental results. *J. Phys. Chem*, 114:5284–5294, March 2001.

[57] Z. Dohnálek, Greg A. Kimmel, Patrick Ayotte, R. Scott Smith, and Bruce D. Kay. The deposition angle-dependent density of amorphous solid water films. *J. Phys. Chem.*, 118:364–372, January 2003.

[58] U. Raut, M. Famá, B. D. Teolis, and R. A. Baragiola. Characterization of porosity in vapor-deposited amorphous solid water from methane adsorption. *J. Phys. Chem*, 127:204713–204713, November 2007.

[59] J. B. Bossa, K. Isokoski, D. M. Paardekooper, M. Bonnin, E. P. van der Linden, T. Triemstra, S. Cazaux, A. G. G. M. Tielens, and H. Linnartz. Porosity measurements of interstellar ice mixtures using optical laser interference and extended effective medium approximations. *Astronomy and Astrophysics*, 561:A136, January 2014.

[60] S. Cazaux, J. B. Bossa, H. Linnartz, and A. G. G. M. Tielens. Pore evolution in interstellar ice analogues. Simulating the effects of temperature increase. *Astronomy and Astrophysics*, 573:A16, January 2015.

[61] Jiao He and Gianfranco Vidali. Characterization of thin film CO_2 ice through the infrared $\nu_1 + \nu_3$ combination mode. *Monthly Notices of the Royal Astronomical Society*, 473:860–866, January 2018.

[62] Robin T. Garrod. Three-dimensional, off-lattice monte carlo kinetics simulations of interstellar grain chemistry and ice structure. *The Atrophysical Journal*, 778(158):14, December 2013.

[63] Aspen R. Clements, Brandon Berk, Ilsa R. Cooke, and Robin T. Garrod. Kinetic monte carlo simulations of water ice porosity: extrapolations of deposition parameters from the laboratory to interstellar space. *Physical Chemistry Chemical Physics*, 20:5553–5568, 2018.

[64] D E Brown, S M George, C Huang, E K L Wong, K B Rider, R S Smith, and B D Kay. H2O condensation coefficient and refractive index for vapor-deposited ice from molecular beam and optical interference measurements. *Journal of Physical Chemistry*, 100:4988–4995, 1996.

[65] Bradley, Michael. Curve Fitting in Raman and IR Spectroscopy. https://assets.thermofisher.com/TFS-Assets/CAD/Application-Notes/AN50733_E.pdf, May 2020.

[66] R. Scott Smith, Tykhon Zubkov, Zdenek Dohnálek, and Bruce D. Kay. The Effect of the Incident Collision Energy on the Porosity of Vapor-Deposited Amorphous Solid Water Films. *J. Phys. Chem*, September 2009.

[67] Caixia Bu, Jianming Shi, Ujjwal Raut, Emily H. Mitchell, and Raúl A. Baragiola. Effect of microstructure on spontaneous polarization in amorphous solid water films. *J. Phys. Chem*, 142:134702, April 2015.

[68] Helen J. Fraser, Mark P. Collings, John W. Dever, and Martin R. S. McCoustra. Using laboratory studies of CO-H_2O ices to understand the non- detection of a 2152cm^{-1} (4.647μm) band in the spectra of interstellar ices. *Monthly Notices of the Royal Astronomical Society*, 353:59–68, September 2004.

[69] Mark P. Collings, John W. Dever, and Martin R. S. McCoustra. Sub-monolayer coverages of CO on water ice. *Chemical Physics Letters*, 415:40–45, October 2005.

[70] Tykhon Zubkov, R. Scott Smith, Todd R. Engstrom, and Bruce D. Kay. Adsorption, desorption, and diffusion of nitrogen in a model nanoporous material. II. Diffusion limited kinetics in amorphous solid water. *J. Chem. Phys.*, 127(18):184708, November 2007.

[71] Noriko Horimoto, Hiroyuki S. Kato, and Maki Kawai. Stepwise morphological change of porous amorphous ice films observed through adsorption of methane. *J. Phys. Chem*, 116:4375–4378, March 2002.

[72] B. Schmitt, J. Mayo Greenberg, and R. J. A. Grim. The Temperature Dependence of the CO Infrared Band Strength in CO: H 2O Ices. *The Astrophysical Journal*, 340:L33, May 1989.

[73] Jiao He, SM Emtiaz, Adwin Boogert, and Gianfranco Vidali. The $^{12}CO_2$ and $^{13}CO_2$ Absorption Bands as Tracers of the Thermal History of Interstellar Icy Grain Mantles. *The Astrophysical Journal*, 869:41, December 2018.

[74] Greg A. Kimmel, Z. Dohnálek, K. P. Stevenson, R. Scott Smith, and Bruce D. Kay. Control of amorphous solid water morphology using molecular beams. II. Ballistic deposition simulations. *The Journal of Chemical Physics*, 114(12):5295–5303, March 2001.

[75] M. Eldrup, A. Vehanen, Peter J. Schultz, and K. G. Lynn. Positronium formation and diffusion in crystalline and amorphous ice using a variable-energy positron beam. *Physical Review B*, 32:7048–7064, December 1985.

[76] Weijun Zheng, David Jewitt, and Ralf I. Kaiser. Electron irradiation of crystalline and amorphous D $_2$O ice. *Chemical Physics Letters*, 435:289–294, February 2007.

[77] A. I. Vasyunin and Eric Herbst.

[78] K.-J. Chuang, G. Fedoseev, D. Qasim, S. Ioppolo, E. F. van Dishoeck, and H. Linnartz. Production of complex organic molecules: H-atom addition versus UV irradiation. *Mon. Not. R. Astron. Soc.*, 467(3):2552–2565, June 2017.

[79] M. a. J. Simons, T. Lamberts, and H. M. Cuppen. Formation of COMs through CO hydrogenation on interstellar grains. *Astron. Astrophys.*, 634:A52, February 2020.

[80] K.-J. Chuang, G. Fedoseev, S. Ioppolo, E. F. van Dishoeck, and H. Linnartz. H-atom addition and abstraction reactions in mixed CO, H2CO and CH3OH ices – an extended view on complex organic molecule formation. *Mon. Not. R. Astron. Soc.*, 455(2):1702–1712, January 2016.

[81] R. T. Garrod and E. Herbst. Formation of methyl formate and other organic species in the warm-up phase of hot molecular cores. *Astron. Astrophys.*, 457(3):927–936, October 2006.

[82] P. D. Brown, S. B. Charnley, and T. J. Millar. A model of the chemistry in hot molecular cores. *Monthly Notices of the Royal Astronomical Society*, 231(2):409–417, 03 1988.

[83] Anne Horn, Harald Mollendal, Osamu Sekiguchi, Einar Uggerud, Helen Roberts, Eric Herbst, A. A. Viggiano, and Travis D. Fridgen. The gas-phase formation of methyl formate in hot molecular cores. *The Astrophysical Journal*, 611(1):605–614, aug 2004.

[84] Ulrich Essmann and Alfons Geiger. Molecular dynamics simulation of vapor deposited amorphous ice. *J. Chem. Phys.*, 103(11):4678–4692, September 1995.

[85] P. Jenniskens and D. F. Blake. Crystallization of amorphous water ice in the solar system. *Astrophys. J.*, 473(2):1104–1113, December 1996.

[86] R. Alan May, R. Scott Smith, and Bruce D. Kay. The molecular volcano revisited: determination of crack propagation and distribution during the crystallization of nanoscale amorphous solid water films. *J. Phys. Chem. Lett.*, 3(3):327–331, February 2012.

[87] Pierre Ghesquiere, A. Ivlev, Jennifer Noble, and P. Theulé. Reactivity in interstellar ice analogs: Role of the structural evolution. *Astronomy Astrophysics*, 614, 03 2018.

[88] Yuki Mizuno, Maiko Kofu, and Osamu Yamamuro. X-ray diffraction study on simple molecular glasses created by low-temperature vapor deposition. *J. Phys. Soc. Jpn.*, 85(12):124602, November 2016.

[89] Hani Kang, Josée Maurais, Youngwook Park, Patrick Ayotte, and Heon Kang. Electric Field Effect on Condensed-Phase Molecular Systems. VIII. Vibrational Stark Effect and Dipolar Inversion in a Carbon Monoxide Crystal. *The Journal of Physical Chemistry C*, 123(51):31262–31271, 2019.

[90] Alexia Simon, Karin I. Öberg, Mahesh Rajappan, and Pavlo Maksiutenko. Entrapment of CO in CO2 Ice. *The Astrophysical Journal*, 883(1):21, Sep 2019.

[91] Jiao He, SM Emtiaz, and Gianfranco Vidali. Measurements of diffusion of volatiles in amorphous solid water: application to interstellar medium environments. *Astrophys. J.*, 863(2):156, August 2018.

[92] Jiao He and Gianfranco Vidali. Characterization of thin film co_2 ice through the infrared ν_1 + ν_3 combination mode. *Mon. Not. R. Astron. Soc.*, 473(1):860–866, January 2018.

[93] Melvin Avrami. Granulation, phase change, and microstructure kinetics of phase change. III. *J. Chem. Phys.*, 9(2):177–184, February 1941.

[94] Kuniaki Harada, Toshiki Sugimoto, Fumiaki Kato, Kazuya Watanabe, and Yoshiyasu Matsumoto. Thickness dependent homogeneous crystallization of ultrathin amorphous solid water films. *Phys. Chem. Chem. Phys.*, 22(4):1963–1973, 2020.

[95] Belén Maté, Yamilet Rodríguez-Lazcano, and Victor J. Herrero. Morphology and crystallization kinetics of compact (HGW) and porous (ASW) amorphous water ice. *Phys. Chem. Chem. Phys.*, 14(30):10595–10602, July 2012.

[96] Robert G. Smith, K. Sellgren, and Alan T. Tokunaga. Absorption features in the 3 micron spectra of protostars. *Astrophys. J.*, 344:413–426, September 1989.

[97] Gleb Fedoseev, Sergio Ioppolo, Dongfeng Zhao, Thanja Lamberts, and H. Linnartz. Low Temperature Surface Formation of NH_3 and HNCO: hydrogenation of nitrogen atoms in CO-rich interstellar ice analogues. *Monthly Notices of the Royal Astronomical Society*, 446, 12 2014.

[98] Ding-Shyue Yang and Ahmed H. Zewail. Ordered water structure at hydrophobic graphite interfaces observed by 4D, ultrafast electron crystallography. *Proc. Natl. Acad. Sci.*, 106(11):4122–4126, March 2009.

[99] Ryutaro Souda and Takashi Aizawa. Crystallization kinetics of thin water films on Pt(111): effects of oxygen and carbon-monoxide adspecies. *Phys. Chem. Chem. Phys.*, 21(3):1123–1130, 2019.

[100] Chris J Bennett, Corey S Jamieson, and Ralf I Kaiser. Mechanistical studies on the formation and destruction of carbon monoxide (CO), carbon dioxide (CO2), and carbon trioxide (CO3) in interstellar ice analog samples. *Phys. Chem. Chem. Phys.*, 12(16):4032–50, May 2010.

[101] Y S Kim, F Zhang, and R I Kaiser. Laboratory simulation of Kuiper belt object volatile ices under ionizing radiation: CO-N2 ices as a case study. *Phys. Chem. Chem. Phys.*, 13(35):15766–73, September 2011.

Curriculum Vitae

Francis Toriello

Personal details

Citizenship	United States of America
Birth	June 20, 1983
Phone	(609) 432-6726
Mail	FToriello@PearlCohen.com

Education

Syracuse University   **2014-Present**

Doctor of Philosophy in Physics

   Advisor: Dr. Gianfranco Vidali.

   Expected Graduation date: 2020

Columbia University   **2011-2014**

Bachelor of Arts in Physics with Astrophysics specialization

Employment

Patent Agent   **2020-Present**

Pearl Cohen Zedek Latzer Baratz

Graduate Student Research Assistant   **2016-2020**

Syracuse University, Advisor: Dr. Gianfranco Vidali

Teacher's Assistant **2014-2016**

Syracuse University

Professional Physics and Math Tutor **2014**

Ocean County College

Undergraduate Research Assistant **2012-2013**

Columbia University, Advisor: Dr. Brian Humensky

Publications

S. Emtiaz, F. Toriello, J. He, G. Vidali "Infrared Spectroscopic Study of Solid methane: nuclear Spin Conversion of Stable and Metastable Phases". In: *J. Phys. Chem* 124.3 (2019), p. 552. DOI: 10.1021/acs.jpca.9b10643.

J. He, A. Clements, S. Emtiaz, F. Toriello , R.T. Garrod, G. Vidali "The Effective Surface Area of Amorphous Solid Water Measured by the Infrared Absorption of Carbon Monoxide". In: *Astrophys J.* 124.3 (2019), p. 94. DOI: 10.3847/1538-4357/ab1f6a.

M. Eadan, F. Toriello "Autonomous Cavity Resonator and Heat Map". In: *Patent Application* 15/785,956 (2019), US 2019/0116634 A1.

F. Toriello "Cherenkov Telescope Mirror Alignment Report". In: *Columbia Undergraduate Science Journal* 8 (2014)